



# CHALMERS

---



## Gravitational instability of nearby galaxies: dwarfs vs. spirals

*Master of science thesis*

Saladin Grebović

Supervisor: Alessandro Romeo

---

Department of Earth and Space Sciences  
Chalmers University of Technology  
Gothenburg, Sweden  
June 2014



MASTER'S THESIS

# Gravitational instability of nearby galaxies: dwarfs vs. spirals

Saladin Grebović  
Supervisor: Alessandro Romeo

Department of Earth and Space Sciences  
Chalmers University of Technology  
Gothenburg, Sweden

June 2014

Gravitational instability of nearby galaxies: dwarfs vs. spirals  
Saladin Grebović, [saladin.grebovic@comhem.se](mailto:saladin.grebovic@comhem.se)

© Saladin Grebović 2014

Department of Earth and Space Sciences  
Chalmers University of Technology  
SE-412 96 Gothenburg, Sweden  
+46 31-772 1000

Onsala Space Observatory  
SE-439 92 Onsala, Sweden  
+46 31-772 5500

The composite image on the title page shows the spiral galaxy NGC 628 (the large image) and the dwarf irregular galaxy Holmberg I (the small image). The galaxies are shown approximately in scale. Note the difference in size and morphology between them. Sources: [http://apod.nasa.gov/apod/image/0305/m74\\_gemini\\_big.jpg](http://apod.nasa.gov/apod/image/0305/m74_gemini_big.jpg) for NGC 628 and Ott et al. (2001) for Holmberg I.

## Abstract

Star formation is one of the most important subjects in all of astrophysics. Previous analyses have shown that there is a link between star formation and gravitational instabilities in galactic discs. In this thesis we investigate the gravitational instability of 9 dwarf and 12 spiral galaxies from The H I Nearby Galaxy Survey (THINGS), previously analyzed by Leroy et al. (2008), using the Romeo-Falstad (2013)  $Q$  stability parameter for multicomponent and realistically thick galactic discs. Our analysis allows us: (1) to quantify how the stability properties of the dwarfs differ from those of the spirals, (2) to determine how the disc stability properties vary with galactocentric distance, and (3) to establish which component dominates the gravitational instability of the disc. We find that the dominant component differs significantly between the two subsamples in a statistical sense. Even so, the median value of the  $Q$  stability parameter is nearly independent of galactocentric distance with a value of order unity for both the dwarfs and the spirals, suggesting that galactic discs may be controlled by self-regulation processes. Two important quantities that enter our stability analysis are the stellar and gaseous velocity dispersions, which we find to have a strong impact on disc instability. In all current stability analyses such quantities are estimated through simple models (e.g. Leroy et al. 2008) since they are difficult to measure. However, our analysis illustrates that using observed stellar and gaseous velocity dispersions would be very useful for understanding the complex link between star formation and gravitational instabilities in disc galaxies.



# Acknowledgments

I would first of all like to extend my gratitude to my supervisor Alessandro Romeo for his time, effort and many good advice. I would also like to thank the professors and PhD students at Onsala Space Observatory for their hospitality and interesting seminars, presentations and discussions, and also for letting me turn their library into my private office. Moreover, I would like to thank my opponent Carl Toft for his interesting questions and for opposing my thesis on the morning of the same day as his own examination.

Last but not least, I would like to express my deepest gratitude for all the love and support which my dad, my sister and her family have given me. I could not have done this without their help!

Saladin Grebović  
Gothenburg, Sweden  
June 2014



# Contents

<b>1</b>	<b>Introduction</b>	<b>1</b>
<b>2</b>	<b>Overview of THINGS galaxies and stability parameters</b>	<b>5</b>
2.1	THINGS galaxies . . . . .	5
2.2	Stability parameters . . . . .	8
<b>3</b>	<b>Stability analysis: dwarfs vs. spirals</b>	<b>11</b>
3.1	Computing the Romeo-Falstad $Q_N$ stability parameter . . . . .	11
3.1.1	Basic quantities . . . . .	11
3.1.2	Observational data . . . . .	14
3.2	Scatter plots of $Q_N$ vs. galactocentric distance . . . . .	15
3.3	Stability properties as functions of galactocentric distance . . . . .	19
<b>4</b>	<b>Searching for physical correlations</b>	<b>23</b>
<b>5</b>	<b>How reliable is our stability analysis?</b>	<b>31</b>
5.1	The short-wavelength approximation . . . . .	31
5.2	Velocity dispersions . . . . .	33
<b>6</b>	<b>Conclusions</b>	<b>41</b>
<b>A</b>	<b>Radial profiles of individual galaxies</b>	<b>43</b>
<b>B</b>	<b>Error analysis</b>	<b>57</b>



# Chapter 1

## Introduction

Star formation is one of the most important subjects in all of astrophysics. Without stars there would be no planets, no starlight, no elements heavier than lithium and no life. Despite its enormous significance and after several decades of intense research there are still many questions left to be answered regarding the star formation process. The perhaps two most important ones are: where are stars formed and at what rate? A hint to the answers lies in the Kennicutt-Schmidt (1998, 1959) law  $\Sigma_{\text{SFR}} \propto \Sigma_{\text{g}}^n$ , where  $\Sigma_{\text{SFR}}$  is the star formation rate surface density and  $\Sigma_{\text{g}}$  is the surface density of gas in a galactic disc and  $n \approx 1.4$  according to Kennicutt (1998). This empirical formula relates small-scale star formation to the large-scale distribution of gas in disc galaxies. Its existence implies that the rate at which stars are formed is strongly influenced by some phenomenon with a very long range, and gravity is an excellent candidate.

Soon after Toomre (1964) had developed a very idealized local stability criterion Spitzer (1968) and Quirk (1972) suggested that gravitational instability might set a lower limit to the gas surface density necessary for stars to form in a galactic disc. Martin & Kennicutt (2001) investigated the gravitational instability of 32 nearby spiral galaxies using the Toomre (1964) criterion and they found indications of a gas surface density threshold in these galaxies (see figure 1.1). Unfortunately, they could not use the simple Toomre (1964) stability parameter to account for the vivid star formation in the inner discs of low-mass galaxies. They also found that the ratio between the observed critical gas surface density and the theoretical critical density predicted by the Toomre (1964) criterion varied between the galaxies in their sample.

Martin & Kennicutt (2001) speculated that these variations may be due to differences in the relative contributions of stars to the gravitational instability of the gas. Although their paper arose a great deal of interest in gravitational instability it also illustrated the necessity of using more sophisticated stability parameters which at least consider the influence of stars. Leroy et al. (2008) used such a parameter calculated by Rafikov (2001) to explore the gravitational instability of 12 spiral and 9 dwarf galaxies from The HI Nearby Galaxy Survey (THINGS). The same spiral galaxies were also analyzed by Romeo & Wiegert (2011) and Romeo & Falstad (2013) using more advanced stability parameters than that of Rafikov (2001). However, neither of the latter studies investigated the gravitational instability of the 9 dwarf galaxies.

Large galaxies are believed to have formed through clustering of smaller objects such

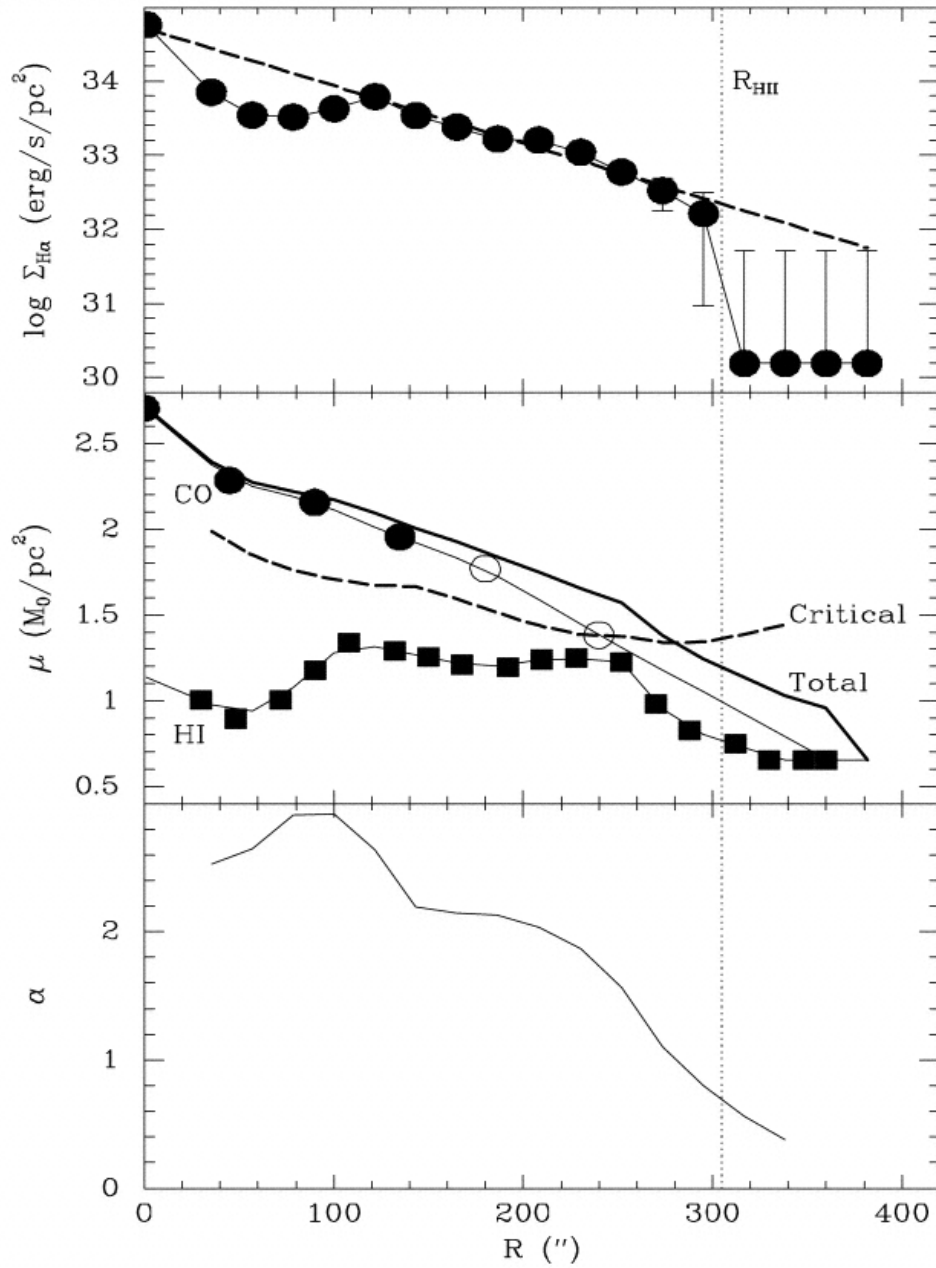


Figure 1.1: *From Martin & Kennicutt (2001)*. The top plot shows the H $\alpha$  surface brightness radial profile for the galaxy NGC 5236 (the dashed line is a fitted exponential function). Since H $\alpha$ -emission is a tracer of star formation we can see in this plot that the star formation rate surface density falls drastically beyond the threshold radius  $R_{\text{HII}}$ . The middle plot shows the radial profiles of gas (H I + H $_2$ ), H $_2$  (as traced by CO-emission) and H I. These surface densities have been multiplied by 1.4 to account for helium. The dashed curve shows the critical surface density given by the Toomre (1964) criterion and we see that the gas surface density falls below the critical density close to  $R_{\text{HII}}$ . The bottom plot shows the ratio  $\alpha$  between the total gas surface density and the critical density.

as dwarf galaxies. Studying the star formation process in the latter type of galaxies is therefore of vital importance for our understanding of the evolution of galaxies such as the one we live in. In this thesis we use the most advanced stability parameter available, namely that of Romeo & Falstad (2013), to analyze the 9 dwarf galaxies mentioned above and to compare their stability properties to those of the 12 spiral galaxies.

The rest of the thesis is organized as follows. In chapter 2 we present the galaxies in our study as well as the survey from which they were selected by Leroy et al. (2008), and we also briefly describe the stability parameters of greatest interest to us. Our stability analysis is performed in chapter 3 and in chapter 4 we search for physical correlations involving  $\Sigma_{\text{SFR}}$ . We investigate how reliable our stability analysis is in chapter 5 before we give our conclusions in chapter 6. In appendix A we provide radial profiles of important parameters for the individual galaxies in our study and in appendix B we briefly describe our error analysis.



# Chapter 2

## Overview of THINGS galaxies and stability parameters

### 2.1 THINGS galaxies

The H I Nearby Galaxy Survey (THINGS) is a very ambitious survey of the 21 cm line emission from neutral atomic hydrogen (H I) in 34 nearby galaxies. It is based on observations made at the Very Large Array of the National Radio Astronomy Observatory during the period 1989–2005. Most of the galaxies in THINGS were selected from the sample of the *Spitzer* Infrared Nearby Galaxies Survey (SINGS) in order to enable multiwavelength analyses of these objects. The THINGS galaxies were also chosen to represent a wide range of star formation rates, total H I masses, absolute luminosities and metallicities (i.e. total mass fractions of elements heavier than helium). They are at distances of about 2–15 Mpc from us ( $1 \text{ pc} \approx 3.26 \text{ light years}$ ). (Walter et al. 2008)

The first THINGS paper (Walter et al.) was published in 2008, and since then many others have followed. The one of greatest interest to us is the paper by Leroy et al. (2008), which includes a gravitational stability analysis of THINGS galaxies. The parameters and radial profiles necessary to repeat their analysis have been placed in the VizieR database<sup>1</sup> (<http://vizier.u-strasbg.fr/>), from where they are accessible to anyone. It was this data which enabled the analysis in this thesis!

For their analysis Leroy et al. (2008) depend on an overlap between data from THINGS, SINGS, the *Galaxy Evolution Explorer* (GALEX) Nearby Galaxies Survey (NGS) and (for the large spiral galaxies) either the Berkeley-Illinois-Maryland Association (BIMA) Survey of Nearby Galaxies (SONG) or the HERA CO-Line Extragalactic Survey (HERACLES). They can therefore only analyze 23 of the 34 THINGS galaxies. (Leroy et al. 2008)

They arrange their sample of 23 nearby star-forming galaxies by their total stellar masses  $M_*$  in an increasing order, and they classify the first 11 galaxies as ‘dwarf galaxies’ (or simply ‘dwarfs’). The remaining 12 galaxies are large spiral galaxies (or ‘spirals’) (see table 2.1). For reasons which will be explained in section 3.1.1, Leroy et al. (2008) had to exclude two of the dwarfs from their stability analysis. This means that the total number

---

<sup>1</sup>This research has made use of the VizieR catalogue access tool, CDS, Strasbourg, France.

Table 2.1: The sample of Leroy et al. (2008), which was also analyzed in this thesis (see table 2 and 4 in Leroy et al. 2008). The galaxies have been arranged by their total stellar masses  $M_*$  in an increasing order and the table shows their basic morphologies according to Leroy et al. (2008). The two galaxies within parentheses were excluded from both the gravitational stability analysis of Leroy et al. (2008) as well as the analysis in this thesis.

	Dwarfs	Morphology		Spirals	Morphology
1	DDO 154	Irregular	12	NGC 628	Spiral
2	Ho I	Irregular	13	NGC 3198	Spiral
3	Ho II	Irregular	14	NGC 3184	Spiral
4	IC 2574	Irregular	15	NGC 4736	Spiral
5	NGC 4214	Irregular	16	NGC 3351	Spiral
6	NGC 2976	Spiral	17	NGC 6946	Spiral
7	(NGC 4449)	Irregular	18	NGC 3627	Spiral
8	(NGC 3077)	Spiral	19	NGC 5194	Spiral
9	NGC 7793	Spiral	20	NGC 3521	Spiral
10	NGC 2403	Spiral	21	NGC 2841	Spiral
11	NGC 925	Spiral	22	NGC 5055	Spiral
			23	NGC 7331	Spiral

of dwarfs and spirals in both theirs as well as our analysis is 9 and 12, respectively.

The dwarfs have rotation velocities  $v_{\text{rot}} \lesssim 125$  km/s, total stellar masses  $M_* \lesssim 10^{10} M_{\odot}$ <sup>2</sup> and absolute magnitudes in the blue band  $M_B \gtrsim -20$ , while the spirals have  $v_{\text{rot}} \gtrsim 125$  km/s,  $M_* \gtrsim 10^{10} M_{\odot}$  and  $M_B \lesssim -20$ . (Leroy et al. 2008).  $M_B$  is a measure of the intrinsic brightness of an object in a narrow band centered at 4400 Å. The lower the value of  $M_B$  the brighter the object is in this band. Relative to the spirals, the dwarfs also tend to have low metallicities, intense radiation fields, low galactic shear, weak or absent spiral structures (Leroy et al. 2008), smaller optical radii and lower star formation rates (see table 4 in Leroy et al. 2008). The optical radius of a galaxy is defined as the radial distance from the optical center of the galaxy where the surface brightness in the blue band has, on an average, decreased to 25 magnitudes per square arcsecond.

Moreover, the dwarfs are H I-rich while the spirals are H<sub>2</sub>-dominated. (Leroy et al. 2008). We also see in table 2.1 that the majority of the dwarfs, unlike the spirals, have irregular morphologies. Galaxies are morphologically classified by the way they appear when viewed through an optical telescope. Galaxies which have clear spiral structures or structureless elliptical shapes are called spiral and elliptical galaxies, respectively. Many galaxies cannot be classified as either spiral or elliptical galaxies, and these galaxies are called irregular galaxies. Some irregular galaxies have weak spiral or elliptical features, while others have no apparent structure of any kind. Also, irregular galaxies may or may not be disc-shaped.

Spiral and elliptical galaxies are further divided into sub-categories according to their ellipticities and how closely wound their spiral arms are, respectively. Spiral galaxies are

<sup>2</sup> $M_{\odot}$  is the mass of the Sun. In general, the symbol  $\odot$  represents the Sun.

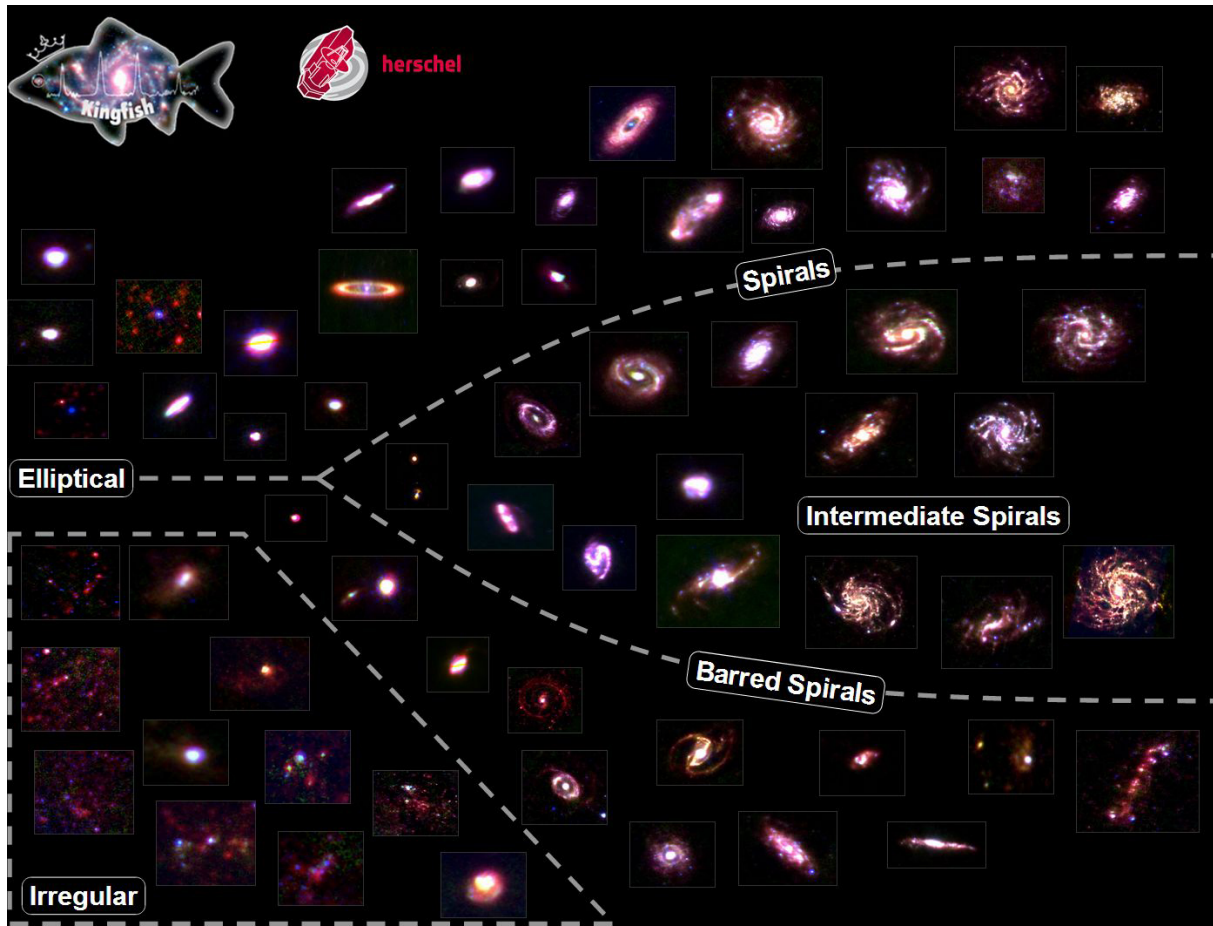


Figure 2.1: The 61 KINGFISH galaxies arranged into the Hubble sequence, which is also known as the ‘Hubble tuning-fork’ due to its appearance. KINGFISH is a survey of nearby galaxies in the far infrared part of the spectrum which uses data from the Herschel space telescope. (Source: [http://www.esa.int/spaceinimages/Images/2013/02/Interactive\\_Hubble\\_Tuning\\_Fork](http://www.esa.int/spaceinimages/Images/2013/02/Interactive_Hubble_Tuning_Fork))

also separated into those with or without bars/bulges at the center. In some classification schemes, such as the de Vaucouleurs system, one also considers whether or not galaxies have ring-like structures. The reader should be alerted to the fact that there exists neither a universally accepted system of galaxy morphology classification nor an unambiguous method of determining which category within a given system a galaxy belongs to. We have therefore omitted detailed morphological information in table 2.1.

However, to illustrate the basic differences in appearance between spiral, elliptical and irregular galaxies we have included figure 2.1, which shows an attempt to organize the 61 galaxies in the Key Insights on Nearby Galaxies (KINGFISH) survey into the Hubble sequence. The latter is a famous morphological classification scheme which was invented by Hubble in 1936.

## 2.2 Stability parameters

Let us first have a look at the (Safronov-) Toomre (1964) stability parameter  $Q$ . Suppose that we have an infinitesimally thin single-component disc which rotates differentially, i.e. the angular velocity is a function of the radius  $R$ . Next, suppose that we perturb the disc with *small* axisymmetric, or tightly wound, waves. One can then show that the disc is gravitationally stable at  $R$  against waves with *short*, but otherwise arbitrary, radial wavelengths if the Toomre (1964) stability criterion is satisfied:

$$Q > 1, \quad Q = \frac{\kappa\sigma}{\pi G\Sigma}, \quad (2.1)$$

where  $\kappa(R)$  is the epicyclic angular frequency,  $\sigma$  is the radial velocity dispersion,  $G$  is the gravitational constant and  $\Sigma(R)$  is the surface density.

The reason for why the waves have to be small is that the Toomre (1964) stability criterion is derived using linear perturbation theory, and the reason for why the radial wavelength has to be small has to do with the fact that “gravity is a long-range force, so perturbations in all parts of the system are coupled”, as Binney & Tremain (2008) put it. However, if the radial wavelength is much smaller than the radius then the long-range coupling may be neglected and the response of the system to the perturbations is determined by local conditions. This simplifies the analysis considerably, as does the assumption of axisymmetry. The assumption of a short radial wavelength is in this context usually referred to as the ‘short-wavelength approximation’, and it may be written as  $|kR| \gg 1$ , where  $k$  is the radial wavenumber. (Binney & Tremain 2008, pp. 485, 486)

Unfortunately, the Toomre (1964) criterion (2.1) is ill-suited as a diagnostic for gravitational instability of galactic discs, since such discs are multi-component systems with non-zero thicknesses. However, it is possible to derive Toomre-like stability criteria, i.e. on the form  $Q > 1$ , which allow for several components if one replaces the Toomre (1964) parameter with an appropriately defined *effective* stability parameter  $Q$ .

In their analysis of the gravitational stability of THINGS galaxies Leroy et al. (2008) use an effective stability parameter calculated by Rafikov (2001), which treats both the stars and the gas as fluids (see equation 15 and 16 in Leroy et al. 2008). This parameter allows for a single gaseous and an arbitrary number of stellar components, but Leroy et al. (2008) treat all the stars in a galaxy as a single component. To treat stars of different types as different components would have given more accurate results, but there is not enough observational data to perform such an analysis.

However, one can treat H I and H<sub>2</sub> as separate components, but this is not possible with the Rafikov (2001) stability parameter. This parameter also neglects the thickness of the disc and it is difficult to compute since doing so requires the maximization of a so-called stability curve.

Romeo & Wiegert (2011) showed that for a two-component system of stars and gas it is possible to define an approximation  $Q_{\text{WR}}$  of the effective stability parameter which is accurate, simple and fast to compute, takes into account the thickness of the disc and makes it easy to see which component dominates  $Q$ . We will see in the next chapter that the latter information is very important in stability analyses.

Romeo & Falstad (2013) generalized  $Q_{\text{WR}}$  into an accurate approximation of the effective stability parameter for a system with an arbitrary number of stellar and gaseous

components. For an  $N$ -component system their stability parameter  $Q_N$  is given by (see equation 16, 18 and 19 in Romeo & Falstad 2013)

$$\frac{1}{Q_N} = \sum_{i=1}^N \frac{W_i}{T_i Q_i} \quad (2.2)$$

$$Q_i = \frac{\kappa \sigma_i}{\pi G \Sigma_i} \quad (2.3)$$

$$W_i = \frac{2\sigma_m \sigma_i}{\sigma_m^2 + \sigma_i^2} \quad (2.4)$$

$$T \approx \begin{cases} 1 + 0.6 \left( \frac{\sigma_z}{\sigma_R} \right)^2 & \text{for } 0 \lesssim \sigma_z / \sigma_R \lesssim 0.5 \\ 0.8 + 0.7 \left( \frac{\sigma_z}{\sigma_R} \right) & \text{for } 0.5 \lesssim \sigma_z / \sigma_R \lesssim 1 \end{cases} \quad (2.5)$$

where  $\sigma_i$  and  $\Sigma_i$  are the radial velocity dispersion and surface density of the  $i$ :th component,  $\sigma_z$  and  $\sigma_R$  are the vertical and radial velocity dispersions, and  $m$  denotes the component with smallest  $TQ$ :  $T_m Q_m = \min\{T_i Q_i\}$ .

It is easy to show that  $W_i \leq 1$  and that  $W_i = 1$  precisely when  $i = m$ . We therefore see in (2.2) that the component with smallest  $TQ$  is also the component which dominates  $Q_N$ .

Romeo & Falstad (2013) used their stability parameter to perform a three-component analysis of the gravitational stability properties of the spirals in table 2.1, in which stars, H<sub>1</sub> and H<sub>2</sub> were treated as distinct components.



# Chapter 3

## Stability analysis: dwarfs vs. spirals

### 3.1 Computing the Romeo-Falstad $Q_N$ stability parameter

The value of  $Q_N$  at different radii was computed for the 9 dwarfs and the 12 spirals for a disc consisting of: (1) stars and H I, (2) stars and gas, where the gas in turn consists of H I and H<sub>2</sub>, and (3) stars, H I and H<sub>2</sub>. We will refer to case 1 as ‘ $Q_2$  without H<sub>2</sub>’, case 2 as ‘ $Q_2$  with H<sub>2</sub>’, and case 3 as simply  $Q_3$ . For reasons which will be explained in a moment, there is no observational data on the surface density of H<sub>2</sub> for the dwarfs. This means that for the dwarfs  $Q_2$  without H<sub>2</sub> is the most reliable stability parameter in the sense that it is the only one computed solely from observational data without additional approximations, besides from those used in all three cases. However,  $Q_2$  without H<sub>2</sub> is also *less* reliable than the other two stability parameters in the sense that it completely ignores the molecular gas in the disc. From this perspective  $Q_2$  with H<sub>2</sub> is better than  $Q_2$  without H<sub>2</sub>, but the former parameter has the weakness that it treats H I and H<sub>2</sub> as a single component.  $Q_3$  is therefore the best stability parameter for the spirals and, to the extent that we can trust the estimated values of  $\Sigma_{\text{H}_2}$  for the dwarf galaxies, it is also the best for the dwarfs.

Since the main purpose of this thesis is to compare the gravitational stability properties of the dwarfs with those of the spirals described in Romeo & Falstad (2013), we used *precisely* the same observational database, assumptions and approximations as they did to compute  $Q_N$ . This way we can be sure that any difference between the stability properties of the two subsamples is due solely to the physical dissimilarities between dwarfs and spirals. Moreover, since Romeo & Falstad (2013) used the data and methods of Leroy et al. (2008), our results are also directly comparable to those of Leroy et al. (2008).

#### 3.1.1 Basic quantities

Let us now show how to compute  $Q_N$ . We see in equation (2.2)–(2.5) that we need to know the values of the parameters listed below, where the index notation should be

self-explanatory.

$$Q_2 \text{ without H}_2 : \sigma_*, \sigma_{\text{HI}}, (\sigma_z/\sigma_R)_*, (\sigma_z/\sigma_R)_{\text{HI}}, \Sigma_*, \Sigma_{\text{HI}}, G, \kappa \quad (3.1)$$

$$Q_2 \text{ with H}_2 : \sigma_*, \sigma_g, (\sigma_z/\sigma_R)_*, (\sigma_z/\sigma_R)_g, \Sigma_*, \Sigma_g, G, \kappa \quad (3.2)$$

$$Q_3 : \sigma_*, \sigma_{\text{HI}}, \sigma_{\text{H}_2}, (\sigma_z/\sigma_R)_*, (\sigma_z/\sigma_R)_{\text{HI}}, (\sigma_z/\sigma_R)_{\text{H}_2}, \Sigma_*, \Sigma_{\text{HI}}, \Sigma_{\text{H}_2}, G, \kappa \quad (3.3)$$

In summary, we need to know the values of:

$$\begin{aligned} &\sigma_*, \sigma_g, \sigma_{\text{HI}}, \sigma_{\text{H}_2}, (\sigma_z/\sigma_R)_*, (\sigma_z/\sigma_R)_g, (\sigma_z/\sigma_R)_{\text{HI}}, (\sigma_z/\sigma_R)_{\text{H}_2}, \\ &\Sigma_*, \Sigma_g, \Sigma_{\text{HI}}, \Sigma_{\text{H}_2}, G, \kappa \end{aligned} \quad (3.4)$$

Like Romeo & Falstad (2013) we estimate  $\sigma_*$  with the help of equation B3 in Leroy et al. (2008):

$$\sigma_{*,z} = \sqrt{\frac{2\pi Gl_*}{7.3} \Sigma_*^{0.5}}, \quad (3.5)$$

where  $l_*$  is the stellar scale length for the galactic disc.

Statistically speaking, the stellar surface density decreases as  $\Sigma_* \propto \exp(-R/l_*)$  with the radius  $R$ . If the galactic disc is self-gravitating and locally isothermal in the vertical direction, then in the limit  $|z| \rightarrow +\infty$  the stellar volume density  $\rho_*$  also decreases exponentially as  $\rho_* \propto \exp(-|z|/h_*)$  with the height  $z$  (see equation 3 in Romeo 1992). To derive (3.5) Leroy et al. (2008) have assumed that the stellar scale height  $h_*$  is independent of  $R$  and that  $l_*/h_* = 7.3 \pm 2.2$ . In addition, they have assumed that the galactic discs are isothermal in the  $z$ -direction, which allows them to use equations based on hydrostatic equilibrium to derive (3.5). Moreover, they take  $(\sigma_z/\sigma_R)_* = 0.6$ , and insertion of this into (3.5) gives

$$\sigma_* = \frac{1}{0.6} \sqrt{\frac{2\pi Gl_*}{7.3} \Sigma_*^{0.5}}, \quad (3.6)$$

where  $\sigma_*$  as before denotes the radial stellar velocity dispersion.

This approximation of  $\sigma_*$  is discussed in section 5.2. The reason for why Leroy et al. (2008) use (3.6) to estimate  $\sigma_*$  is that direct observations of this quantity are rare for galaxies in general and non-existing for the THINGS galaxies in particular. To compute  $\sigma_*$  using (3.6) we need the values of  $l_*$  and  $\Sigma_*$ , which are given in the electronic version of table 4 and 7, respectively, in Leroy et al. (2008).

Next, like Romeo & Falstad (2013) and Leroy et al. (2008) we take the velocity dispersions of the gaseous components to be constants with the values  $\sigma_g = \sigma_{\text{HI}} = 11$  km/s and  $\sigma_{\text{H}_2} = 6$  km/s. As Romeo & Falstad (2013) explain it is also natural to let  $(\sigma_z/\sigma_R)_g = (\sigma_z/\sigma_R)_{\text{HI}} = (\sigma_z/\sigma_R)_{\text{H}_2} = 1$  since collisional components should have isotropic velocity dispersions.

Just as for  $\Sigma_*$ , radial profiles of  $\Sigma_{\text{HI}}$  are given for both the dwarfs and the spirals in the electronic version of table 7 in Leroy et al. (2008). Radial profiles of  $\Sigma_{\text{H}_2}$  are also given for the spirals, but not for the dwarfs. Since there is no data on  $\Sigma_{\text{H}_2}$  for the dwarfs we estimate the value of this parameter for these galaxies as (see equation 28 in Leroy et al. 2008)

$$\Sigma_{\text{H}_2} \approx \frac{10^{-6} \Sigma_{\text{SFR}}}{5.25 \times 10^{-10} \text{yr}^{-1}}, \quad (3.7)$$

where  $\Sigma_{\text{SFR}} \equiv d\Sigma_{\star}/dt$  is the star formation rate surface density.

This formula is based on an empirical power law relationship with index  $1.0 \pm 0.2$ , i.e. a linear relationship, between  $\Sigma_{\text{SFR}}$  and  $\Sigma_{\text{H}_2}$  found by Bigiel et al. (2008) for their subsample of seven large THINGS spiral galaxies. Leroy et al. (2008) extended this result by showing that for their subsample of 12 large THINGS spiral galaxies, which include those studied by Bigiel et al. (2008), the star formation efficiency of  $\text{H}_2$ ,  $\text{SFE}(\text{H}_2) \equiv \Sigma_{\text{SFR}}/\Sigma_{\text{H}_2}$ , varies relatively little with  $R$ ,  $\Sigma_{\text{g}}$ ,  $\Sigma_{\star}$  and several other parameters where the ISM is dominated by  $\text{H}_2$ . They also computed the constant 5.25 ( $\pm 2.5$ ) in equation (3.7) (see equation 27 in Leroy et al. 2008).

Note that by using equation (3.7) to estimate  $\Sigma_{\text{H}_2}$  for the dwarfs we are implicitly assuming that this relation is approximately true for these galaxies as well – not only where the ISM is dominated by  $\text{H}_2$  but at *all* radii. This is a big leap of faith! Also note that the powers of 10 in equation (3.7) are merely meant to convert between different units. In the units used in the electronic version of table 7 in Leroy et al. (2008) equation (3.7) simplifies to  $\Sigma_{\text{H}_2} \approx \Sigma_{\text{SFR}}/5.25$ .

Next, we used  $G = 4.301 \text{ m}^2\text{kpc/s}^2/\text{M}_{\odot}$ . With the gravitational constant in this unit one can directly insert the tabular values of  $l_{\star}$  and  $\Sigma_{\star}$  into equation (3.7), without changing their units, to obtain  $\sigma_{\star}$  in km/s. If in addition  $\kappa$  and  $\sigma_i$  have the units km/s/kpc and km/s, respectively, then equation (2.3) also gives the Toomre (1964) parameter directly from the tabulated surface densities.

The epicyclic frequency was calculated from equation 13 and B1 in Leroy et al. (2008), which give that

$$\kappa(R) = 1.41 \frac{v_{\text{rot}}(R)}{R} \sqrt{1 + \beta} \quad (3.8)$$

$$v_{\text{rot}}(R) = v_{\text{flat}} \left[ 1 - \exp\left(\frac{-R}{l_{\text{flat}}}\right) \right] \quad (3.9)$$

$$\beta(R) = \frac{R/l_{\text{flat}}}{\exp(R/l_{\text{flat}}) - 1} \quad (3.10)$$

where  $v_{\text{flat}}$  and  $l_{\text{flat}}$  are parameters obtained from fitting the rotation curve to an exponentially decreasing function on the form (3.9). The values of  $v_{\text{flat}}$  and  $l_{\text{flat}}$  are given in the electronic version of table 4 in Leroy et al. (2008). Note that equation (3.10) is not given in Leroy et al. (2008). It was calculated from (3.9) using the definition of  $\beta$  as the logarithmic derivative of the rotation curve, i.e.  $\beta \equiv d(\ln v_{\text{rot}})/d(\ln R)$ .

Also note that the dwarf galaxies NGC 4449 and NGC 3077, which are listed within parentheses in table 2.1, have complicated rotation curves which cannot be fitted well by functions on the form (3.9). These two galaxies were therefore excluded from both the stability analysis of Leroy et al. (2008) as well as ours. The reason for their strange kinematics is that NGC 4449 has a counter-rotating core and NGC 3077 is interacting with the galaxy M81. (Leroy et al. 2008)

Moreover, it should be mentioned that interstellar gas consists of about 74% hydrogen and 26% helium on an average. Other elements are present only in very small amounts. To account for the helium, which cannot be directly observed, Leroy et al. (2008) included a factor  $1.36 \approx 1/0.74$  in their tabulated values of  $\Sigma_{\text{H}_1}$  and  $\Sigma_{\text{H}_2}$ . This makes  $\Sigma_{\text{g}}$  the *total* surface density of gas, rather than merely the hydrogen surface density.

### 3.1.2 Observational data

The most basic physical quantities in the electronic tables of Leroy et al. (2008) are:  $\Sigma_\star$ ,  $\Sigma_{\text{HI}}$ ,  $\Sigma_{\text{H}_2}$  (spirals only),  $\Sigma_{\text{SFR}}$  and  $v_{\text{rot}}$ . From these one can compute for instance  $v_{\text{flat}}$ ,  $l_{\text{flat}}$ ,  $l_\star$ , the optical radius  $R_{25}$ , etc. Let us therefore briefly mention how Leroy et al. (2008) derived the basic quantities.

The stellar surface density was determined from *Spitzer* (mostly SINGS)  $3.6\ \mu\text{m}$  intensity maps. The median intensity over  $10''$  wide tilted rings was computed and radial profiles of the median were constructed. These profiles were used to compute the K-band intensity (the K-band is centered at  $2.2\ \mu\text{m}$ ) via an empirical formula. Then a fixed K-band mass-to-light ratio  $\Upsilon_\star^K = 0.5\ \text{M}_\odot/\text{L}_{\odot,\text{K}}$  was used to convert the K-band intensity to stellar mass. Divided by the area this gives  $\Sigma_\star$ . After correcting for the inclination  $i$  the formula for  $\Sigma_\star$  in  $\text{M}_\odot/\text{pc}^2$  becomes (see equation C1 in Leroy et al. 2008)

$$\Sigma_\star = 280 \cos i I_{3.6}, \quad (3.11)$$

where  $I_{3.6}$  is the  $3.6\ \mu\text{m}$  intensity in the unit MJy/ster.

Next, the HI surface density was determined from THINGS 21 cm line emission maps. The formula used was (see equation A1 in Leroy et al. 2008)

$$\Sigma_{\text{HI}}(\text{M}_\odot\text{pc}^{-2}) = 0.020 \cos i I_{21\text{cm}}(\text{K km s}^{-1}), \quad (3.12)$$

where  $I_{21\text{cm}}$  is the integrated intensity of the 21 cm line and the expressions within parentheses are the units for  $\Sigma_{\text{HI}}$  and  $I_{21\text{cm}}$ . Note that this formula includes a factor 1.36 to account for the presence of helium.

For the spirals the  $\text{H}_2$  surface density was estimated using CO as a tracer. HERACLES provided maps of the CO  $J = 2 \rightarrow 1$  emission for all the spirals except NGC 3627 and NGC 5194, where  $J$  is the total angular momentum quantum number. For the latter galaxies BIMA SONG supplied CO  $J = 1 \rightarrow 0$  maps. By assuming a constant CO-to- $\text{H}_2$  conversion factor  $X_{\text{CO}} = 2 \times 10^{20}\ \text{cm}^{-2}(\text{K km s}^{-1})^{-1}$ , and a relation  $I_{\text{CO}}(2 \rightarrow 1) = 0.8 I_{\text{CO}}(1 \rightarrow 0)$ , Leroy et al. (2008) could compute  $\Sigma_{\text{H}_2}$  from the integrated CO intensities  $I_{\text{CO}}(2 \rightarrow 1)$  and  $I_{\text{CO}}(1 \rightarrow 0)$  with the formulas (see equation A2 and A3 in Leroy et al. 2008)

$$\Sigma_{\text{H}_2}(\text{M}_\odot\text{pc}^{-2}) = 5.5 \cos i I_{\text{CO}}(2 \rightarrow 1)(\text{K km s}^{-1}) \quad (3.13)$$

$$\Sigma_{\text{H}_2}(\text{M}_\odot\text{pc}^{-2}) = 4.4 \cos i I_{\text{CO}}(1 \rightarrow 0)(\text{K km s}^{-1}) \quad (3.14)$$

According to Leroy et al. (2008) the CO-emission from very low-mass galaxies is usually weak or not detected and its interpretation is complicated by potential variations in  $X_{\text{CO}}$ . This is the reason for why they do not provide tabulated values of  $\Sigma_{\text{H}_2}$  for the dwarfs.

The star formation rate surface density was estimated from *GALEX* NGS far-ultraviolet (FUV) maps and *Spitzer*  $24\ \mu\text{m}$  maps. According to Leroy et al. (2008), this combination traces both unobscured (FUV) and dust embedded ( $24\ \mu\text{m}$ ) star formation. The formula they used is (see equation D1 in Leroy et al. 2008)

$$\Sigma_{\text{SFR}} = \left( 8.1 \times 10^{-2} I_{\text{FUV}} + 3.2_{-0.7}^{+1.2} \times 10^{-3} I_{24} \right) \cos i, \quad (3.15)$$

where  $\Sigma_{\text{SFR}}$  has the unit  $\text{M}_\odot\text{kpc}^{-2}\text{yr}^{-1}$  and the intensities have the unit MJy/ster.

Next, the rotation velocity was determined from THINGS mean intensity weighted velocities  $v_r$  and the formula (see equation B2 in Leroy et al. 2008)

$$v_{\text{rot}} = \frac{v_r - v_{\text{sys}}}{\sin i \cos \theta}, \quad (3.16)$$

where  $v_{\text{sys}}$  is the systemic velocity and  $\theta$  is the azimuthal angle relative to the receding major axis measured in the plane of the galaxy. Maps of  $v_{\text{rot}}$  were assembled and the median in  $5''$  wide tilted rings computed to give radial profiles of  $v_{\text{rot}}$ . These profiles were weighted by the scatter in the rings and fitted to functions on the form (3.9) using a non-linear least squares method to provide values of  $v_{\text{flat}}$  and  $l_{\text{flat}}$  for each galaxy. For as many of the galaxies as possible high-quality rotation curves from de Blok et al. (2008) were also included in the fit.

Finally, it should be mentioned that Leroy et al. (2008) have placed all data at a common spatial resolution of 400 pc for the dwarfs and 800 pc for the spirals. This means that they have used Gaussian functions to degrade data with higher spatial resolution to ensure that all data have the same resolution. This is equivalent to placing all the dwarfs and all the spirals at an equal distance, respectively. Note that the spirals are larger than the dwarfs but they are also at larger distances, so the number of resolution elements per galaxy is about the same for all the galaxies. Leroy et al. (2008) have also used a working sensitivity of  $1 \text{ M}_{\odot} \text{pc}^{-2}$  for  $\Sigma_{\text{H}_1}$  and  $\Sigma_{\text{H}_2}$  and  $10^{-4} \text{ M}_{\odot} \text{yr}^{-1} \text{kpc}^{-2}$  for  $\Sigma_{\text{SFR}}$ , which means that they have removed all data with values below the working sensitivities. This is important since the data would otherwise have different sensitivities and one would not know how to interpret a missing value in the electronic version of table 7 in Leroy et al. (2008).

## 3.2 Scatter plots of $Q_N$ vs. galactocentric distance

Scatter plots of  $Q_N$  for the three cases described at the beginning of section 3.1 are shown in figure 3.1 for the dwarfs and the spirals separately. In all six plots  $Q_N$  is plotted as a function of the normalized galactocentric distance  $R/R_{25}$ , and the grey area shows the region of local gravitational instability. The values of  $R_{25}$  were taken from the electronic version of table 4 in Leroy et al. (2008). The plots of  $Q_2$  with  $\text{H}_2$  and  $Q_3$  for the spirals show the same data points as the two plots in figure 4 of Romeo & Falstad (2013), except for the addition of the empty squares in the former plots. Several other plots in Romeo & Falstad (2013) have been reproduced in this thesis with permission from the authors.

The colors of the points in figure 3.1 show which component dominates  $Q_N$ , i.e. has the smallest value of  $TQ$ , at each point. The symbols indicate the amount of gaseous data available. Points with non-vanishing values of both  $\Sigma_{\text{H}_1}$  and  $\Sigma_{\text{H}_2}$  are denoted by circles, point with non-vanishing values of  $\Sigma_{\text{H}_1}$  but not  $\Sigma_{\text{H}_2}$  or vice versa are denoted by diamonds and plus-signs, respectively, and points with vanishing values of both  $\Sigma_{\text{H}_1}$  and  $\Sigma_{\text{H}_2}$  are denoted by empty squares. Note that the symbols have the same significance in all the plots of, or related to,  $Q_N$  in this thesis. Also note that in the PDF-version of this thesis all figures have vector graphics, and the reader is therefore encouraged to enlarge the plots and study the shapes and colors of individual points and error-bars.

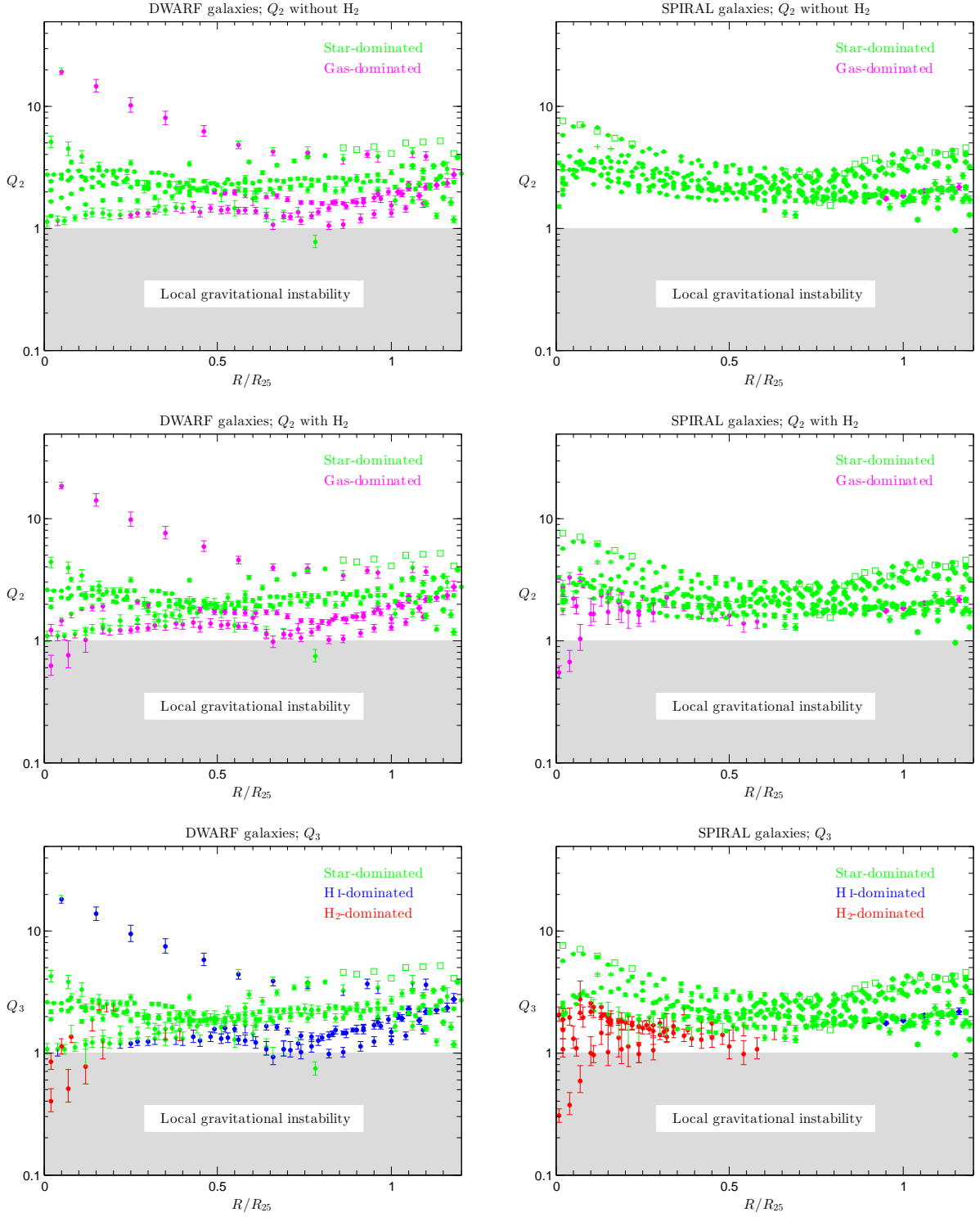


Figure 3.1: Scatter plots of  $Q_2$  without  $H_2$ ,  $Q_2$  with  $H_2$  and  $Q_3$  for the dwarfs (left) and spirals (right). The meaning of the colors and symbols in these plots are explained in the main text.

Moreover, the error-bars in figure 3.1, as well as the error-bars in all other figures in this thesis, have been computed using the same methods as in Romeo & Falstad (2013). The details of the error analysis are given in appendix B together with an alternative method of computing the error-bars for  $Q_N$ . In the present context it is sufficient to say that the error analysis is very complicated for  $Q_N$  and that the main reason for this is that  $Q_N$  is not differentiable at points where the dominant component changes, i.e. where the index  $m$  in equation 2.4 changes value.

It should also be mentioned that each point in figure 3.1 has three associated values of  $Q_N$ : a nominal value computed from observational data, and a lower and an upper value indicating the uncertainty of  $Q_N$ . The end-points of the error-bars show an estimation of the latter two values, and the colors of the error-bars show the dominant components for these points. However, the reader should be aware that there exists no method of calculating the exact value of the standard deviation  $\sigma$  of  $Q_N$  and that the error-bars in figure 3.1 do not show  $Q_N \pm \sigma$ . In fact, the error-bars are asymmetric and it is shown in appendix B that the density function of  $Q_N$  is asymmetric as well – in particular near point where the  $m$ -value changes.

The error-bars are not shown for the square points in figure 3.1 since they are inside the squares. These points were excluded from the analysis of the spirals in Romeo & Falstad (2013) since they cannot be placed in the  $(s, q)$  plane, which will be introduced in section 5.1. Also, some of these points have vanishing values of  $\Sigma_{\text{H}_2}$  at small radii, where there should be plenty of  $\text{H}_2$  in the spirals. This is more likely due to observational difficulties rather than real deficiencies in  $\text{H}_2$ , which makes these points very uncertain. For the dwarfs there are only square points at large radii where we expect the surface densities of both  $\Sigma_{\text{H}_1}$  and  $\Sigma_{\text{H}_2}$  to be below the working sensitivity of Leroy et al. (2008). Nevertheless, to ensure that the dwarfs are treated in precisely the same manner as the spirals we have excluded the square points from the stability analysis for both subsamples in this thesis. In the only computation where these points are considered this is stated explicitly, and in appendix B we also show that including the square points has a negligible effect on the results.

Let us now analyze figure 3.1. The first thing that one notices is that most of the data points in these six plots lay on bands slightly above the region of instability. For the dwarfs this band is relatively close to the grey region, while for the spirals there is a small but tangible gap between the lower edge of the band and the grey area. The second thing that one notices is that when we move from the top plots to the middle ones and then to the bottom plots, the data points are lowered in general and gas-dominated points appear at small radii with relatively low  $Q_N$ -values in particular.

The second observation can be understood by inspection of equation (2.2) and (2.3). Since  $Q_g \propto 1/\Sigma_g$  adding  $\Sigma_{\text{H}_2}$  to  $\Sigma_g$  decreases the value of  $Q_g$ , which in turn increases the value of  $1/Q_2$ , i.e. decreases the value of  $Q_2$ . The value of  $T_g Q_g$  is also lowered, while  $T_\star Q_\star$  is unaffected. This tends to make star-dominated points gas-dominated. These effects are most pronounced in regions with a lot of  $\text{H}_2$ , i.e. near the centers of the galaxies<sup>1</sup>. Also, since  $Q_i \propto \sigma_i$  and  $\sigma_{\text{H}_2} < \sigma_{\text{H}_1}$ , treating  $\text{H}_2$  as a separate component has similar effects.

If we compare the two plots of  $Q_3$  we also see that there is a difference in both

---

<sup>1</sup>Radial profiles of  $\Sigma_{\text{H}_2}$  and several other quantities are shown for individual galaxies in appendix A.

the distribution and nature of the gas-dominated points between the dwarfs and the spirals. For the dwarfs there are gas-dominated points at all radii, with a slightly higher concentration at  $R/R_{25} \gtrsim 0.5$ , while for the spirals nearly all the gas-dominated points have  $R/R_{25} \lesssim 0.6$ . Also, the gas-dominated points in the dwarfs are H I-dominated, except for a few points at small radii, while the gas-dominated points in the spirals are H<sub>2</sub>-dominated, except for a few points at large radii. The latter observation was expected since the dwarfs and the spirals are rich in H I and H<sub>2</sub>, respectively.

Moreover, we see in the plot of  $Q_3$  for the dwarfs that there is a string of H I-dominated points with relatively large  $Q_3$ -values at  $0 \lesssim R/R_{25} \lesssim 0.7$ . These points belong to the irregular galaxy Holmberg I (Ho I), which has a central ‘hole’ in its H I-distribution. According to Ott et al. (2001), most of the atomic hydrogen in Ho I is located in a supergiant shell, and they suggest that this shell might have been formed by strong stellar winds and supernova explosions which have driven the H I away from the center of the galaxy. However, they also point out that there exists little observational evidence that stars are the cause of such superbubbles or supergiant shells.

Regardless of the origin of the H I-shell it remains an observational fact that both  $\Sigma_\star$  and  $\Sigma_{\text{SFR}}$  have very low values in the central parts of Ho I. One might suspect that this is due to the low values of  $\Sigma_{\text{H I}}$  there since star form from H<sub>2</sub>, which in turn forms from H I. Due to the absence of stars we do not expect  $Q_3$  to be star-dominated at small radii in Ho I, and since  $Q_{\text{H I}} \propto 1/\Sigma_{\text{H I}}$  we also expect  $Q_3$  to have high values there (see equation (2.2) and (2.3)). This is precisely what we see in the bottom left plot in figure 3.1.

Next, let us comment on the H<sub>2</sub>-dominated points at small radii in the plot of  $Q_3$  for the dwarfs. The three points with the smallest values of  $Q_3$  belong to NGC 4214, which has a central starburst (see for instance Fanelli et al. 1997), i.e.  $\Sigma_{\text{SFR}}$  is very high in the central parts of this galaxy. Intuitively this seems to correspond well with the small  $Q_3$ -values there. However, NGC 4214 is morphologically classified as an irregular galaxy with a weak bar in the NASA/IPAC Extragalactic Database (NED)<sup>2</sup>, and the method of calculating with values averaged over tilted rings used by Leroy et al. (2008) does not work well with bars. The reason for this is that the conditions inside bars are very different from the conditions in their surroundings, so the average or median value over a tilted ring passing a bar neither represents the properties of the bar nor its surrounding very well.

It should also be mentioned that we assumed a fixed value of  $\sigma_{\text{H}_2}$ , but in reality the velocity dispersion increases towards the center of a galaxy. We see in equation (2.2) and (2.3) that a larger value of  $\sigma_{\text{H}_2}$  implies a larger value of  $Q_{\text{H}_2}$  and thus also a larger value of  $Q_3$ . It is therefore possible that the H<sub>2</sub>-dominated points in NGC 4214 have larger  $Q_3$ -values than those shown in figure 3.1. Moreover, one should not necessarily expect a starburst region to have very low values of  $Q_3$ . There may be self-regulation mechanisms which prevent the value of  $Q_3$  from falling much below one. This is easy to understand since gravitational instabilities try to collapse gas clouds, which heats them up. This in turn increases the velocity dispersion of the gas, which leads to higher values of  $Q_3$ . Interestingly enough, the heating of the gas also increases the gas dissipation, which lowers

---

<sup>2</sup>This research has made use of the NASA/IPAC Extragalactic Database (NED) which is operated by the Jet Propulsion Laboratory, California Institute of Technology, under contract with the National Aeronautics and Space Administration.

the temperature as well as the velocity dispersion and  $Q_3$ . Due to such self-regulation mechanisms a starburst region may therefore oscillate around  $Q_3 = 1$ , i.e. it could be *marginally stable*.

Finally, the remaining three  $H_2$ -dominated points at small radii in the plot of  $Q_3$  for the dwarfs belong to NGC 925, which is a *barred* spiral galaxy, so the discussion above applies to these points as well. One should also mention that there are a few points in this plot with  $Q_3 < 1$  at  $0.6 \lesssim R/R_{25} \lesssim 0.9$ . These points belong to galaxy 3 and 4 in table 2.1, and there is not much else to say about them.

### 3.3 Stability properties as functions of galactocentric distance

The two upper plots in figure 3.2 show the median of  $Q_N$  as a function of galactocentric distance  $R/R_{25}$  for the same three cases as before for the dwarfs and the spirals separately. The two lower plots show the percentage of data points in each bin dominated by stars and gas, respectively, as well as the percentage of points with  $Q_N < 1$ . In all four plots 12 bins  $b_1, \dots, b_{12}$  were used with the limits  $0.1(i-1) < b_i \leq 0.1i$ ,  $i = 1, 2, \dots, 12$ . Note that changing the limits to  $0.1(i-1) \leq b_i < 0.1i$  makes a difference since some of the data points lay precisely on the borders between bins. However, this is a relatively small effect with no qualitative impact on the results.

We see in figure 3.2 that the median of  $Q_3$  is almost constant with a value of about 2 for both the dwarfs and the spirals. We also see that in all three cases the percentage of gas-dominated points steadily decreases with  $R/R_{25}$  for the spirals, while it instead increases for the dwarfs up to  $R/R_{25} \approx 0.95$  and then it decreases rapidly. This is more or less what we would expect from an inspection of the two bottom plots in figure 3.1. Figure 3.3 shows schematically at which galactocentric distances the majority of the  $Q_3$ -points are dominated by stars and gas, respectively, for the two subsamples.

Note that the median of  $Q_3$  is below the median of  $Q_2$  with  $H_2$ , which in turn is below the median of  $Q_2$  without  $H_2$ . This is in full agreement with the discussion in section 3.2. However, it is a bit surprising that the median of  $Q_2$  with  $H_2$  is so close to the median of  $Q_3$  for the dwarfs. The reason for this is that there is relatively little  $H_2$  in the dwarfs compared to the spirals. In general, treating  $H_2$  as a separate component has very little impact if  $\Sigma_{H_2}$  has a small value. In particular, it has a negligible impact on star-dominated points, and we can tell by inspection of figure 3.1 that the median of  $Q_2$  with  $H_2$  and  $Q_3$  are both star-dominated<sup>3</sup> at almost all radii for the dwarfs. The same is true for the median of  $Q_2$  with  $H_2$  for the spirals, but at small galactocentric distances the median of  $Q_3$  is obviously  $H_2$ -dominated for the spirals. This ensures that there will be a large difference between  $Q_2$  with  $H_2$  and  $Q_3$  at small  $R/R_{25}$  for the spirals, and this is precisely what we see in figure 3.2.

---

<sup>3</sup>For an even number of data points in a bin the median is the average value of the two middlemost  $Q_N$ -values. In this case the median of  $Q_N$  does not correspond to a single point and consequently does not have a dominant component. However, if the two middlemost points are both star-dominated then the median may be thought of as a star-dominated point as well.

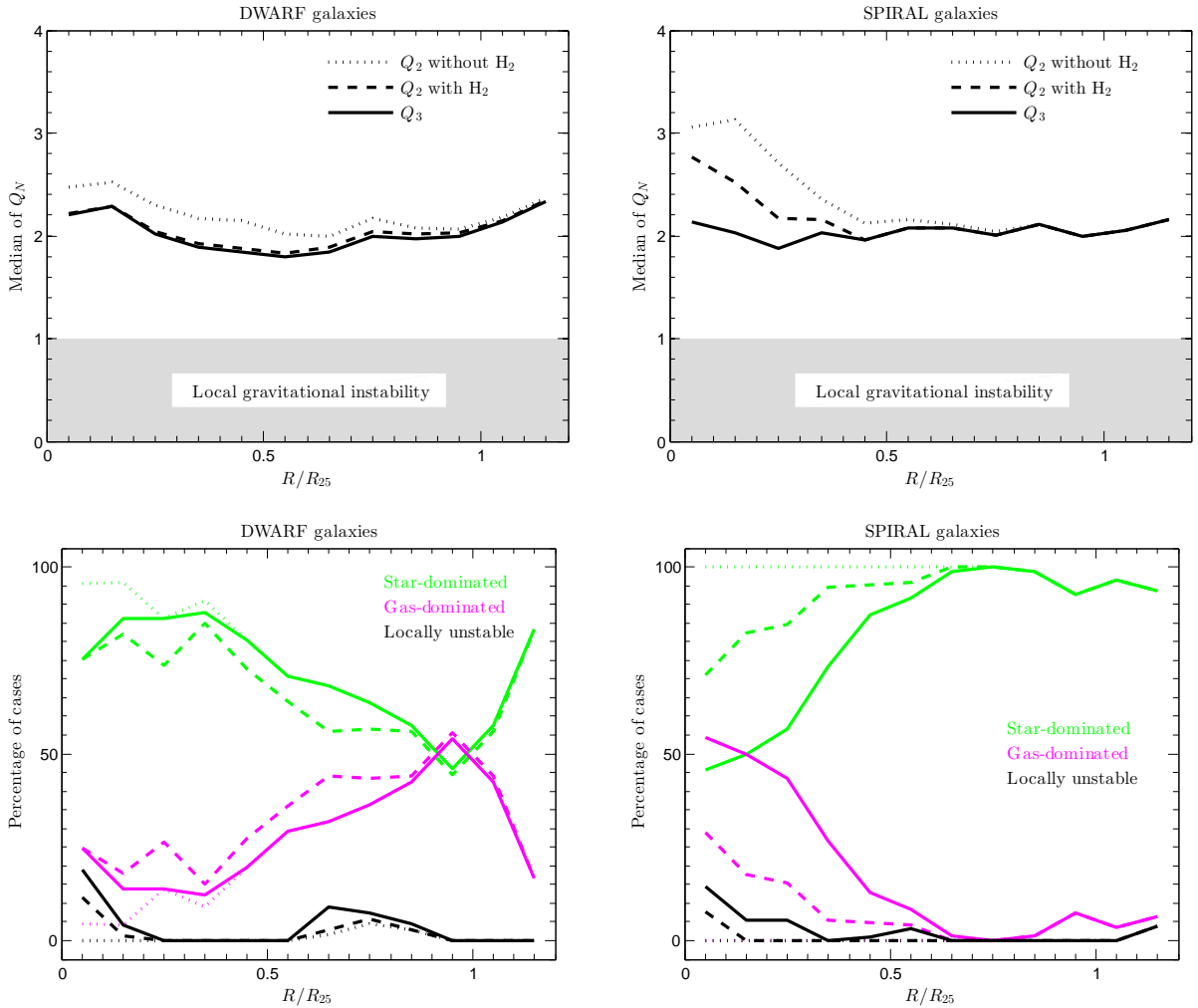


Figure 3.2: The two upper plots show the median of  $Q_N$  as a function of galactocentric distance  $R/R_{25}$  for the three standard cases for the dwarfs (left) and the spirals (right). The two lower plots show the percentage of data points in each bin dominated by stars and gas, respectively, as well as the percentage of points with  $Q_N < 1$ .

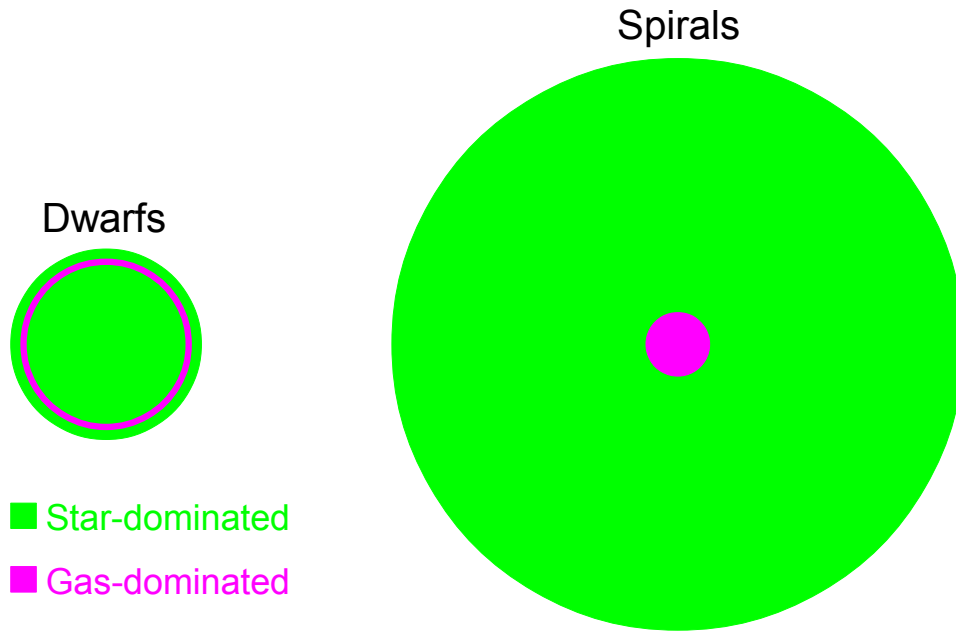


Figure 3.3: A sketch of where in the interval  $0 \leq R/R_{25} \leq 1.2$  the majority of the  $Q_3$ -points are dominated by stars and gas, respectively, for the two subsamples. Note that the figure is not in scale.



# Chapter 4

## Searching for physical correlations

Attempts were made to find correlations involving  $\Sigma_{\text{SFR}}$ . Figure 4.1 shows scatter plots of  $\Sigma_{\text{SFR}}$  as a function of galactocentric distance for the dwarfs and the spirals, respectively. It also shows the median of  $\Sigma_{\text{SFR}}$  for the two subsamples, computed using the same bin-limits as for figure 3.2. Note that one usually also computes the  $1\sigma$ -scatter for the (sub)samples about the median as  $\sigma \simeq \text{MAD}/0.6745$  (see equation 10 in Romeo, Horellou & Bergh 2004), where MAD stands for Median Absolute Deviation. However, in this case  $\text{MAD}/0.6745$  is not a robust estimator of the  $1\sigma$ -scatter since the scatter plots of  $\Sigma_{\text{SFR}}$  suggest that the distribution of this quantity is both skewed and multimodal. The former means that it is not symmetric with respect to the median and the latter means that the data points tend to concentrate around more than one value of  $\Sigma_{\text{SFR}}$  for a fixed value of  $R/R_{25}$ .

We also see in the scatter plots of  $\Sigma_{\text{SFR}}$  that there are large empty areas inside the distributions. For the dwarfs there are several such areas in the interval  $0 \lesssim R/R_{25} \lesssim 0.6$ , and for the spirals there is one particularly large empty area stretching from  $R/R_{25} \approx 0.4$  to  $R/R_{25} \approx 1.1$ . This could simply be a consequence of the smallness of the subsamples, i.e. if there were more galaxies then the extra data points might have filled the empty spaces. However, these areas could also be a result of how the THINGS sample was selected. For any statistical analysis the sample must be selected at random, but the THINGS galaxies were purposely selected to represent a wide variety of physical properties. In making such a choice one always risk biasing the sample, regardless of by which criteria it is chosen. In other words: the THINGS sample might not be representative of the natural mixture of galaxies in the nearby Universe. The fact that the relative scatter of  $\Sigma_{\text{SFR}}$  is rather small for the dwarfs at  $R/R_{25} \gtrsim 0.6$  could also be an effect of how these galaxies were selected.

Be that as it may, we see that the logarithm of the median of  $\Sigma_{\text{SFR}}$  is almost a linear function of galactocentric distance for both subsamples, i.e.  $\Sigma_{\text{SFR}}$  seems to decrease exponentially with  $R/R_{25}$  in a statistical sense. We also see that there is an offset between the two lines such that the median of  $\Sigma_{\text{SFR}}$  has larger values at small galactocentric distances for the spirals than for the dwarfs. This is not surprising considering that more stars are formed at the center of large spiral galaxies than at the center of dwarf galaxies. Moreover, we also see that the median of  $\Sigma_{\text{SFR}}$  has a larger negative tilt for the spirals than for the dwarfs.

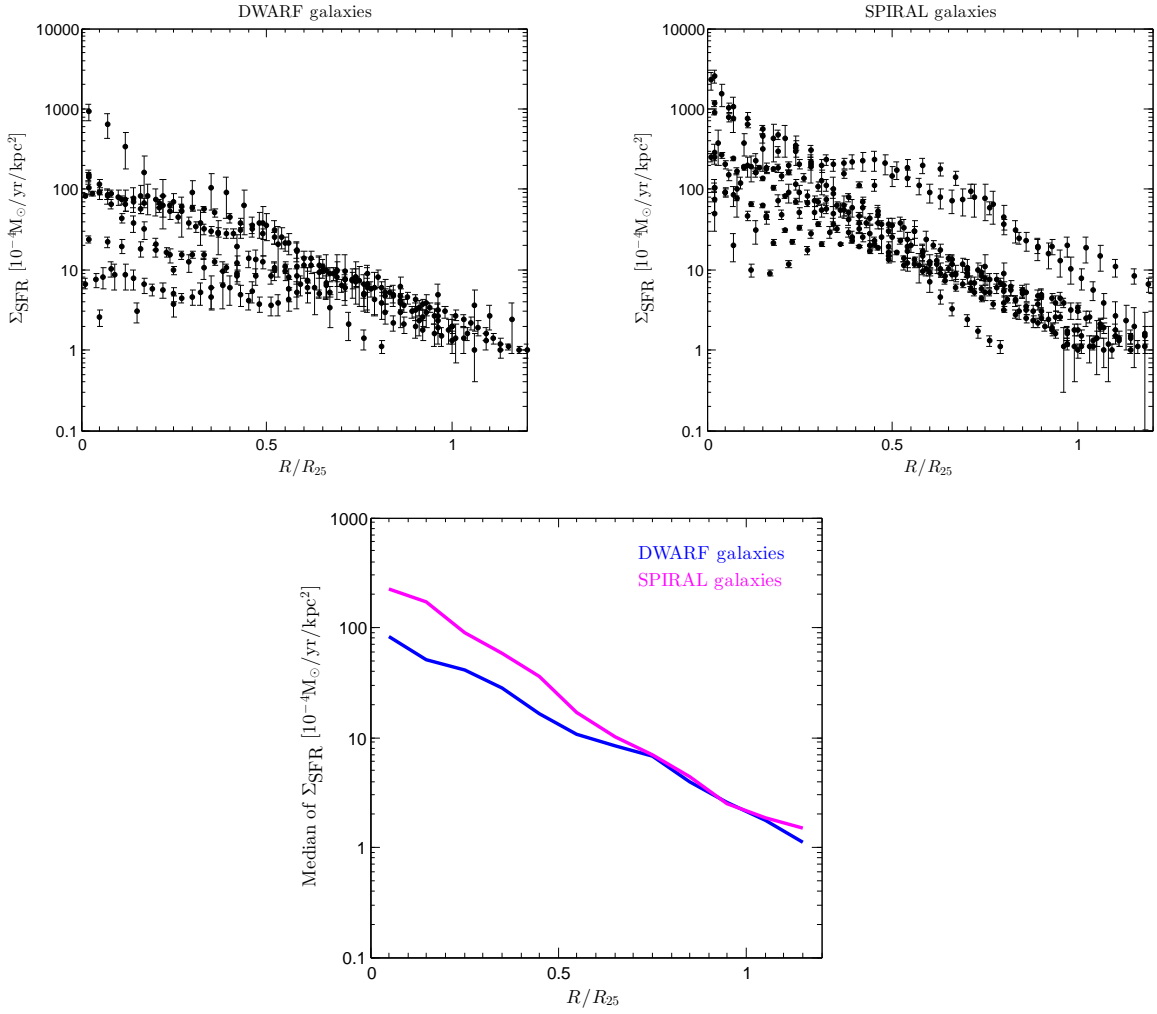


Figure 4.1: Scatter plots of  $\Sigma_{\text{SFR}}$  as a function of galactocentric distance for the dwarfs (upper-left) and the spirals (upper-right), and the median of  $\Sigma_{\text{SFR}}$  for the two subsamples (lower).

Unfortunately, we cannot put too much faith in the median of  $\Sigma_{\text{SFR}}$ ; at least not for the dwarfs. The reason for this is that it is not robust. This is shown in figure 4.2, where we investigate the impact on the median of  $\Sigma_{\text{SFR}}$  for the dwarfs from removing either NGC 7793 or NGC 2403, or both, from the dwarf subsample. We see that removing either of these galaxies lowers the median significantly in the interval  $0.2 \lesssim R/R_{25} \lesssim 0.4$ , and that removing both of them also lowers the median by about a factor 2–4 at  $R/R_{25} \lesssim 0.2$ . The reason for why the median of  $\Sigma_{\text{SFR}}$  depends so strongly on these two galaxies is that they both have radial profiles of  $\Sigma_{\text{SFR}}$  which are almost identical to that of the median, i.e. they strongly support the median at all values of  $R/R_{25}$ .

Next, in an attempt to find a connection between  $\Sigma_{\text{SFR}}$  and  $Q_N$  we have repeated some of the steps in the analysis of Westfall et al. (2014). They investigate the relationship between disc stability and star formation for 25 galaxies from the DiskMass Survey. They find, with a confidence level of over 99%, that the *effective* star formation rate surface density is anti-correlated with the minimum value of  $Q_2$  with  $\text{H}_2$  on the interval  $0.1 \leq R/l_\star \leq 2.5$ . We denote the former quantity by  $\bar{\Sigma}_{\text{SFR}}$  and the latter by  $Q_2^{\text{min}}$ .  $\bar{\Sigma}_{\text{SFR}}$  is defined as

$$\bar{\Sigma}_{\text{SFR}} \equiv \text{SFR}/(\pi R_{25}^2), \quad (4.1)$$

where  $\text{SFR} \equiv dM_\star/dt$  is the global star formation rate of the galaxy.

Note that  $\bar{\Sigma}_{\text{SFR}}$  is almost, but not quite, equal to the average value of  $\Sigma_{\text{SFR}}$  over the optical disc. Although  $\Sigma_{\text{SFR}}$  decreases rapidly beyond the edge of the optical disc it does not vanish completely for  $R > R_{25}$ . SFR is therefore somewhat larger than the integral of  $\Sigma_{\text{SFR}}$  over the optical disc, which implies that  $\bar{\Sigma}_{\text{SFR}}$  is a bit larger than the average value of  $\Sigma_{\text{SFR}}$  over this disc.

Westfall et al. (2014) use  $Q_2^{\text{min}}$  in order to make their results comparable to those of Li et al. (2006). In their paper from 2005 Li et al. use computer simulations to explore star formation in isolated disc galaxies. They show that at time  $t = 0$  in their simulations the two-component Rafikov (2001) stability parameter  $Q_{\text{sg}}$  for stars and gas has large values at small radii, decreases to a well-defined minimum  $Q_{\text{sg,min}}$  at  $R_{\text{min}}$ , and increases for  $R > R_{\text{min}}$ . In their paper from 2006 they also show that at time  $t = \tau_{\text{SF}}$ , which they call the ‘star formation timescale’,  $\Sigma_{\text{SFR}} \propto [Q_{\text{sg,min}}]^{-1.54 \pm 0.23}$ . It is unclear at which radius  $\Sigma_{\text{SFR}}$  is to be evaluated, but presumably it is at  $R_{\text{min}}$ .

Considering the uncertainty of the observational data,  $Q_2$  with  $\text{H}_2$  is equivalent to  $Q_{\text{sg}}$ , but  $\bar{\Sigma}_{\text{SFR}} \neq \Sigma_{\text{SFR}}(R_{\text{min}})$ . Also, the galaxies explored by Westfall et al. (2014) are different from those simulated by Li et al. (2005, 2006), and Westfall et al. (2014) compute  $\bar{\Sigma}_{\text{SFR}}$  and  $Q_2^{\text{min}}$  for  $t \neq \tau_{\text{SF}}$ . One should therefore not expect to find a very strong agreement between the results of these two studies, and Westfall et al. (2014) indeed find a much steeper power-law slope of about 3 in their data than the slope of  $-1.54$  computed by Li et al. (2006).

In our analysis we tried to find a relation between  $\bar{\Sigma}_{\text{SFR}}$  and the minimum  $Q_N^{\text{min}}$  of  $Q_2$  without  $\text{H}_2$ ,  $Q_2$  with  $\text{H}_2$  and  $Q_3$ , respectively, on the interval  $0.1 \leq R/l_\star \leq 2.5$ . Since our radial profiles of these stability parameters do not have well-defined minima, i.e. they are not convex, we also tried to find a relation between  $\bar{\Sigma}_{\text{SFR}}$  and the median of  $Q_N$  for these three cases. Note that in this analysis the median of  $Q_N$  is the median of all  $Q_N$ -values for a single galaxy, rather than the median of  $Q_N$  at a fixed galactocentric distance marginalized over all galaxies in the subsample as in figure 3.2.

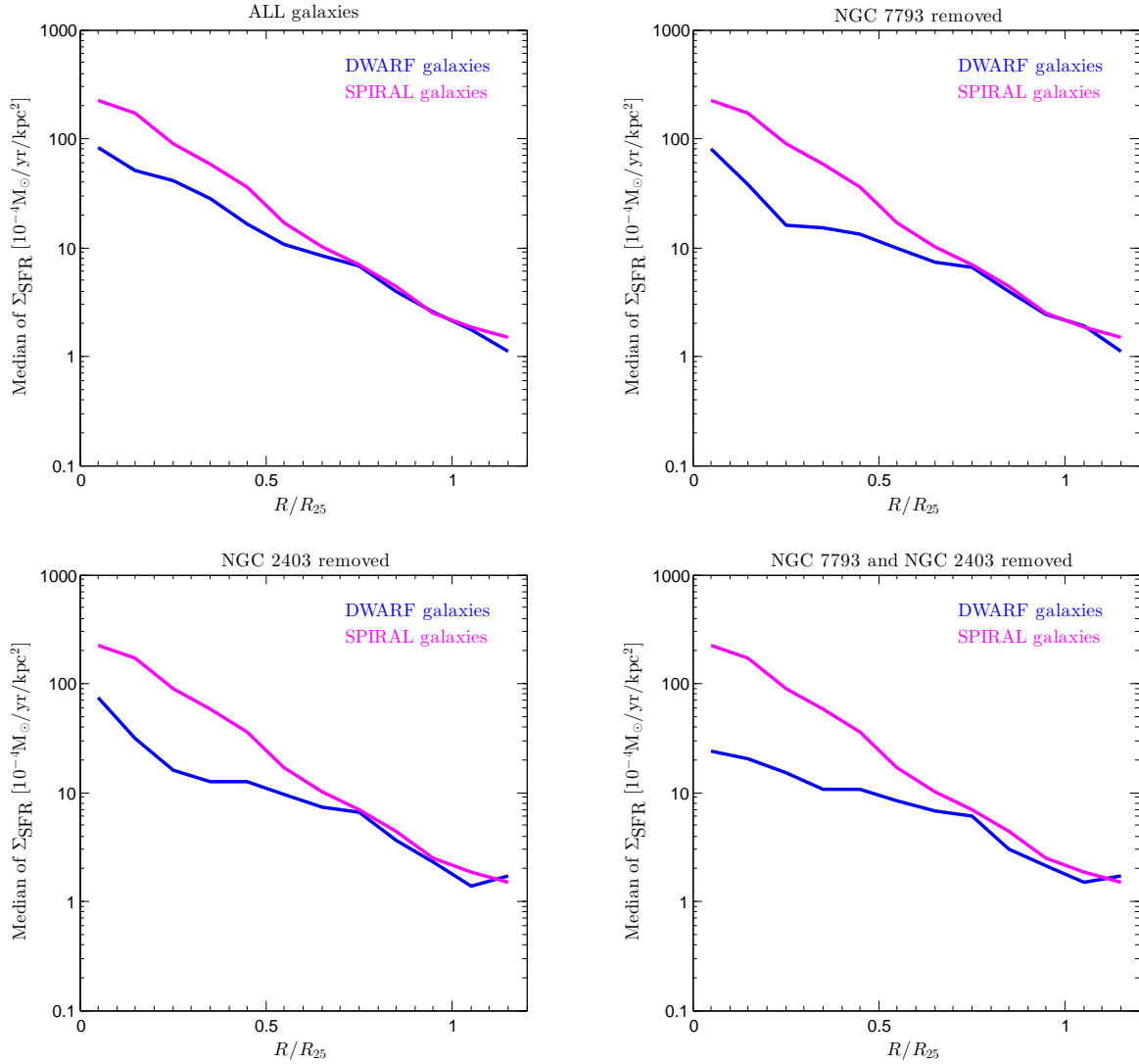


Figure 4.2: The upper-left plot is identical to the lower plot in figure 4.1. The remaining three plots show the effect on the first plot of removing NGC 7793 (upper-right) or NGC 2403 (lower-left), or both (lower-right), from the dwarf subsample.

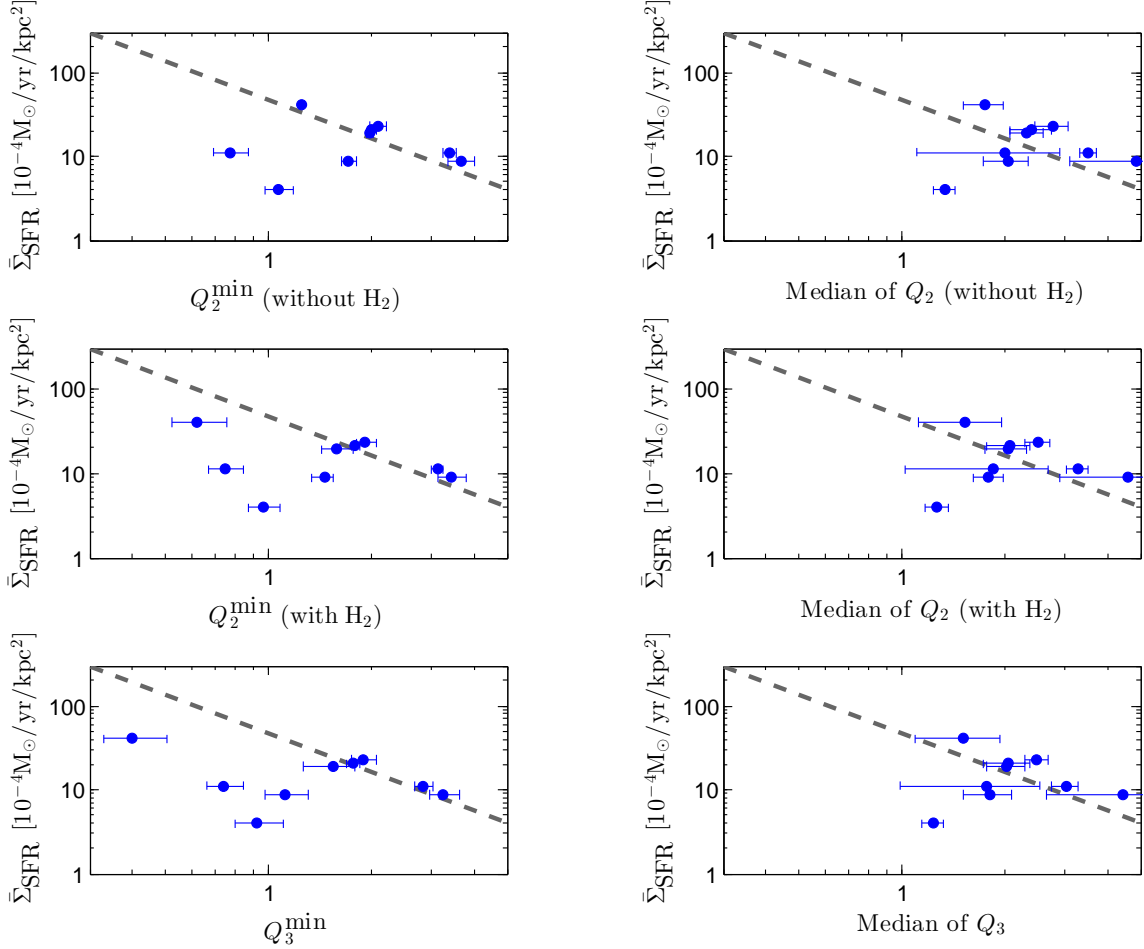


Figure 4.3:  $\bar{\Sigma}_{\text{SFR}}$  as a function of  $Q_N^{\text{min}}$  and the median of  $Q_N$ , respectively, for the three standard cases for the dwarfs.

The values of SFR,  $R_{25}$  and  $l_*$  were taken from the electronic version of table 4 in Leroy et al. (2008), and the results of the computations are shown in figure 4.3 and 4.4 for the dwarfs and the spirals, respectively. Note that there are no error-bars for  $\bar{\Sigma}_{\text{SFR}}$  in these plots since the standard deviations of SFR and  $R_{25}$  are not given by Leroy et al. (2008). The dashed grey line in the plots show the best fitted power-law relationship with a fixed slope of  $-1.54$  for the data of Westfall et al. (2014). This line has been taken directly from figure 3 in Westfall et al. (2014) to compare their result to ours, i.e. it has *not* been fitted to our data!

We see in figure 4.3 and 4.4 that there is no apparent anti-correlation between  $\bar{\Sigma}_{\text{SFR}}$  and any of the other quantities considered in these plots. However, for the spirals there is a *hint* of an anti-correlation between  $\bar{\Sigma}_{\text{SFR}}$  and the median of  $Q_3$ . The dashed green line shows our linear least-squares fit to the data points. It has a slope of  $-1.73$ , which is relatively close to  $-1.54$ . We also see that there is an offset between the green and the grey line. Moreover, for the dwarfs there is a *hint* of an anti-correlation between  $\bar{\Sigma}_{\text{SFR}}$  and the median of  $Q_3$ ; at least if one ignores the lowermost point in this plot. This point corresponds to the galaxy IC 2574, which is a relatively large dwarf galaxy with very

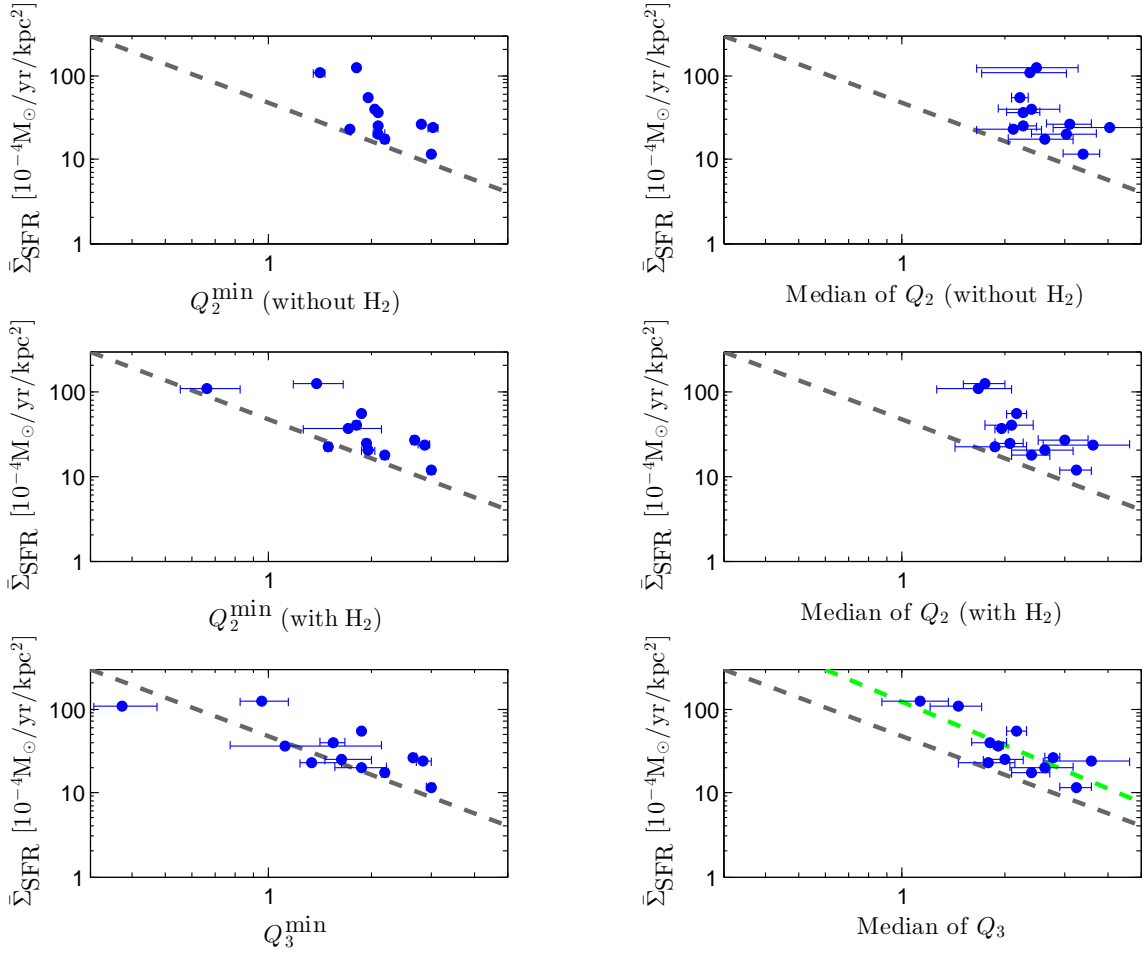


Figure 4.4:  $\bar{\Sigma}_{\text{SFR}}$  as a function of  $Q_N^{\text{min}}$  and the median of  $Q_N$ , respectively, for the three standard cases for the spirals.

low values of  $\Sigma_{\text{SFR}}$  over the entire optical disc. As a comparison, IC 2574 has an optical radius of 7.5 kpc and central values of  $\Sigma_{\text{SFR}}$  of about  $10^{-3} \text{ M}_{\odot}/\text{yr}/\text{kpc}^2$ , while the dwarf galaxy NGC 4214 has an optical radius of 2.9 kpc and central values of  $\Sigma_{\text{SFR}}$  of about  $10^{-1} \text{ M}_{\odot}/\text{yr}/\text{kpc}^2$ .

Without the point corresponding to IC 2574 we can *believe* that there exists an anti-correlation between  $\bar{\Sigma}_{\text{SFR}}$  and the median of  $Q_3$  for the dwarfs, but if there is such a relation it is much too faint in our data to justify a linear least-squares fit. However, we can tell by inspection of the bottom-right plots in figure 4.3 and 4.4 that there seems to be an offset between the data for the dwarfs and the data for the spirals.

Westfall et al. (2014) also seek a linear relationship between  $\bar{\Sigma}_{\text{SFR}}/\bar{\Sigma}_{\text{g}}$  and  $Q_2^{\text{min}}$ , as predicted by Li et al. (2006), where  $\bar{\Sigma}_{\text{g}}$  is the average value of  $\Sigma_{\text{g}}$  over the optical disc. They found a weak linear relationship with a slope of  $-1.0$ . Since  $\bar{\Sigma}_{\text{SFR}}/\bar{\Sigma}_{\text{g}}$  is a rather peculiar quantity, we decided to instead seek a relationship between  $\text{SFR}/M_{\text{g}}$  and  $Q_N^{\text{min}}$  or the median of  $Q_N$ , where  $M_{\text{g}}$  is the total gas mass of the galaxy. We obtained values of  $M_{\text{HI}}$  and  $M_{\text{H}_2}$  for the spirals from the electronic version of table 4 in Leroy et al. (2008), which include the mass of the helium. Unfortunately, there was not enough data for the dwarfs, so this analysis was only performed for the spirals. The result is shown in figure 4.5 and we see that there does not seem to be a correlation in any of these plots.

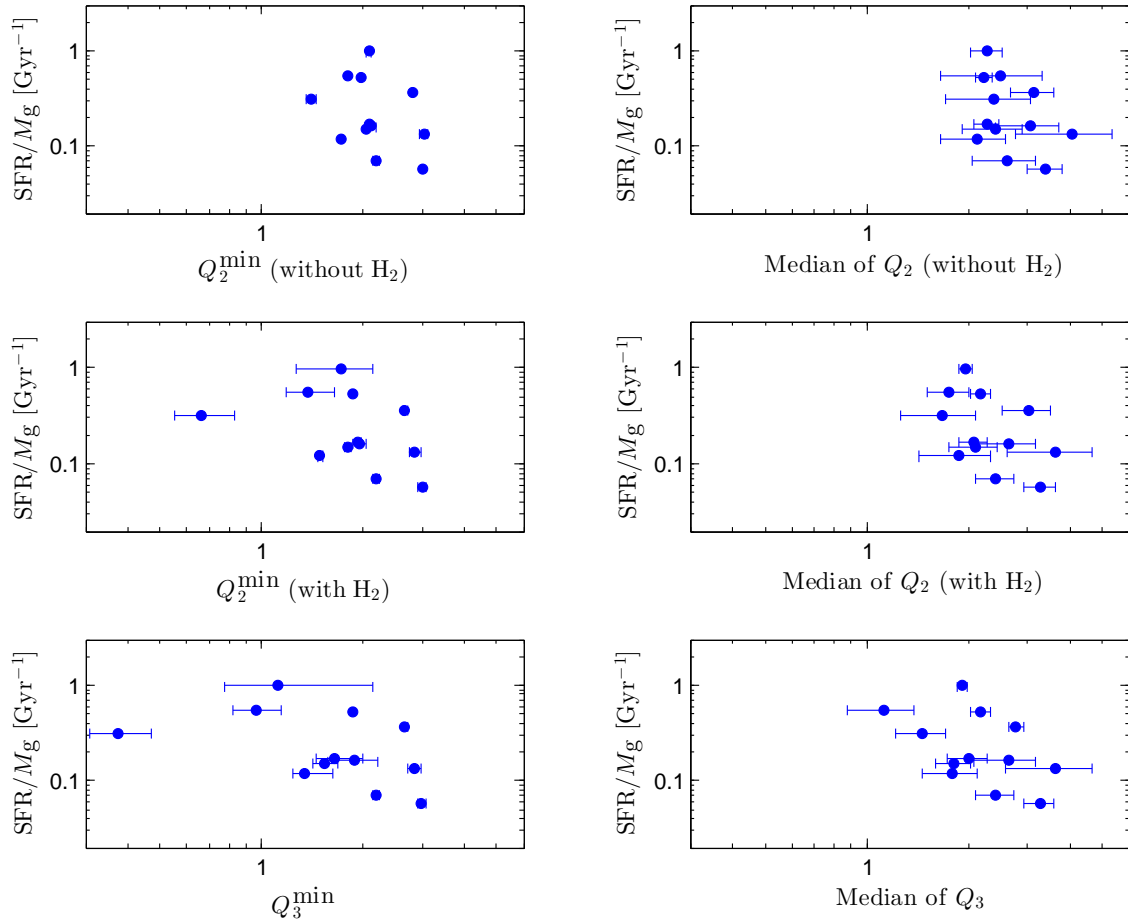


Figure 4.5:  $SFR/M_g$  as a function of  $Q_N^{\min}$  and the median of  $Q_N$ , respectively, for the three standard cases for the spirals.

# Chapter 5

## How reliable is our stability analysis?

In the stability analysis described in chapter 3 we have made use of several simplifying assumptions and approximations, and we will now investigate how reliable our analysis is.

### 5.1 The short-wavelength approximation

Let us first discuss the short-wavelength approximation. As we mentioned in section 2.2 the Toomre (1964) stability criterion is derived under the assumption that the radial wavelength  $\lambda$  of the perturbation is much smaller than the radius  $R$ . In fact, all  $Q$  stability parameters are based on this assumption, and we must therefore make sure that it holds in our analysis. The condition which must be satisfied may be written as  $|kR| \gg 1$ , where  $|k| = 2\pi/\lambda$  is the radial wavenumber of the perturbation. Note that although  $|kR|$  is formally required to be much greater than one, the short-wavelength approximation often performs well even with  $|kR|$  as small as unity. (Binney & Tremain 2008, p. 486)

Since Toomre-like stability criteria are on the form  $Q > 1$ , the  $Q$  parameter is always calculated for the radial wavenumber  $k_{\max}$  which minimizes  $Q$ , i.e. maximizes  $1/Q$ . By defining  $Q$  in this way one ensures that if  $Q > 1$  then the disc is stable against perturbations with *arbitrary*, albeit small, radial wavelengths. In deriving  $Q_N$  Romeo & Falstad (2013) approximate  $k_{\max}$  as  $k_{\max} \sim \kappa/\sigma_m$ , where  $m$  as before denotes the component with the smallest value of  $TQ$ . We therefore have that  $k_{\max}R \sim \kappa R/\sigma_m$ .

In figure 5.1 we show the value of this quantity as a function of galactocentric distance for the dwarfs and the spirals, respectively, for our three standard  $Q_N$  parameters. We see that in all six plots  $k_{\max}R \geq 1$  at all values of  $R/R_{25}$  except for very small ones. This means that the short-wavelength approximation is valid in our analysis, except near the galactic centers where the computed  $Q_N$ -values are uncertain anyway for reasons which are explained below. The percentage of data points with  $k_{\max}R < 1$  in the six plots is shown in table 5.2.

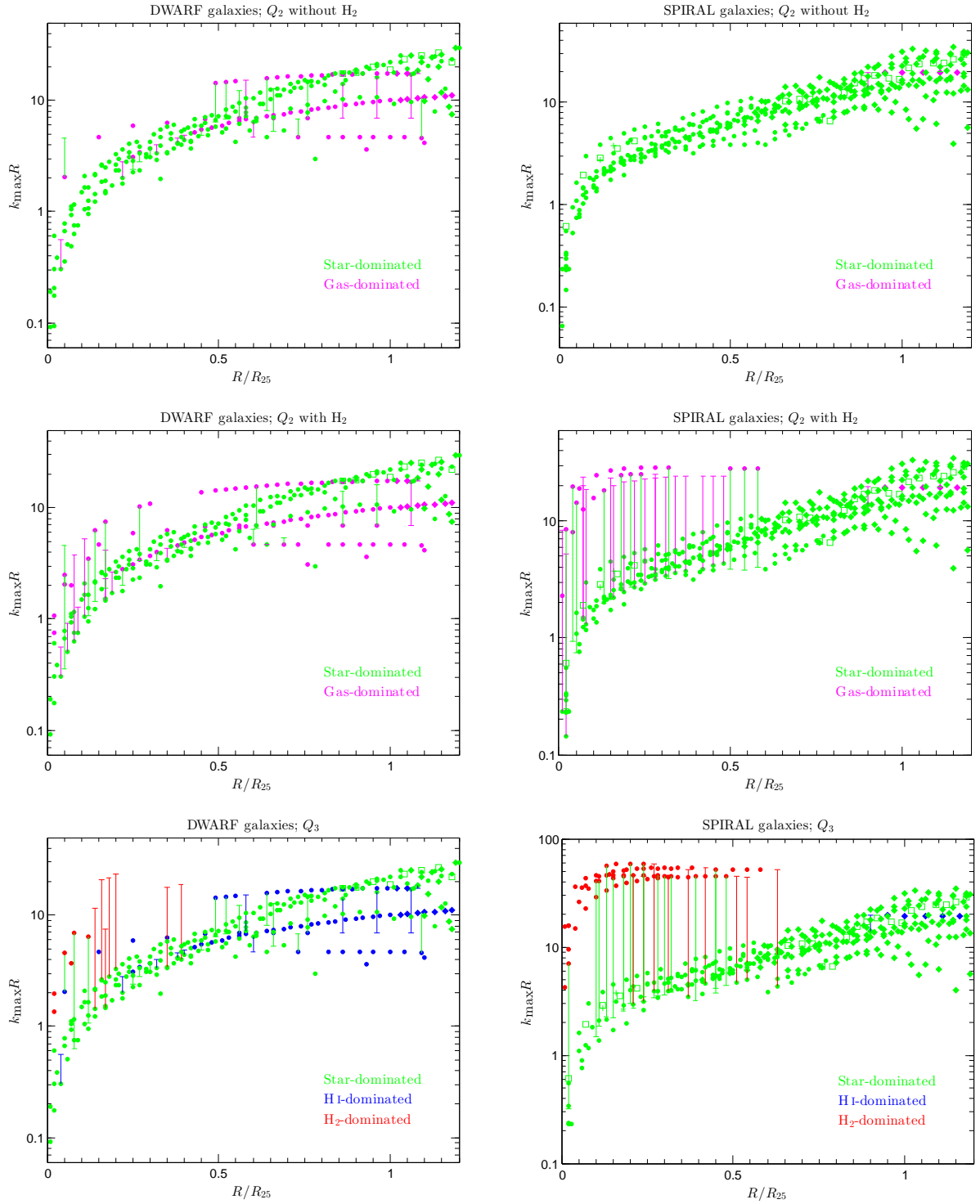


Figure 5.1: Plots of  $k_{\max}R$ , approximated as  $k_{\max}R \sim \kappa R/\sigma_m$ , for the dwarfs (left) and spirals (right).

Table 5.1: The percentage of data points with  $k_{\max}R < 1$  in the six plots in figure 5.1.

	$Q_2$ without $H_2$	$Q_2$ with $H_2$	$Q_3$
Dwarfs	7%	6%	5%
Spirals	5%	3%	2%

## 5.2 Velocity dispersions

Let us now discuss the velocity dispersion of stars  $\sigma_*$ . We computed  $\sigma_*$  with the help of equation B3 in Leroy et al. (2008), which is shown in section 3.1.1 in this thesis and is repeated below.

$$\sigma_{*,z} = \sqrt{\frac{2\pi Gl_*}{7.3} \Sigma_*^{0.5}} \quad (5.1)$$

Since Leroy et al. (2008) assume that  $l_*/h_* = 7.3 (\pm 2.2)$ , equation (5.1) gives the following expression for the exponential stellar scale height  $h_*$ :

$$h_* = \frac{\sigma_{*,z}^2}{2\pi G \Sigma_*} \quad (5.2)$$

However, as Hoffmann & Romeo (2012) point out,  $h_*$  depends on the *total* surface density  $\Sigma_{\text{tot}} = \Sigma_* + \Sigma_g$ , rather than merely  $\Sigma_*$ . This means that  $\sigma_{*,z}$  is actually given by

$$\sigma_{*,z} = \sqrt{\frac{2\pi Gl_*}{7.3} \Sigma_{\text{tot}}^{0.5}} \quad (5.3)$$

The relative error of equation (5.1) is

$$\left( \frac{\sigma_{*,z}^2}{2\pi G \Sigma_*} - \frac{\sigma_{*,z}^2}{2\pi G \Sigma_{\text{tot}}} \right) \bigg/ \frac{\sigma_{*,z}^2}{2\pi G \Sigma_{\text{tot}}} = \frac{\Sigma_g}{\Sigma_*}. \quad (5.4)$$

For the spiral galaxies  $\Sigma_*$  tends to be much larger than  $\Sigma_g$  at all radii, except at  $R \gtrsim R_{25}$ . This means that equation (5.1) is only a good approximation of  $\sigma_{*,z}$  for the spirals at  $R \lesssim R_{25}$ . However, for the dwarf galaxies  $\Sigma_*$  is only significantly larger than  $\Sigma_g$  at much smaller radii, and  $\Sigma_* < \Sigma_g$  at *all* radii for the two smallest dwarfs DDO 154 and Ho I! In other words: equation (5.1) is a very poor approximation of  $\sigma_{*,z}$  for the dwarfs, except at relatively small radii in the largest of these galaxies.

This has consequences; one of which is illustrated in figure 5.2, which shows  $\sigma_{H\text{I}}/\sigma_*$  as a function of galactocentric distance for the dwarfs and the spirals, respectively. The left plots show the result of computing  $\sigma_*$  from (5.1) and the right ones show the same for equation (5.3). We see that the black points in these plots form bands which rise almost linearly with  $R/R_{25}$ . This is not very surprising considering that  $\Sigma_*$  decreases exponentially with radius, as we mentioned in section 3.1.1.

What should be more surprising is that so many of the data points in the upper-left plot lay in the green regions, which are marked as ‘unphysical’. In fact, all of the blue

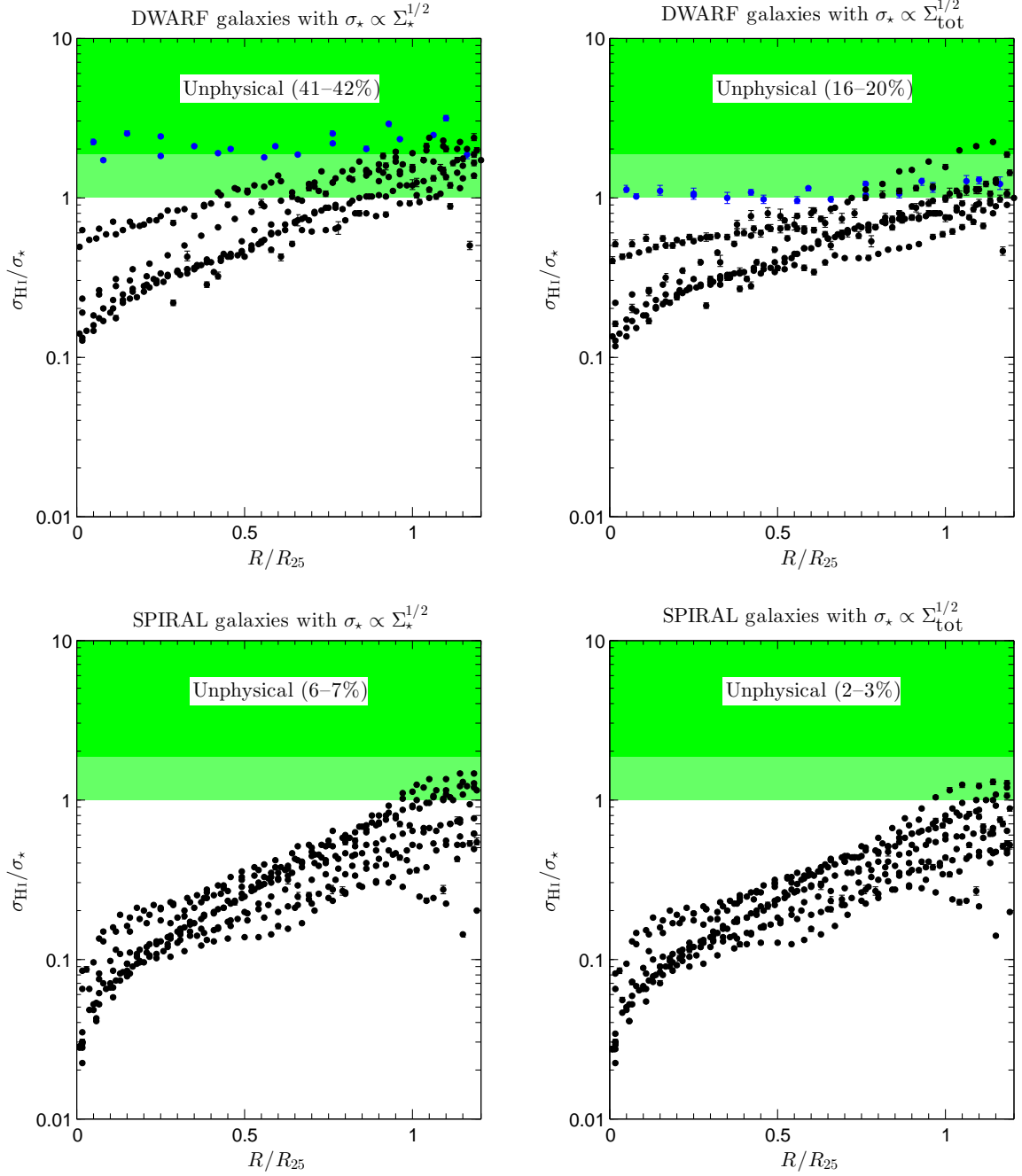


Figure 5.2: Plots of  $\sigma_{\text{HI}}/\sigma_*$  for the dwarfs (upper) and the spirals (lower). In the left plots  $\sigma_*$  has been computed using equation (5.1), which gives  $\sigma_* \propto \Sigma_*^{1/2}$ , and in the right plots  $\sigma_*$  has been computed using equation (5.3), which gives  $\sigma_* \propto \Sigma_{\text{tot}}^{1/2}$ . Note that *all* data points have been used for these plots, including those with vanishing values of both  $\Sigma_{\text{H1}}$  and  $\Sigma_{\text{H2}}$ .

points, which belong to DDO 154 and Ho I, are in these regions. The light-green region shows where  $\sigma_\star < \sigma_{\text{HI}}$  and the darker green region shows where  $\sigma_\star < \sigma_{\text{H}_2}$ . We should not find any points at all in either of these regions! The reason for this is that stars are formed from  $\text{H}_2$ , and *newly formed* stars may therefore have velocity dispersions as low as that of  $\text{H}_2$ . However, unlike gas stars cannot ‘cool down’ through dissipation. In fact, the velocity dispersion of disc stars instead increases with time (‘disc heating’) due to their interaction with spiral waves and encounters with giant molecular clouds. (Romeo 1990). Since the stars studied by Leroy et al. (2008) belong to the so-called ‘old stellar disc’, which consists of elderly stars such as our Sun, they should therefore have  $\sigma_\star \gg \sigma_{\text{HI}}$ , and they *must* at least have  $\sigma_\star > \sigma_{\text{H}_2}$ .

Despite this we find that 41–42% of the data points<sup>1</sup> for the dwarfs have  $\sigma_\star < \sigma_{\text{HI}}$  for  $\sigma_\star \propto \Sigma_\star^{1/2}$ . Also, 11% have  $\sigma_\star < \sigma_{\text{H}_2}$ , which is physically impossible! However, we see that all points at small galactocentric distances have  $\sigma_\star > \sigma_{\text{HI}}$ , except for those belonging to DDO 154 and Ho I. Moreover, for the spirals only 6–7% of the points have  $\sigma_\star < \sigma_{\text{HI}}$  for  $\sigma_\star \propto \Sigma_\star^{1/2}$ , and these points are all located at  $R \gtrsim R_{25}$ . These observations are in full agreement with our analysis of the accuracy of equation (5.1) for the dwarfs and the spirals, respectively.

We also see that for both subsamples there are only about half as many unphysical points for  $\sigma_\star \propto \Sigma_{\text{tot}}^{1/2}$  as for  $\sigma_\star \propto \Sigma_\star^{1/2}$ . This shows how important it is to take the total surface density in the expression for  $\sigma_\star$  in general, and for dwarf galaxies in particular. But even then there are many unphysical points, which indicates the need of direct measurements of  $\sigma_\star$ .

Another interesting observation is that for the spirals there are points with  $\sigma_{\text{HI}}/\sigma_\star$  on the order of 0.01 at small galactocentric distances. Such high velocity dispersions of stars are never observed. For instance, the lowermost point in the lower-left plot in figure 5.2 has  $\sigma_\star = 492 \text{ km/s}$ , which seems too high to be true. Unfortunately, it is impossible to say precisely how large the value of  $\sigma_\star$  can be since this depends on the galaxy. However, in the Solar neighborhood the radial velocity dispersion of old stars is  $38 \pm 2 \text{ km/s}$  and even for the bulge stars in the Milky Way the root mean square (RMS) velocity is only about  $150 \text{ km/s}$  (Binney & Tremain 2008, pp. 15, 18), which implies an RMS radial velocity dispersion of about  $150/\sqrt{3} \text{ km/s} \sim 100 \text{ km/s}$  (assuming that the stellar velocity dispersion is isotropic). In general we expect to find  $\sigma_\star \lesssim 100 \text{ km/s}$  for disc stars and  $100 \text{ km/s} \lesssim \sigma_\star \lesssim 200 \text{ km/s}$  for stars in the bulge or halo. The large stellar velocity dispersions at small galactocentric distances seen in figure 5.2 are therefore an indication that either the equation of Leroy et al. (2008) for  $\sigma_\star$  is very inaccurate at small radii in the spirals, or the values of  $\Sigma_\star$  deduced from observational data are too high near the centers of these galaxies. The latter would give too large values of  $\sigma_\star$ , and it could result from contamination of  $\Sigma_\star$  from halo and/or bulge stars in the line of sight.

Regardless of the cause, the suspiciously large values of  $\sigma_\star$  for the spirals at small radii are another reason for why direct observations of this quantity are required for a stability analysis. Moreover, it should be mentioned in this context that Leroy et al. (2008) assume that  $(\sigma_z/\sigma_R)_\star = 0.6$  to calculate  $\sigma_\star \equiv \sigma_{\star,R}$  from equation (5.1), but the ratio between  $\sigma_{\star,z}$  and  $\sigma_{\star,R}$  is not constant. It is well-known that the velocity dispersion of stars becomes

---

<sup>1</sup>The percentages depend on the method by which one computes them. See appendix B for a short discussion on this subject.

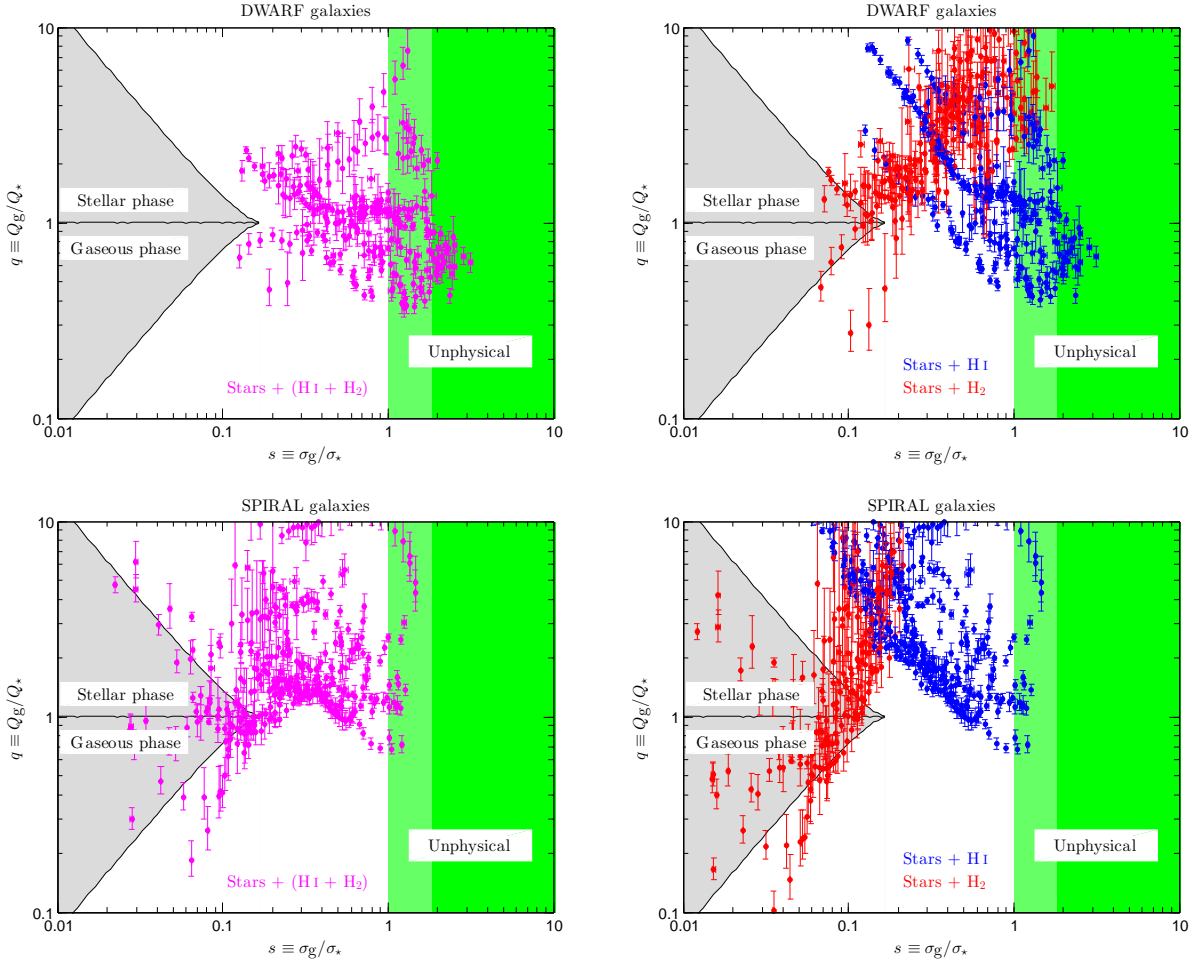


Figure 5.3: These plots show how the dwarfs (upper) and spirals (lower) populate the  $(s, q)$  plane for the three cases described in the main text.

isotropic towards the center of a galaxy, i.e.  $(\sigma_z/\sigma_R)_* \rightarrow 1$  when  $R \rightarrow 0$ , and this ratio also depends on the Hubble-type in an unknown way. This is yet another reason for why *direct measurements* of  $\sigma_*$  are needed!

Before we leave the subject of  $\sigma_*$ , let us discuss figure 5.3. These plots show how the dwarfs and the spirals populate the  $(s, q)$  plane of Romeo & Wiegert (2011) for the three cases: (1) stars + (H I + H<sub>2</sub>), (2) stars + H I, and (3) stars + H<sub>2</sub>. The parameters  $s$  and  $q$  are defined as  $s \equiv \sigma_g/\sigma_*$  and  $q \equiv Q_g/Q_*$ . In case 1 we treat all the gas as a single component with  $\sigma_g = \sigma_{\text{H I}}$ , and in case 2 and 3 we completely ignore H<sub>2</sub> and H I, respectively.

As in figure 5.2, we see in figure 5.3 that there are a lot of data points with unphysically low values of  $\sigma_*$ . Be aware though that the light-green region has different meanings for the three cases. For case 1 and 2 it shows where  $\sigma_* < \sigma_{\text{H I}}$ , but for case 3 it instead shows where  $\sigma_* < \sigma_{\text{H}_2}$ . The darker green region shows where  $\sigma_* < \sigma_{\text{H}_2}$  for case 1 and 2, while it has no specific meaning for case 3.

Figure 5.3 also shows the so-called ‘two-phase region’, which is colored grey in these

plots. Inside this region the dispersion relation  $\omega^2(k)$ , where  $\omega$  is the angular frequency, has two local minima; one is due to the stars and the other one is due to the gas. Outside the two-phase region  $\omega^2(k)$  has only a single (global) minimum. The galactic disc is gravitationally unstable against axisymmetric, or tightly wound, density waves with radial wavenumber  $k$  if  $\omega^2(k) < 0$ . In the upper part of the two-phase region (stellar phase) the stellar minimum is beneath the gaseous one, which means that the stars determine when the disc is no longer stable for all permissible values of  $k$ . In the lower part of the same region (gaseous phase) the opposite is true, while outside the grey area the stellar and gaseous minima coincide.

We see in figure 5.3 that for the dwarfs none of the data points are inside the two-phase region in case 1 and 2, while in case 3 only a few points are inside it (4–8%). For the spirals there are plenty of points inside the grey area in case 1 (12–17%) and even more in case 3 (45–59%), but none in case 2. This tells us that H I is dynamically coupled to stars for both subsamples, while H<sub>2</sub> tends not to be, and that the share of H<sub>2</sub> which is decoupled from stars is much higher in the spirals than in the dwarfs.

Next, let us investigate the assumptions made for the velocity dispersions of H I, H<sub>2</sub> and helium (He). We adopted the fixed value  $\sigma_{\text{HI}} = 11$  km/s given by Leroy et al. (2008). They claim that  $\sigma_{\text{HI}} = 11 \pm 3$  km/s is a good description of  $\sigma_{\text{HI}}$  in the outer parts of the optical discs ( $0.5$ – $1.0R_{25}$ ) of THINGS galaxies with inclinations  $i \lesssim 60^\circ$ . However, the median of  $\sigma_{\text{HI}}$  is different for each galaxy, and one may wonder how selecting a single value to represent  $\sigma_{\text{HI}}$  for all the galaxies has affected our results.

Leroy et al. (2008) do not provide numerical values of the median of  $\sigma_{\text{HI}}$  and the  $1\sigma$ -scatter of this quantity for individual THINGS galaxies (they merely plot them), so we will use the results of Ianjamasimanana et al. (2012) instead. In their paper Ianjamasimanana et al. (2012) analyze the shapes of the H I velocity profiles of the THINGS galaxies. They find that the neutral atomic hydrogen in these galaxies actually consists of two components: a cold component with velocity dispersions in the range  $\sim 3.4$  to  $\sim 8.6$  km/s and a warm component in the range  $\sim 10.1$  to  $\sim 24.3$  km/s. Unfortunately, we cannot treat H I as two distinct components since we do not know the surface densities of the components. However, in table 1 in their paper Ianjamasimanana et al. (2012) also provide values of  $\sigma_{\text{HI}}$  computed from single Gaussian fits to their data, together with the corresponding standard deviations. These fits treat all the H I as a single component and the values relevant to our study are shown in table 5.2 in this thesis.

To estimate the impact on our stability analysis from changing to these values of  $\sigma_{\text{HI}}$  we used them to compute  $Q_3$  for the dwarfs and the spirals, respectively. The result is shown in figure 5.4, and by comparing these two plots to the bottom two plots in figure 3.1 we see that assigning different values of  $\sigma_{\text{HI}}$  to the individual galaxies has no qualitative effect on the scatter plots of  $Q_3$ . For the spirals it has essentially no impact at all, which is easy to understand considering that only a few  $Q_3$ -points are H I-dominated for these galaxies. For the dwarfs the effect is somewhat larger, but still very small. This is also understandable in light of the fact that the values of  $\sigma_{\text{HI}}$  in table 5.2 are relatively close to 11 km/s for all the dwarfs.

From this perspective it therefore seems acceptable to use  $\sigma_{\text{HI}} = 11$  km/s for all the galaxies in our stability analysis. However, there is a caveat to using a fixed value of  $\sigma_{\text{HI}}$ . It is well-known that the velocity dispersion of gas increases towards the center of a

Table 5.2: Values of  $\sigma_{\text{HI}}$  for individual dwarfs and spirals taken from table 1 in Ianjamasimanana et al. (2012).

	Dwarfs	$\sigma_{\text{HI}}$ [km/s]		Spirals	$\sigma_{\text{HI}}$ [km/s]
1	DDO 154	$9.7 \pm 0.1$	12	NGC 628	$9.0 \pm 0.2$
2	Ho I	$8.9 \pm 0.2$	13	NGC 3198	$13.1 \pm 0.3$
3	Ho II	$9.1 \pm 0.2$	14	NGC 3184	$11.3 \pm 0.3$
4	IC 2574	$10.1 \pm 0.2$	15	NGC 4736	$11.0 \pm 0.3$
5	NGC 4214	$8.8 \pm 0.1$	16	NGC 3351	$10.2 \pm 0.3$
6	NGC 2976	$11.9 \pm 0.3$	17	NGC 6946	$10.4 \pm 0.2$
7	(NGC 4449)	$13.8 \pm 0.2$	18	NGC 3627	$20.8 \pm 0.5$
8	(NGC 3077)	$12.6 \pm 0.3$	19	NGC 5194	$17.0 \pm 0.4$
9	NGC 7793	$10.6 \pm 0.2$	20	NGC 3521	$17.4 \pm 0.4$
10	NGC 2403	$11.1 \pm 0.3$	21	NGC 2841	$16.3 \pm 0.4$
11	NGC 925	$12.7 \pm 0.2$	22	NGC 5055	$14.0 \pm 0.4$
			23	NGC 7331	$19.5 \pm 0.4$

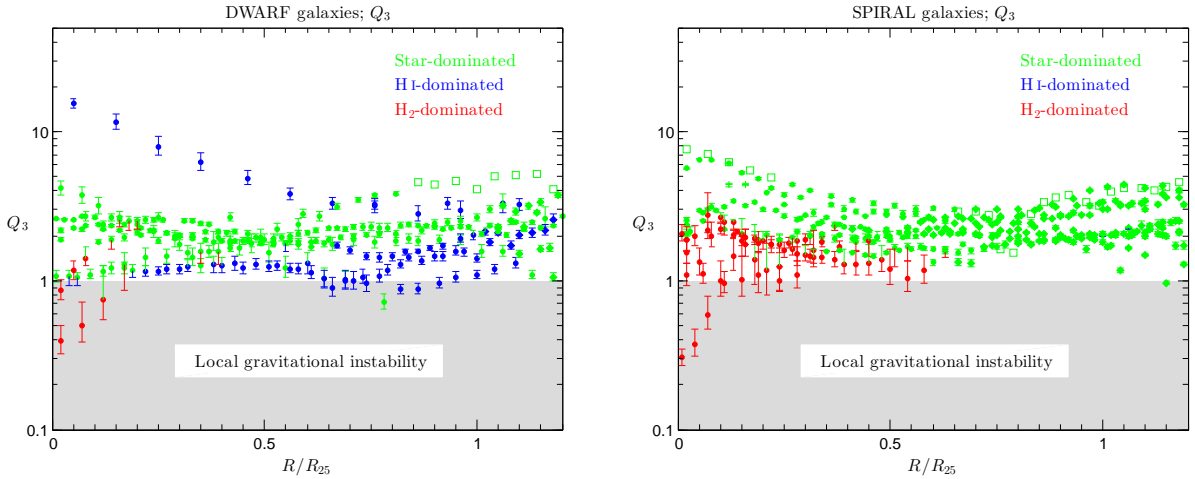


Figure 5.4: Scatter plots of  $Q_3$  for the dwarfs (left) and the spirals (right) computed using the values of  $\sigma_{\text{HI}}$  listed in table 5.2.

galaxy, and a constant value of  $\sigma_{\text{H I}}$  does not take this into consideration. The same can be said about the fixed value  $\sigma_{\text{H}_2} = 6 \text{ km/s}$  which we also adopted<sup>2</sup>. In order to obtain more accurate results at small radii we therefore need *radial profiles* of both  $\sigma_{\text{H I}}$  and  $\sigma_{\text{H}_2}$  based on *direct observations*!

Let us finally briefly comment on the velocity dispersion  $\sigma_{\text{He}}$  of helium. We mentioned in section 3.1.1 that Leroy et al. (2008) accounted for the helium by including a factor 1.36 in their tabulated values of  $\Sigma_{\text{H I}}$  and  $\Sigma_{\text{H}_2}$ . With this method one implicitly assigns the same value to the velocity dispersion of helium as that of the H I or H<sub>2</sub> which it has been associated with. In addition, one also implicitly assumes a fixed value of the ratio  $(\Sigma_{\text{H I}} + \Sigma_{\text{H}_2})/\Sigma_{\text{He}}$ . Unfortunately, we do not know the true values of either  $\sigma_{\text{He}}$  or  $\Sigma_{\text{He}}$  since there is no observational data on these quantities.

---

<sup>2</sup>Leroy et al. (2008) mention that this is the value of  $\sigma_g$  used by both Kennicutt (1989) and Martin & Kennicutt (2001).



# Chapter 6

## Conclusions

Below we point out the main steps of the analysis performed in this thesis and the conclusions drawn from the results.

1. We have analyzed the gravitational instability of 9 dwarf and 12 spiral galaxies from the THINGS sample, previously analyzed by Leroy et al. (2008), using the  $Q$  stability parameter for multicomponent and realistically thick galactic discs introduced by Romeo & Falstad (2013). Three distinct cases were investigated in which the galactic discs were modeled as: (a) two-component systems consisting of stars and H I, (b) two-component systems consisting of stars and gas (H I + H<sub>2</sub>), and (c) three-component systems consisting of stars, H I and H<sub>2</sub>. Of these cases the last one is the superior diagnostic for the spirals as well as for the dwarfs, provided that we can trust the estimated values of the surface density of H<sub>2</sub> ( $\Sigma_{\text{H}_2}$ ) for the latter galaxies. Following Leroy et al. (2008) we have estimated these values for the dwarfs from the star formation rate surface density ( $\Sigma_{\text{SFR}}$ ) using an empirical linear relation which is known to approximately hold for the spirals.
2. Scatter plots of the three-component (stars + H I + H<sub>2</sub>)  $Q$  stability parameter  $Q_3$  of Romeo & Falstad (2013) were computed for the dwarfs and the spirals. For both subsamples the  $Q_3$ -values mostly lay within relatively narrow bands just above the threshold for instability, i.e.  $Q_3 = 1$ . The component that gives the dominant contribution to disc instability was also computed for each data point. For both the dwarfs and the spirals there are star-dominated  $Q_3$ -points at all galactocentric distances ( $R/R_{25}$ ). Both subsamples also have H<sub>2</sub>-dominated points with  $Q_3 < 1$  at small  $R/R_{25}$ , but the nature and distribution of the gas-dominated points are otherwise different between the dwarfs and the spirals. The dwarfs have gas-dominated points at all galactocentric distances, with a slightly higher concentration for  $R/R_{25} \gtrsim 0.5$ , and all of these points are H I-dominated except for a few H<sub>2</sub>-dominated points at small  $R/R_{25}$ . For the spirals on the other hand nearly all gas-dominated points are H<sub>2</sub>-dominated with  $R/R_{25} \lesssim 0.6$ .
3. The median of  $Q_3$  is nearly independent of  $R/R_{25}$  with a value of about 2 for both the dwarfs and the spirals. Moreover, for both subsamples the majority of the  $Q_3$ -points are star-dominated at all galactocentric distances except at  $R/R_{25} \approx 0.95$

for the dwarfs and for  $R/R_{25} \lesssim 0.15$  in the spirals, where the points are instead gas-dominated.

4. Scatter plots of  $\Sigma_{\text{SFR}}$  as a function of galactocentric distance were computed for the dwarfs and the spirals. A previous analysis by Leroy et al. (2008) showed that the logarithm of the median of  $\Sigma_{\text{SFR}}$  is a nearly linear function of  $R/R_{25}$  for both subsamples. We have found that this result is not robust for the dwarfs. We suspect that the reason for this is that there are too few galaxies in the dwarf subsample of Leroy et al. (2008) and that these galaxies are not representative of the population of dwarf galaxies in the nearby Universe.
5. We have searched for a correlation between  $Q_N$  and the *effective* star formation rate surface density  $\bar{\Sigma}_{\text{SFR}}$ , defined as the ratio between the global star formation rate SFR and the area  $\pi R_{25}^2$  of the optical disc. We found a *hint* of such a relation between  $\bar{\Sigma}_{\text{SFR}}$  and the median of  $Q_3$  computed for each spiral individually, and also a somewhat weaker sign of the same for the dwarfs. Unfortunately, the dwarf and spiral subsamples of Leroy et al. (2008) which were used in this thesis are too small to either confirm or refute the existence of such correlations.
6. We have shown that the formula for the radial velocity dispersion of stars ( $\sigma_*$ ) used by Leroy et al. (2008) gives unphysically low values of this quantity for  $R \gtrsim R_{25}$  in the spirals and at all radii in the dwarfs, except for very small ones in the largest of the dwarf galaxies. As we mentioned, this expression for  $\sigma_*$  is in fact incorrect. We showed that an improved version of the formula only gives about half as many unphysically low values of  $\sigma_*$  for both subsamples. However, for the dwarfs the percentage of such points is still unacceptably high, and for the spirals there are also values of  $\sigma_*$  at small radii which are too high. This illustrates the need for *direct observations* of  $\sigma_*$ !
7. Even more importantly, following previous studies (for instance Kennicutt 1989, Martin & Kennicutt 2001 and Leroy et al. 2008) we have used fixed values of the velocity dispersions of H I ( $\sigma_{\text{H I}}$ ) and H<sub>2</sub> ( $\sigma_{\text{H}_2}$ ) since there are no reliable measurements of the radial profiles of these quantities throughout the galactic discs. However, we know that the velocity dispersion of gas increases towards the galactic center, which has never been taken into account in any stability analysis. We pointed out that the fixed value of  $\sigma_{\text{H}_2}$  might be the reason for why there are H<sub>2</sub>-dominated  $Q_3$ -points with values below 1 at small radii in both the dwarfs and the spirals. If we had used the correct values of  $\sigma_{\text{H}_2}$  then these points might have been above the threshold for instability. For an accurate stability analysis one should therefore use radial profiles of primarily  $\sigma_{\text{H}_2}$ , but also  $\sigma_{\text{H I}}$ , based on *direct measurements*!

# Appendix A

## Radial profiles of individual galaxies

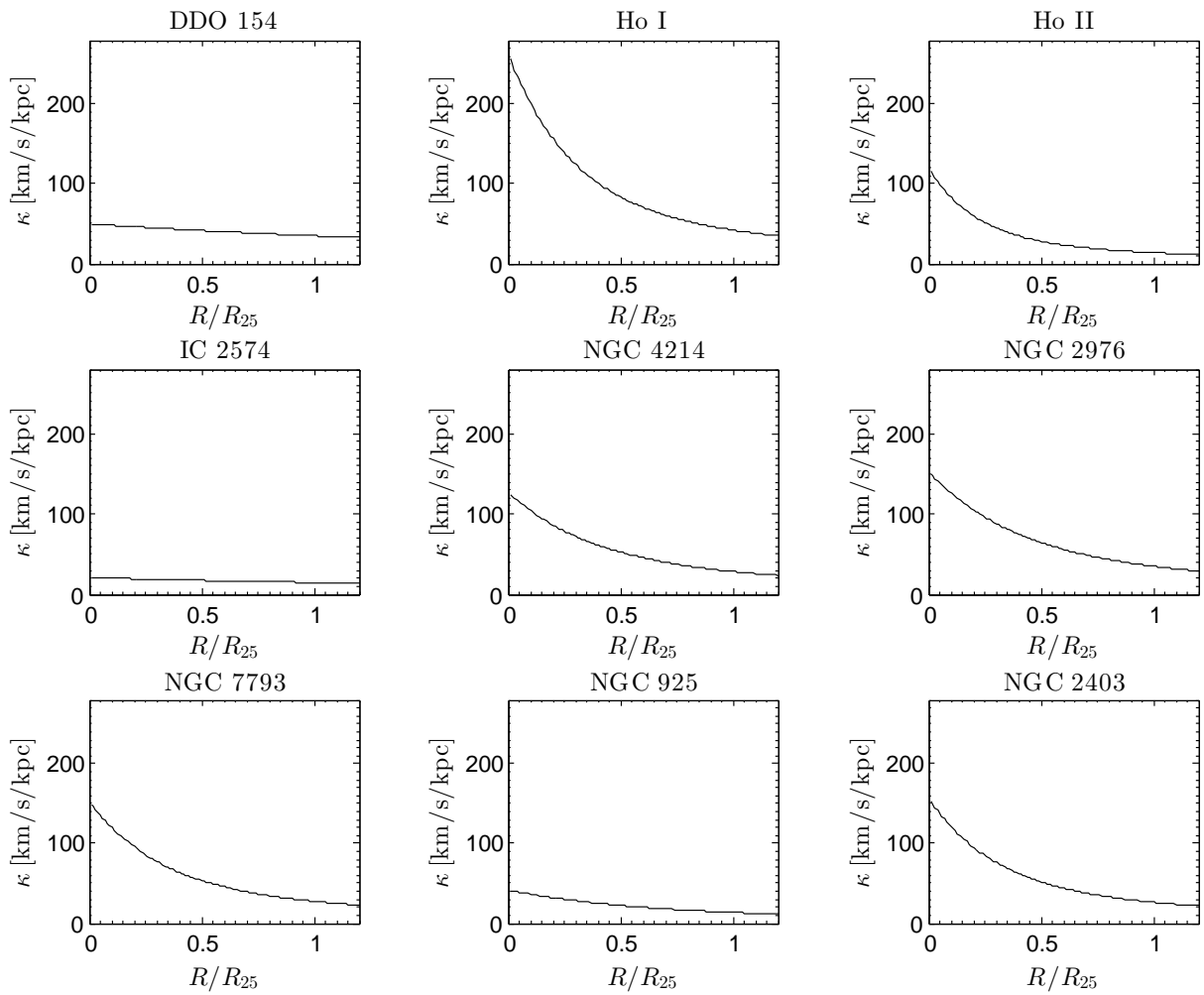


Figure A.1: The epicyclic angular frequency  $\kappa$  as a function of galactocentric distance  $R/R_{25}$  for the DWARF galaxies.

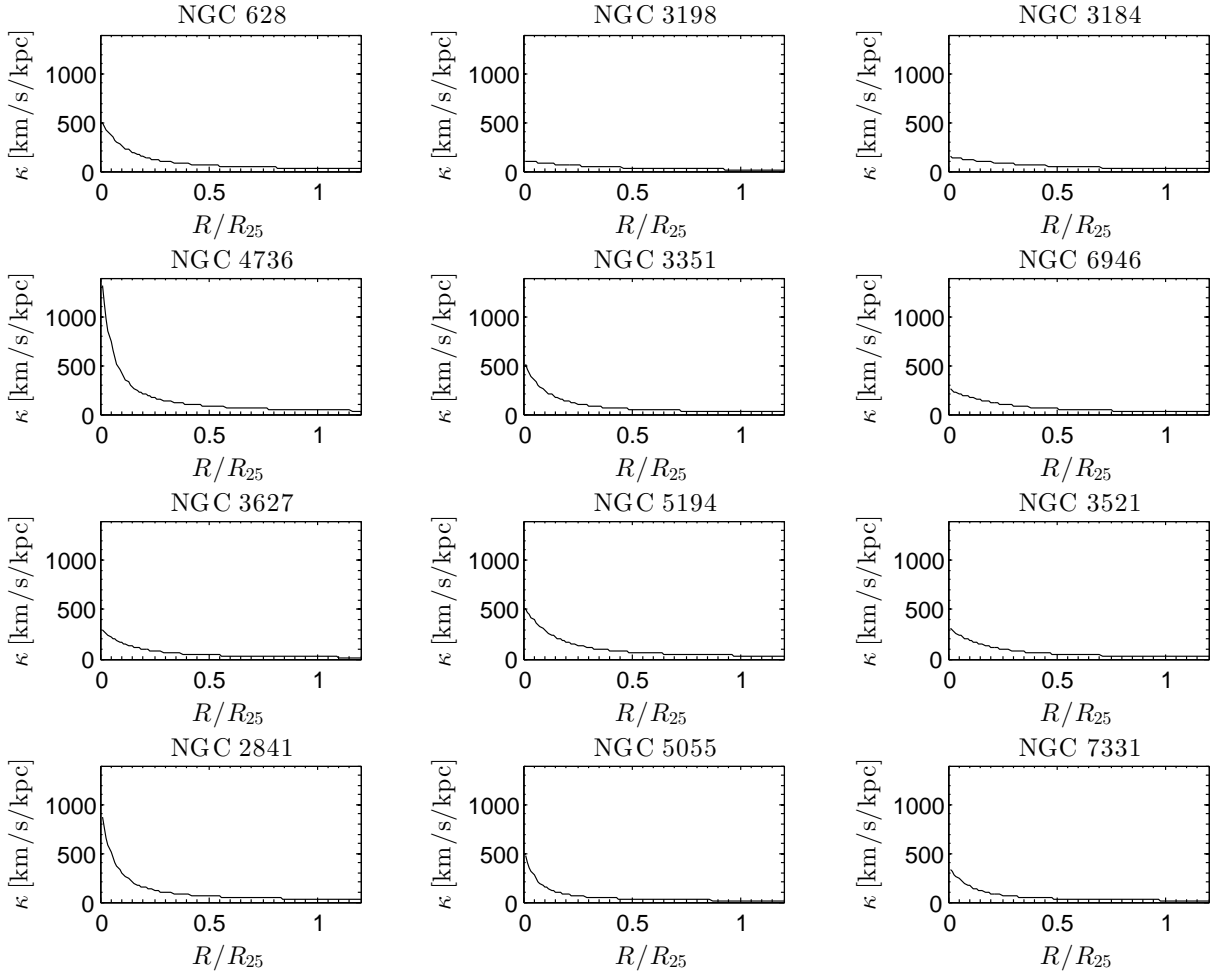


Figure A.2: The epicyclic angular frequency  $\kappa$  as a function of galactocentric distance  $R/R_{25}$  for the SPIRAL galaxies.

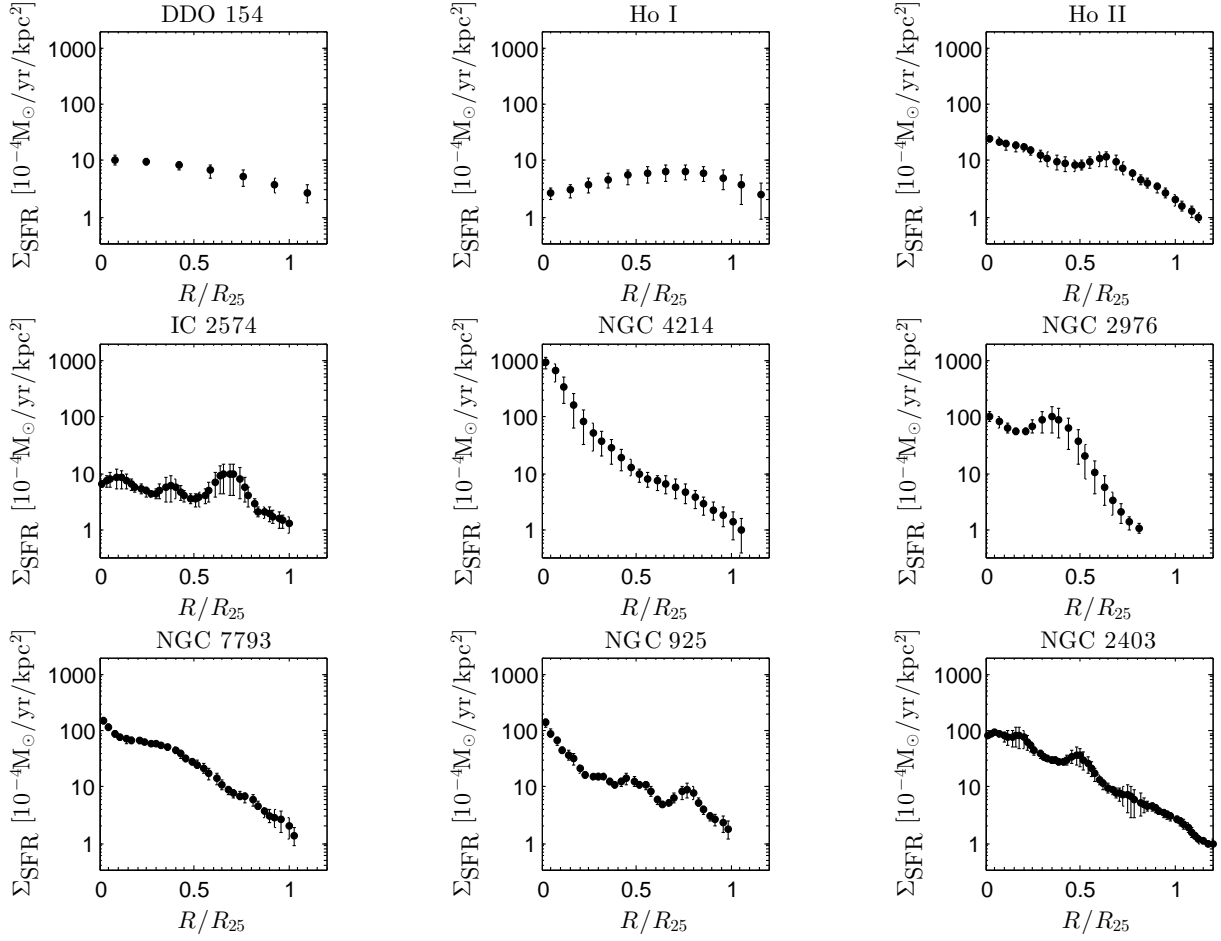


Figure A.3: The star formation rate surface density  $\Sigma_{\text{SFR}}$  as a function of galactocentric distance  $R/R_{25}$  for the DWARF galaxies.

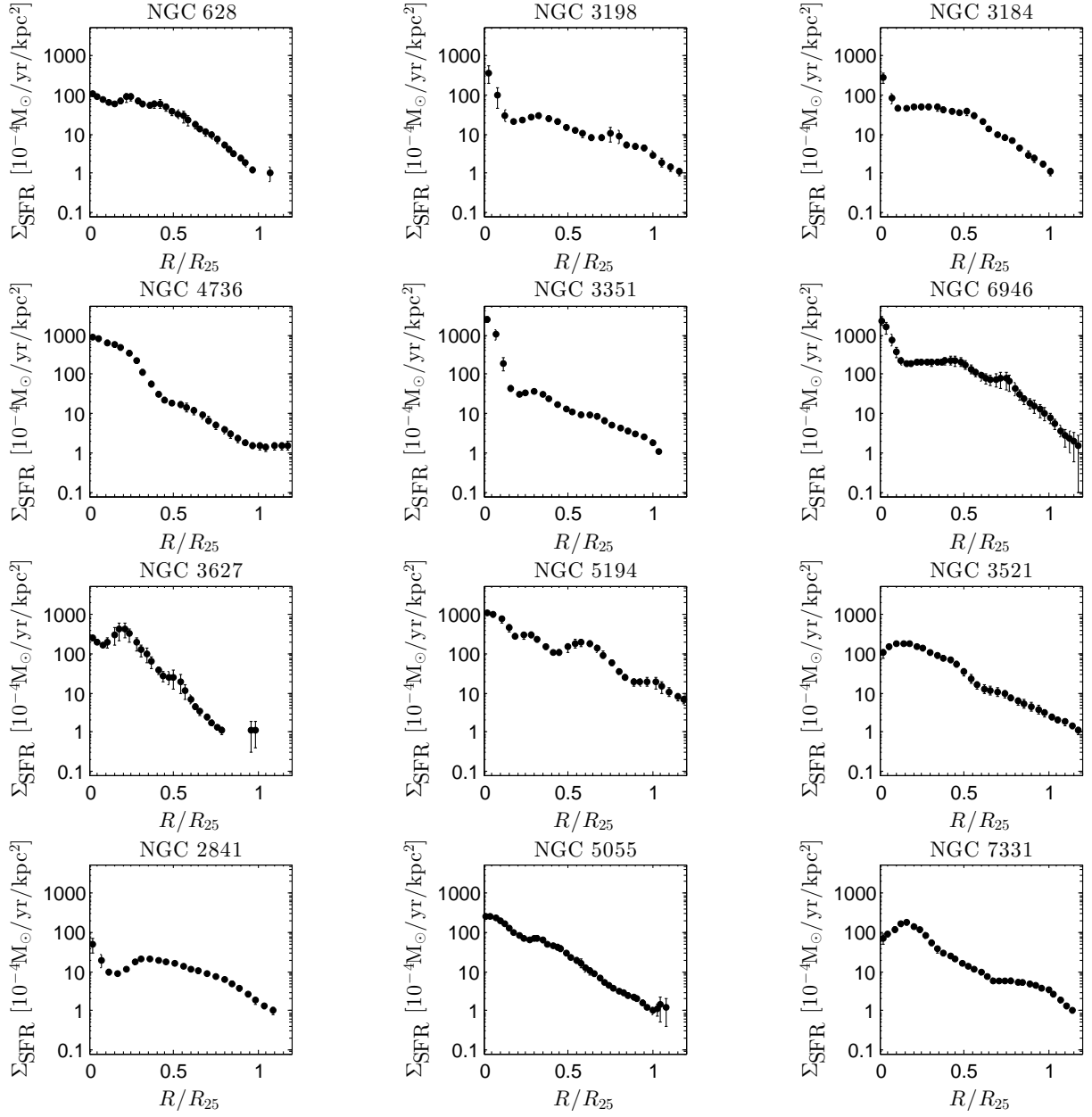


Figure A.4: The star formation rate surface density  $\Sigma_{\text{SFR}}$  as a function of galactocentric distance  $R/R_{25}$  for the SPIRAL galaxies.

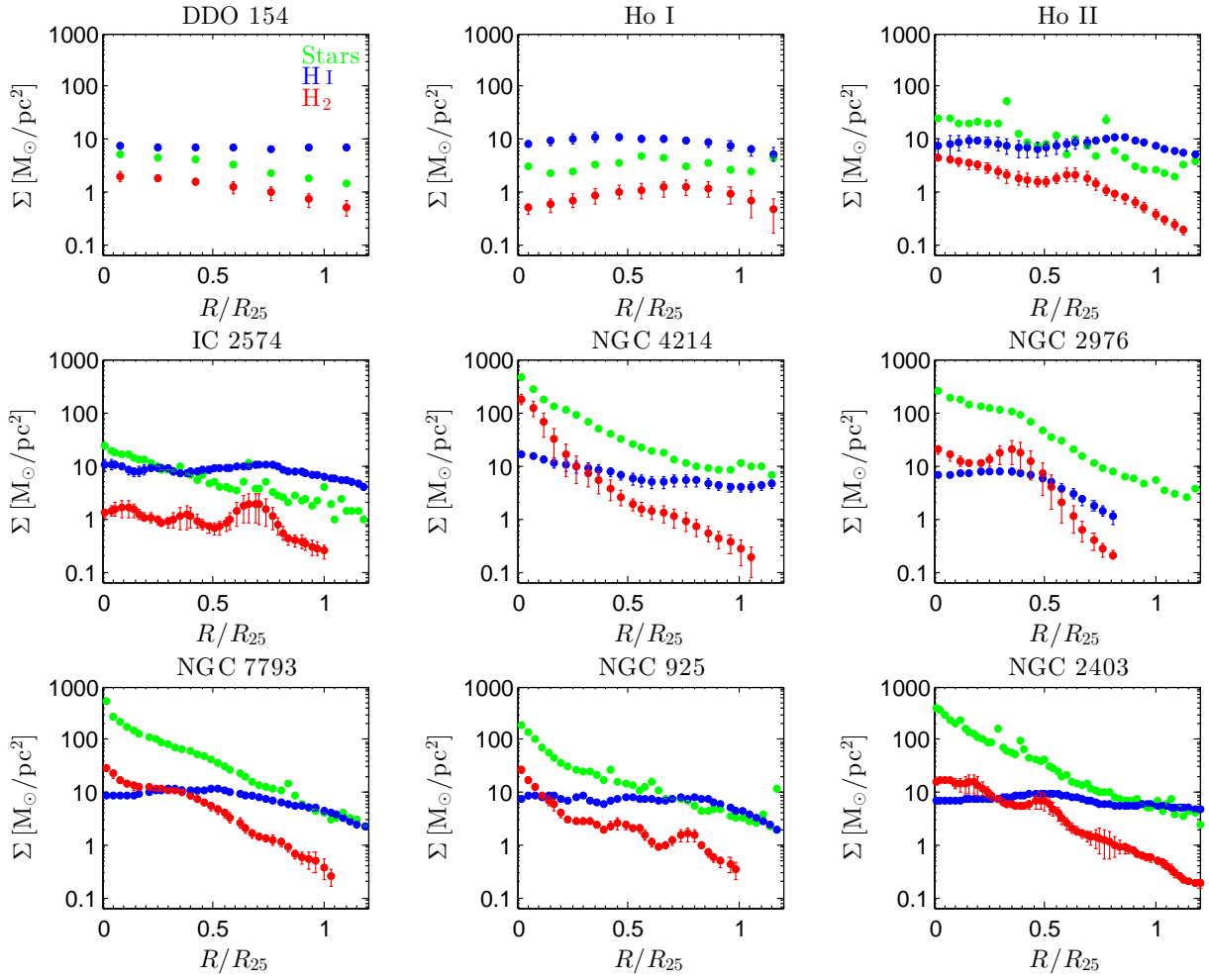


Figure A.5: The surface density  $\Sigma$  of stars, H I and H<sub>2</sub>, respectively, as a function of galactocentric distance  $R/R_{25}$  for the DWARF galaxies.

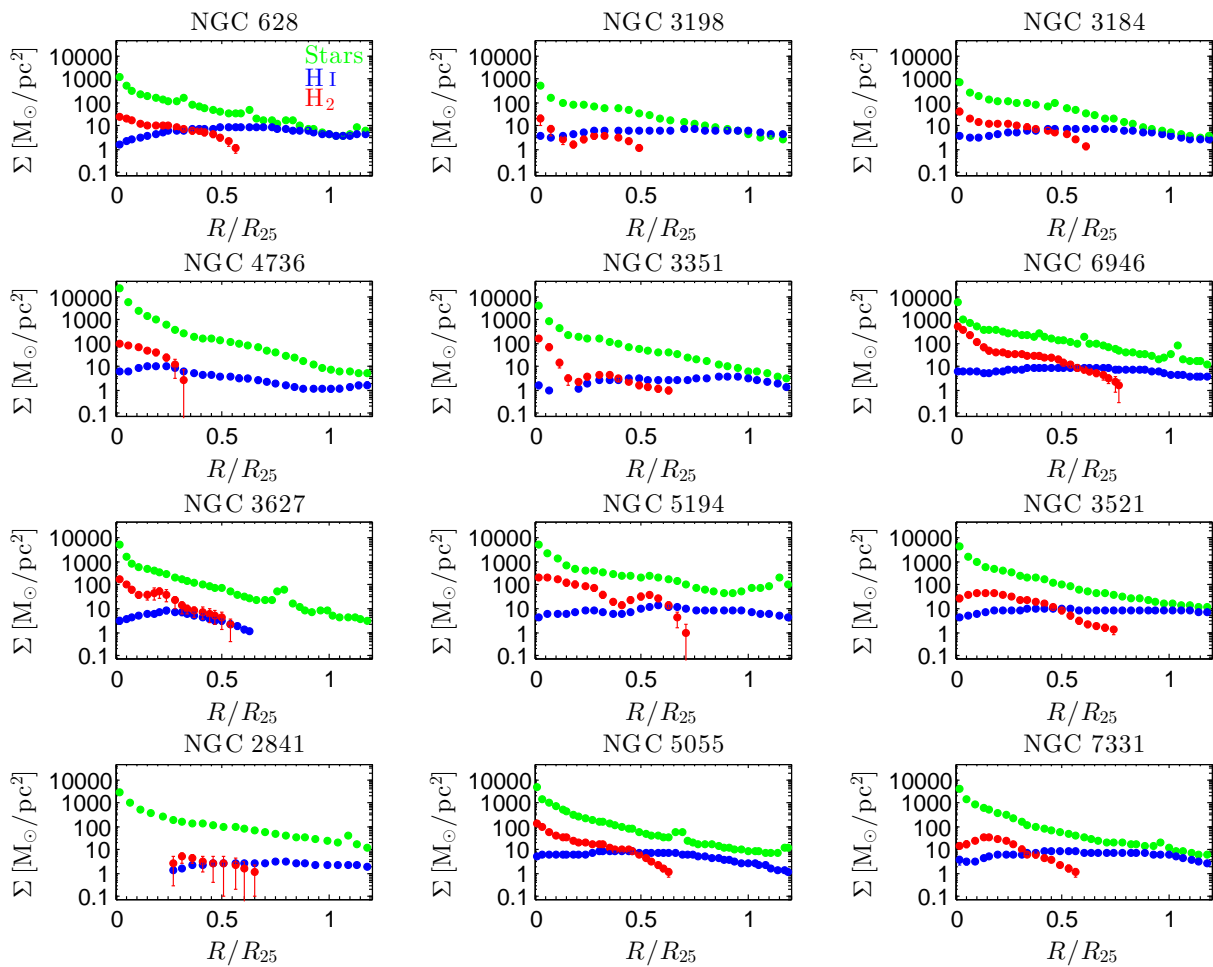


Figure A.6: The surface density  $\Sigma$  of stars, H I and H<sub>2</sub>, respectively, as a function of galactocentric distance  $R/R_{25}$  for the SPIRAL galaxies.

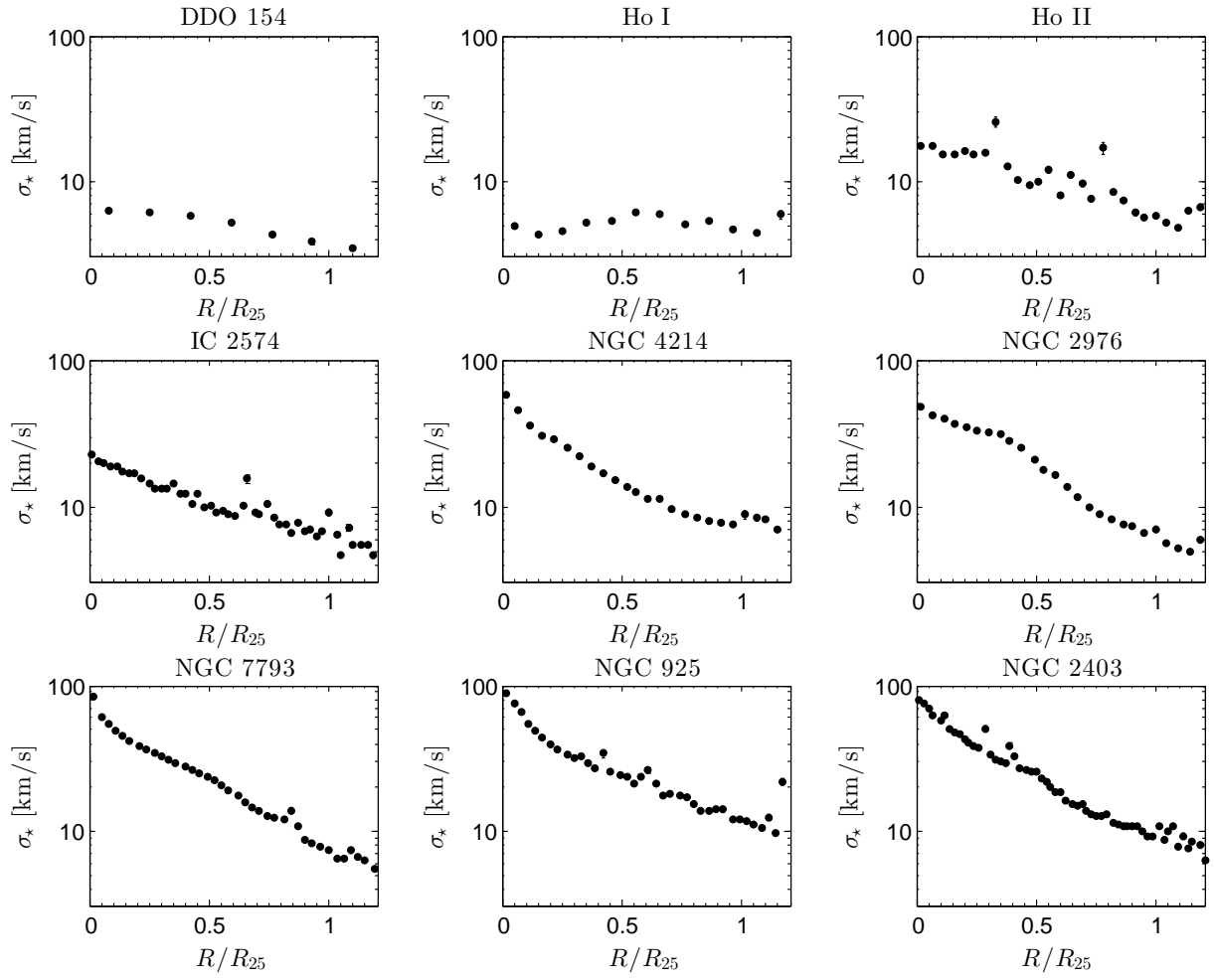


Figure A.7: The velocity dispersion of stars  $\sigma_*$  as a function of galactocentric distance  $R/R_{25}$  for the DWARF galaxies.

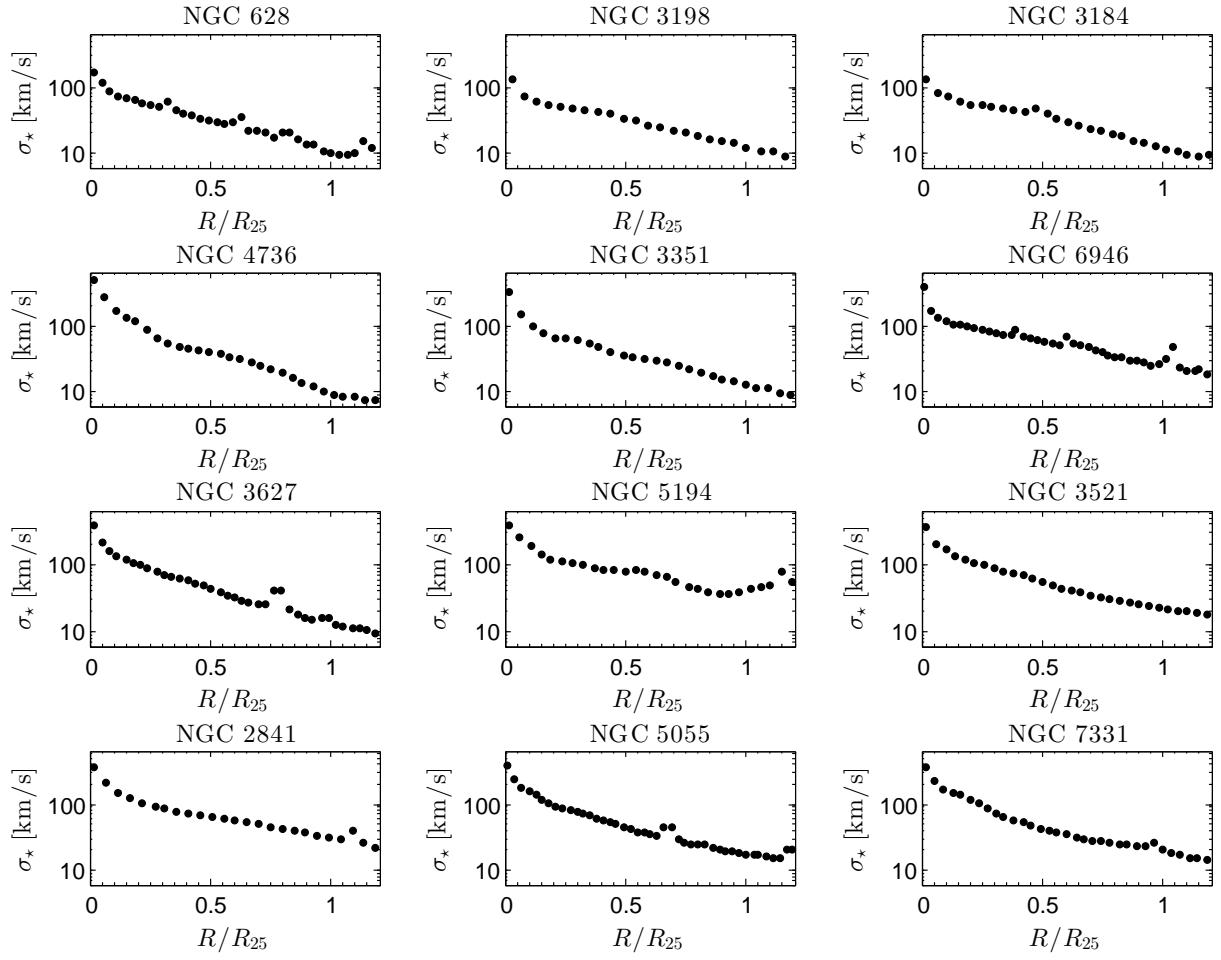


Figure A.8: The velocity dispersion of stars  $\sigma_*$  as a function of galactocentric distance  $R/R_{25}$  for the SPIRAL galaxies.

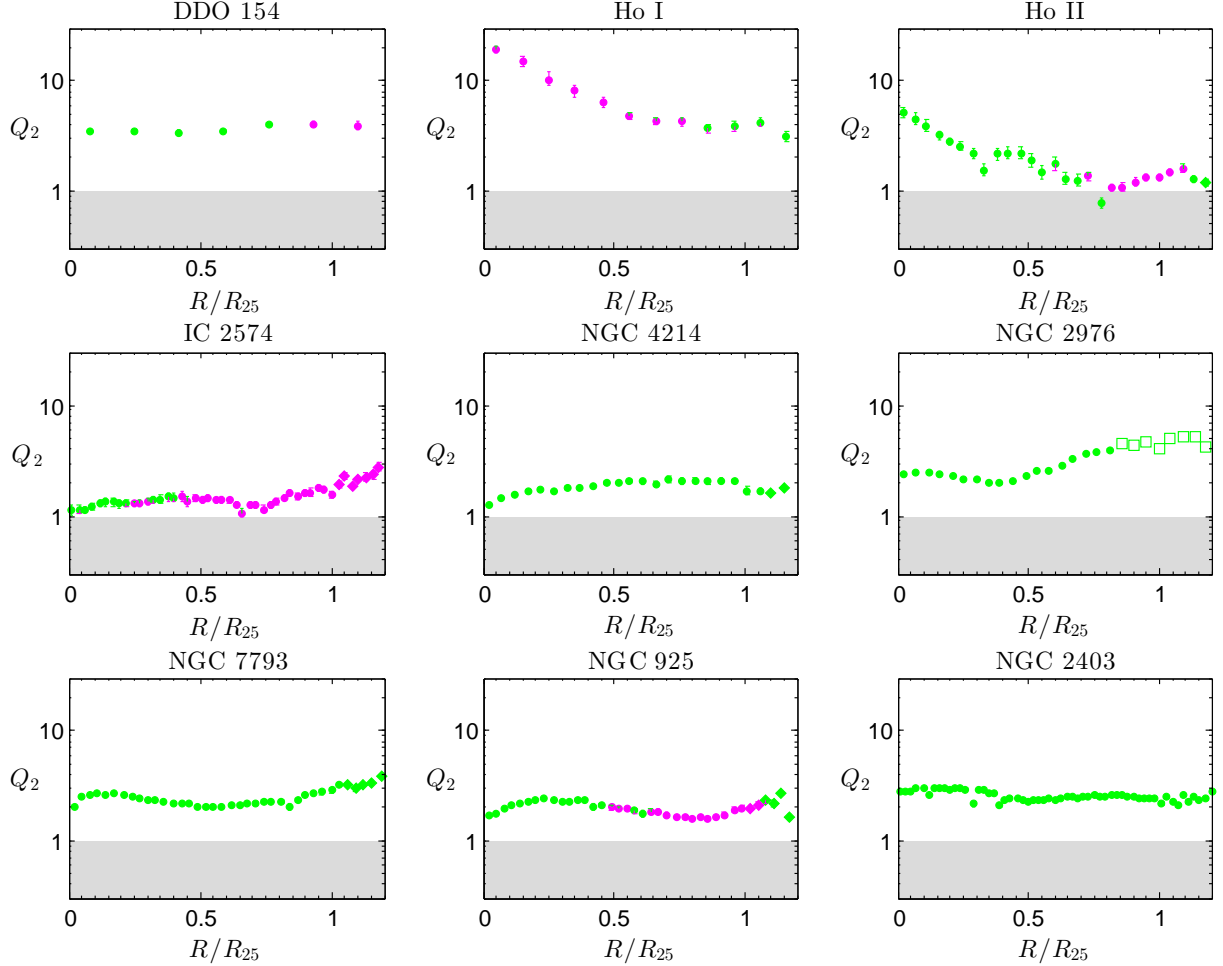


Figure A.9: The gravitational stability parameter  $Q_2$  WITHOUT  $H_2$  as a function of galactocentric distance  $R/R_{25}$  for the DWARF galaxies. The grey area shows the region of local gravitational instability and the colors of the points show which component dominates  $Q_N$ , i.e. has the smallest value of  $TQ$ , at each point. Green points are star-dominated and magenta points are gas-dominated. The symbols indicate the amount of gaseous data available. Points with non-vanishing values of both  $\Sigma_{H1}$  and  $\Sigma_{H2}$  are denoted by circles, point with non-vanishing values of  $\Sigma_{H1}$  but not  $\Sigma_{H2}$  are denoted by diamonds, and points with vanishing values of both  $\Sigma_{H1}$  and  $\Sigma_{H2}$  are denoted by empty squares. The error-bars have been omitted for the empty squares since they are inside the squares.

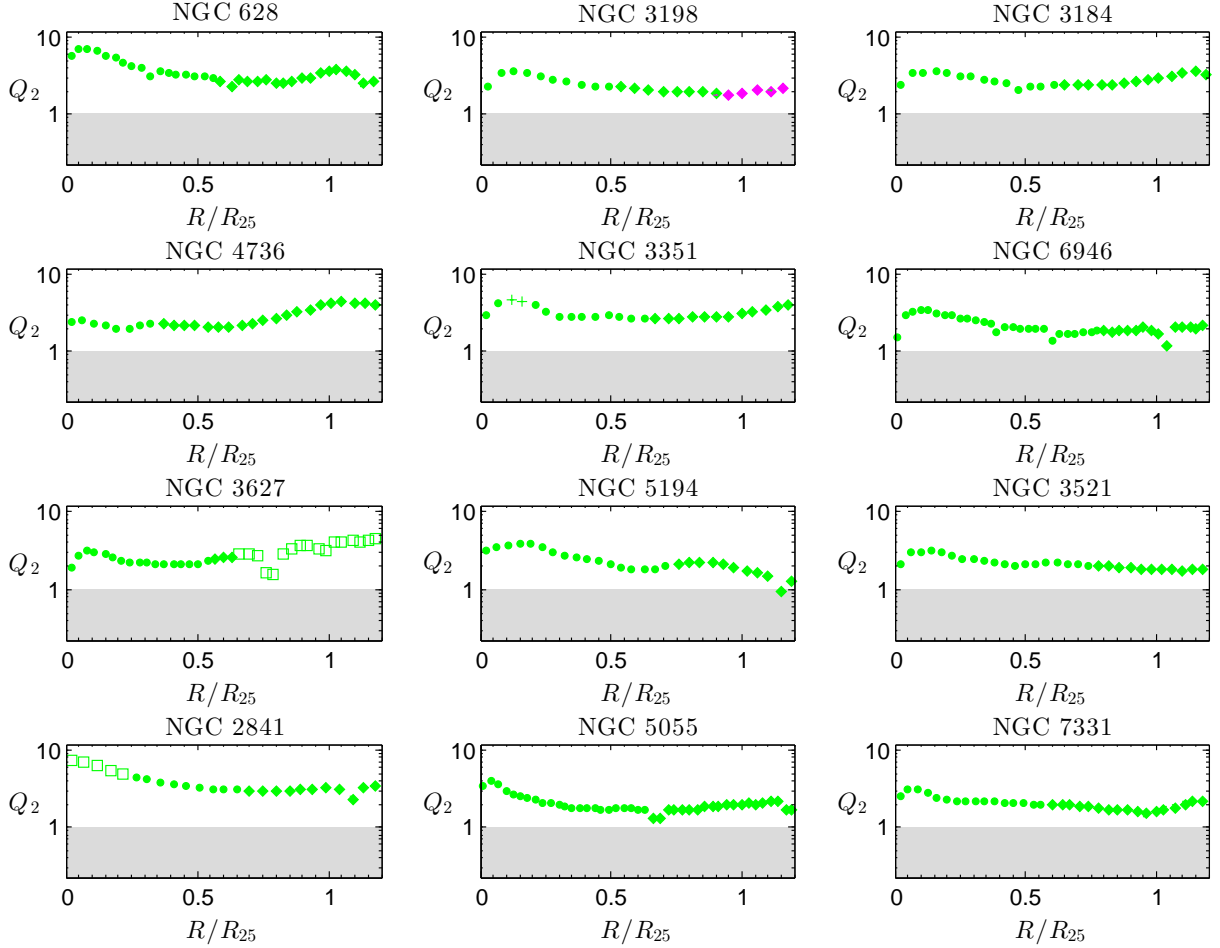


Figure A.10: The gravitational stability parameter  $Q_2$  WITHOUT  $H_2$  as a function of galactocentric distance  $R/R_{25}$  for the SPIRAL galaxies. The grey area shows the region of local gravitational instability and the colors of the points show which component dominates  $Q_N$ , i.e. has the smallest value of  $TQ$ , at each point. Green points are star-dominated and magenta points are gas-dominated. The symbols indicate the amount of gaseous data available. Points with non-vanishing values of both  $\Sigma_{H_I}$  and  $\Sigma_{H_2}$  are denoted by circles, point with non-vanishing values of  $\Sigma_{H_I}$  but not  $\Sigma_{H_2}$  or vice versa are denoted by diamonds and plus-signs, respectively, and points with vanishing values of both  $\Sigma_{H_I}$  and  $\Sigma_{H_2}$  are denoted by empty squares. The error-bars have been omitted for the empty squares since they are inside the squares.

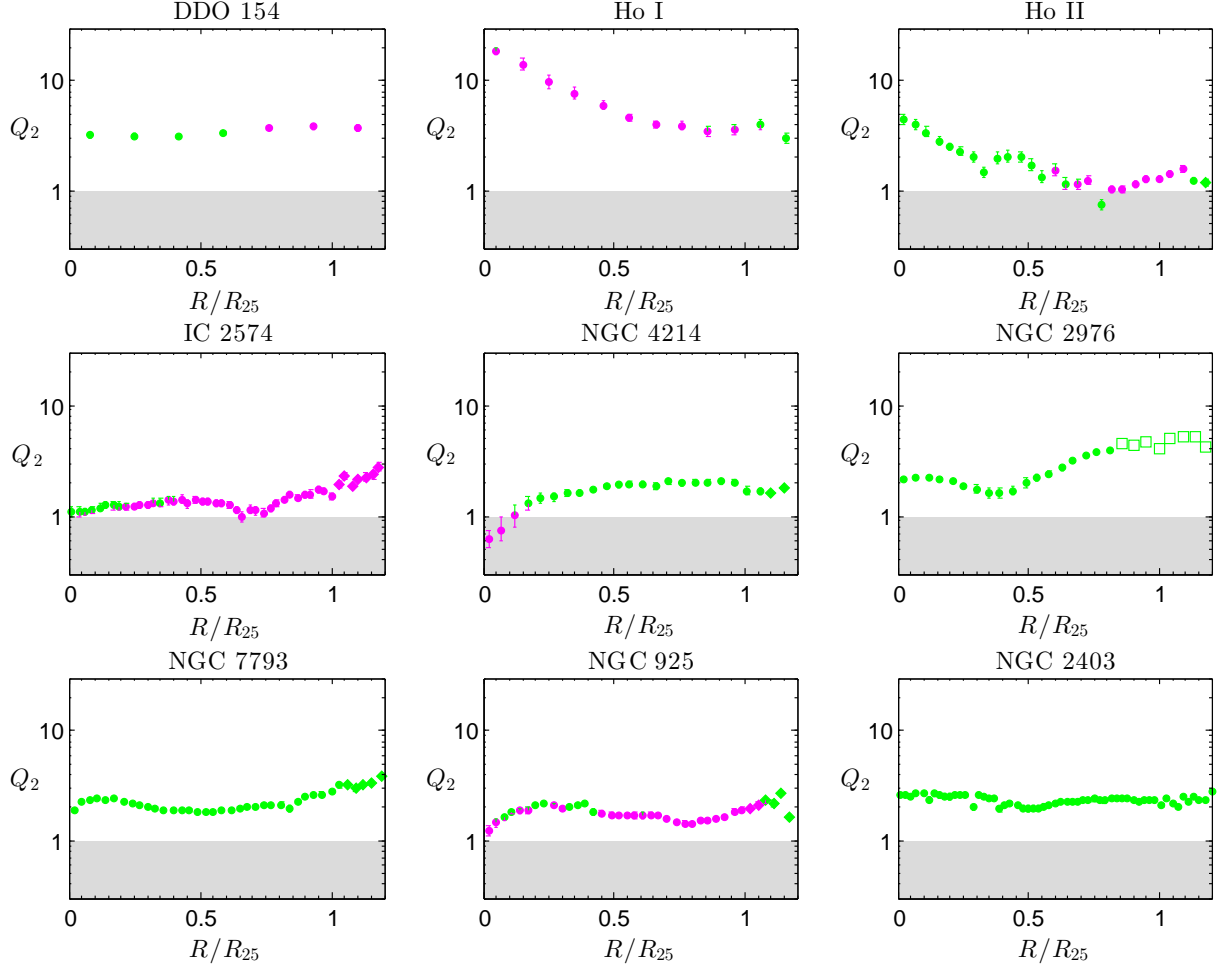


Figure A.11: The gravitational stability parameter  $Q_2$  WITH  $H_2$  as a function of galactocentric distance  $R/R_{25}$  for the DWARF galaxies. The grey area shows the region of local gravitational instability and the colors of the points show which component dominates  $Q_N$ , i.e. has the smallest value of  $TQ$ , at each point. Green points are star-dominated and magenta points are gas-dominated. The symbols indicate the amount of gaseous data available. Points with non-vanishing values of both  $\Sigma_{H1}$  and  $\Sigma_{H2}$  are denoted by circles, point with non-vanishing values of  $\Sigma_{H1}$  but not  $\Sigma_{H2}$  are denoted by diamonds, and points with vanishing values of both  $\Sigma_{H1}$  and  $\Sigma_{H2}$  are denoted by empty squares. The error-bars have been omitted for the empty squares since they are inside the squares.

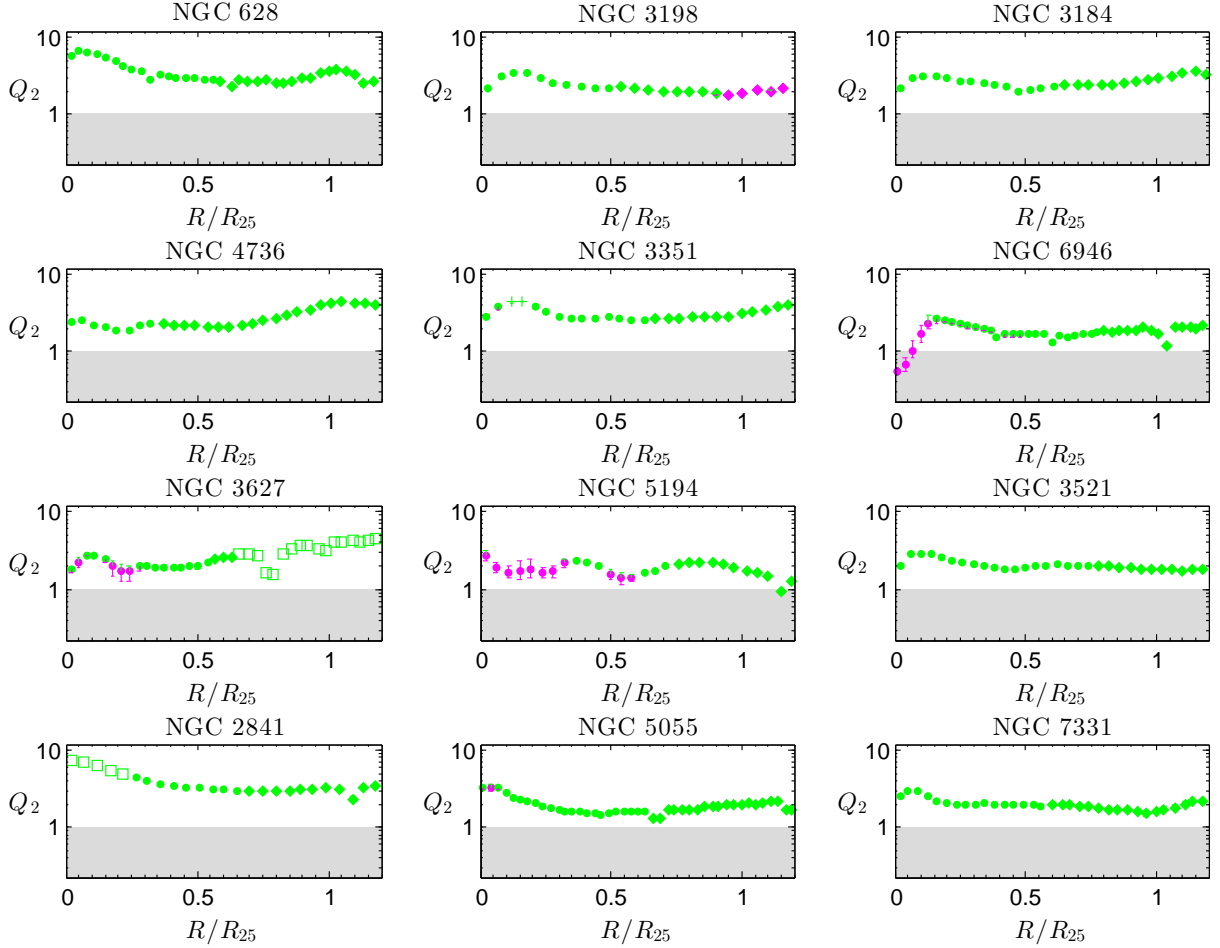


Figure A.12: The gravitational stability parameter  $Q_2$  WITH  $H_2$  as a function of galactocentric distance  $R/R_{25}$  for the SPIRAL galaxies. The grey area shows the region of local gravitational instability and the colors of the points show which component dominates  $Q_N$ , i.e. has the smallest value of  $TQ$ , at each point. Green points are star-dominated and magenta points are gas-dominated. The symbols indicate the amount of gaseous data available. Points with non-vanishing values of both  $\Sigma_{H_I}$  and  $\Sigma_{H_2}$  are denoted by circles, point with non-vanishing values of  $\Sigma_{H_I}$  but not  $\Sigma_{H_2}$  or vice versa are denoted by diamonds and plus-signs, respectively, and points with vanishing values of both  $\Sigma_{H_I}$  and  $\Sigma_{H_2}$  are denoted by empty squares. The error-bars have been omitted for the empty squares since they are inside the squares.

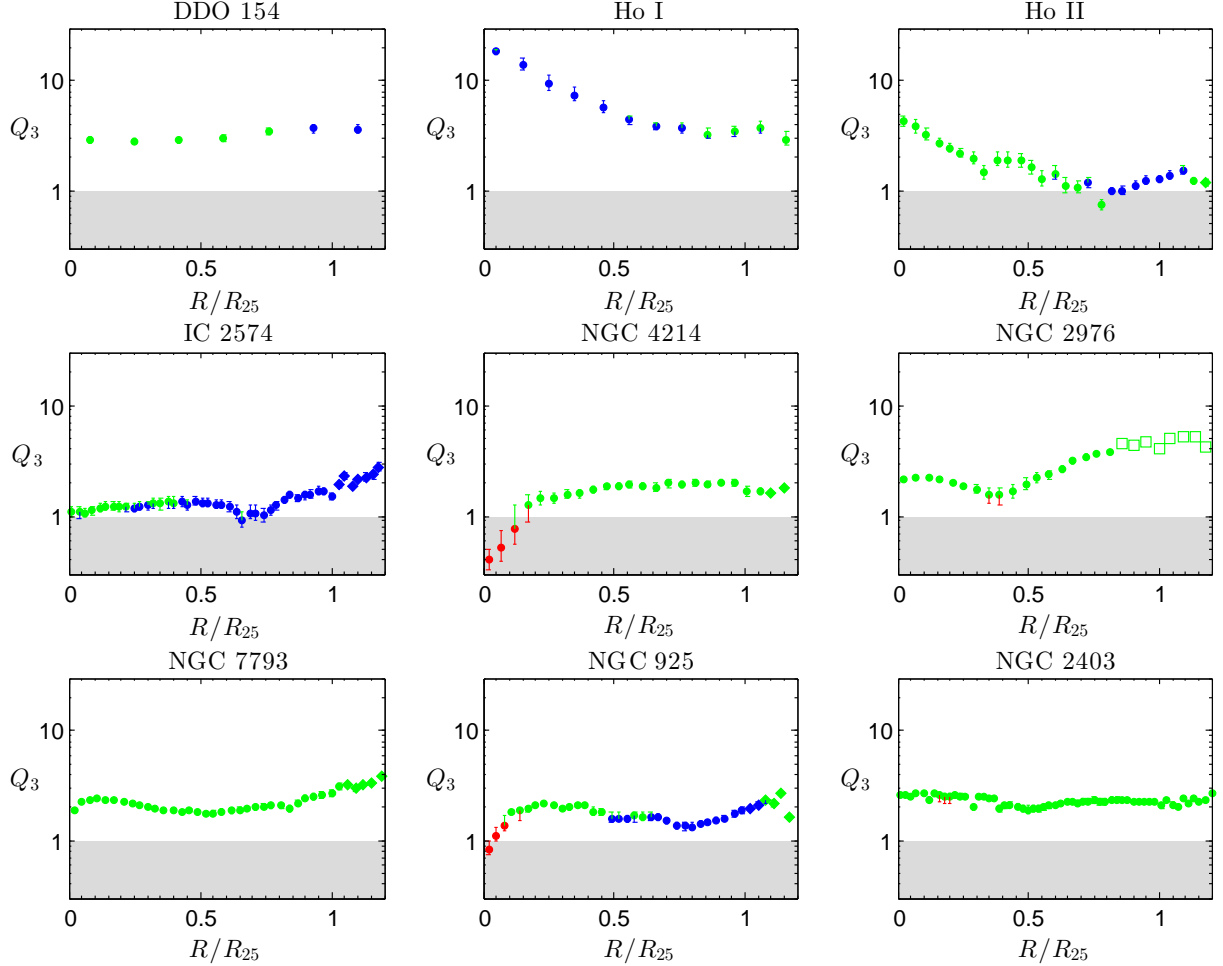


Figure A.13: The gravitational stability parameter  $Q_3$  as a function of galactocentric distance  $R/R_{25}$  for the DWARF galaxies. The grey area shows the region of local gravitational instability and the colors of the points show which component dominates  $Q_N$ , i.e. has the smallest value of  $TQ$ , at each point. Green points are star-dominated, blue points are H I-dominated and red points are H<sub>2</sub>-dominated. The symbols indicate the amount of gaseous data available. Points with non-vanishing values of both  $\Sigma_{\text{H I}}$  and  $\Sigma_{\text{H}_2}$  are denoted by circles, point with non-vanishing values of  $\Sigma_{\text{H I}}$  but not  $\Sigma_{\text{H}_2}$  are denoted by diamonds, and points with vanishing values of both  $\Sigma_{\text{H I}}$  and  $\Sigma_{\text{H}_2}$  are denoted by empty squares. The error-bars have been omitted for the empty squares since they are inside the squares.

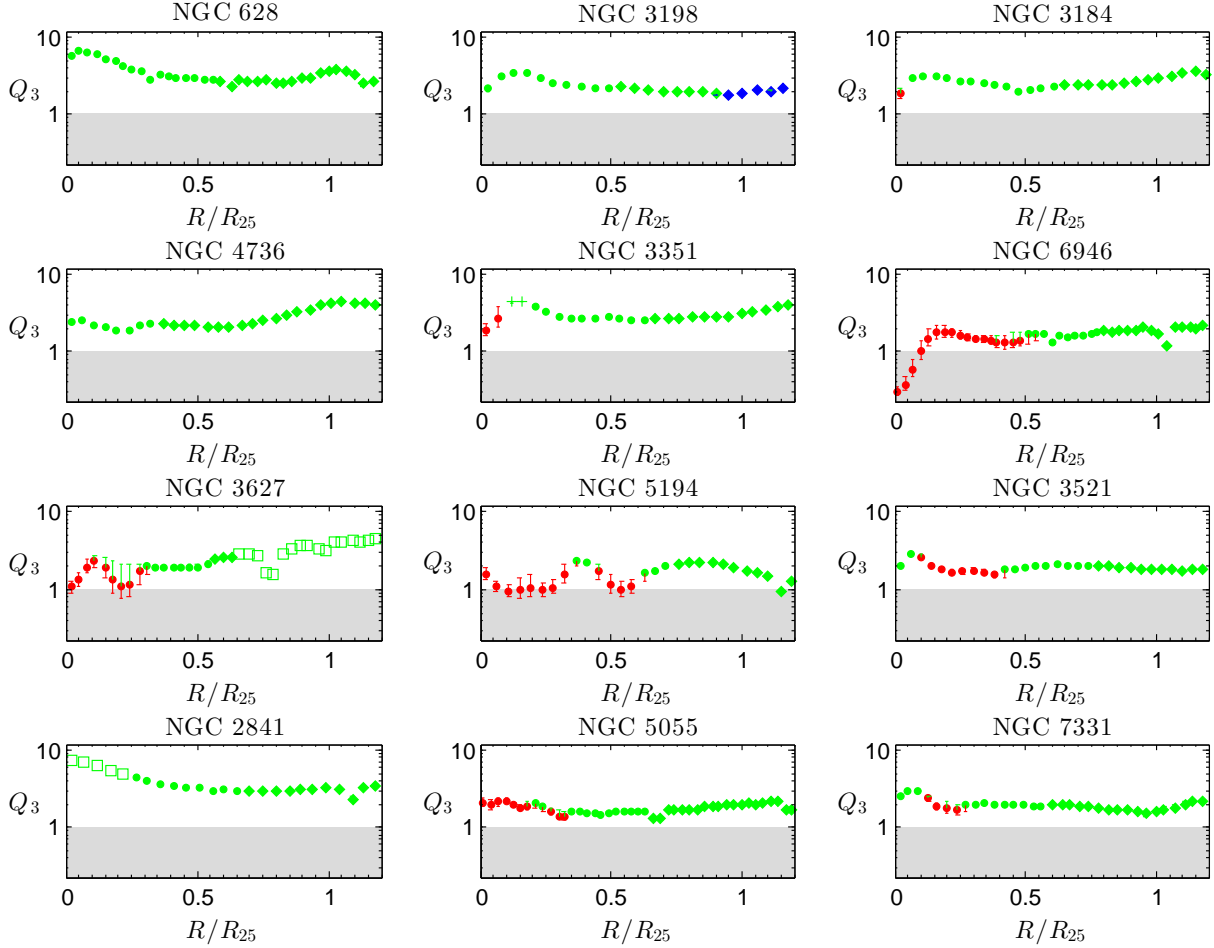


Figure A.14: The gravitational stability parameter  $Q_3$  as a function of galactocentric distance  $R/R_{25}$  for the SPIRAL galaxies. The grey area shows the region of local gravitational instability and the colors of the points show which component dominates  $Q_N$ , i.e. has the smallest value of  $TQ$ , at each point. Green points are star-dominated, blue points are H I-dominated and red points are H<sub>2</sub>-dominated. The symbols indicate the amount of gaseous data available. Points with non-vanishing values of both  $\Sigma_{\text{H I}}$  and  $\Sigma_{\text{H}_2}$  are denoted by circles, point with non-vanishing values of  $\Sigma_{\text{H I}}$  but not  $\Sigma_{\text{H}_2}$  or vice versa are denoted by diamonds and plus-signs, respectively, and points with vanishing values of both  $\Sigma_{\text{H I}}$  and  $\Sigma_{\text{H}_2}$  are denoted by empty squares. The error-bars have been omitted for the empty squares since they are inside the squares.

# Appendix B

## Error analysis

Let us first discuss the method by which the error-bars for  $Q_N$  were computed. We listed in (3.4) the parameters which  $Q_N$  depends on. Most of these were taken as constants and  $\sigma_*$  was computed from  $\Sigma_*$  using equation (3.6). Moreover,  $\kappa$  was computed from exponential fits to the rotation curves using equation (3.8)–(3.10). Naturally, these assumptions and approximations provide substantial systematical errors to  $Q_N$ , but such errors may be ignored for our present purpose since error-bars are only meant to show *statistical* errors. We should therefore think of  $Q_N$  for the spirals as a function of the continuous random variables  $\Sigma_*$ ,  $\Sigma_{H1}$  and  $\Sigma_{H2}$ , which we have assumed to be independent and normally distributed. Note that for the dwarfs  $Q_N$  is instead a function of  $\Sigma_*$ ,  $\Sigma_{H1}$  and  $\Sigma_{SFR}$  since we have computed  $\Sigma_{H2}$  for these galaxies from  $\Sigma_{SFR}$  using equation (3.7). The uncertainties of  $\Sigma_*$ ,  $\Sigma_{H1}$ ,  $\Sigma_{H2}$  and  $\Sigma_{SFR}$  are given in the electronic version of table 7 in Leroy et al. (2008) and we have interpreted these values as approximations of the standard deviations of the quantities in question.

For a differentiable function  $f$  of  $n$  uncorrelated and normally distributed continuous random variables  $X_i$ ,  $i = 1, 2, \dots, n$  with standard deviations  $\sigma_i$ ,  $i = 1, 2, \dots, n$ , respectively, one usually estimate the standard deviation  $\sigma_f$  with the help of the error propagation equation, which gives that (see for instance equation 3.14 in Bevington 2002)

$$\sigma_f^2 \approx \left(\frac{\partial f}{\partial x_1}\right)^2 \sigma_1^2 + \left(\frac{\partial f}{\partial x_2}\right)^2 \sigma_2^2 + \dots + \left(\frac{\partial f}{\partial x_n}\right)^2 \sigma_n^2. \quad (\text{B.1})$$

However, we cannot use this formula to estimate the standard deviation of  $Q_N$  since this function is not differentiable at points where the dominant component changes (see equation (2.2)–(2.5)). In fact, even if  $Q_N$  had been a differentiable function we still could not have used equation (B.1). The reason for this is that  $(\partial f/\partial x)\Delta x$  is only a good approximation of the difference  $\Delta f$  in  $f$  due to the difference  $\Delta x$  in  $x$  if  $\Delta x$  is small, but the relative uncertainties of  $\Sigma_*$ ,  $\Sigma_{H1}$ ,  $\Sigma_{H2}$  and  $\Sigma_{SFR}$  are quite large for some points.

We therefore used a different method to estimate the uncertainty of  $Q_N$ , which is precisely the same method as the one which was used by Romeo & Wiegert (2011) and Romeo & Falstad (2013). An upper ( $Q_+$ ) and a lower ( $Q_-$ ) bound on  $Q_N$  within  $\pm 1\sigma$ -intervals of the nominal values of the quantities which  $Q_N$  depends on were computed.  $Q_+$  and  $Q_-$  were used as the end-points of the error-bars while the dominant components at these points were used to determine the colors of the error-bars. For  $Q_2$  with  $H_2$  the

values of  $Q_-$ ,  $Q$  and  $Q_+$  were computed from the formulas below, where  $\Delta\Sigma_i$  denotes the uncertainty of  $\Sigma_i$ .

$$\sigma_{\star,z} = \left(\frac{2\pi Gl_\star}{7.3}\right)^{1/2} (\Sigma_\star)^{1/2}, \quad \sigma_{\star,z+} = \left(\frac{2\pi Gl_\star}{7.3}\right)^{1/2} \underbrace{(\Sigma_\star + \Delta\Sigma_\star)}_{\Sigma_{\star+}}^{1/2},$$

$$\sigma_{\star,z-} = \left(\frac{2\pi Gl_\star}{7.3}\right)^{1/2} \underbrace{(\Sigma_\star - \Delta\Sigma_\star)}_{\Sigma_{\star-}}^{1/2} \quad (\text{B.2})$$

$$\sigma_{\star,R} = \frac{1}{0.6}\sigma_{\star,z}, \quad \sigma_{\star,R+} = \frac{1}{0.6}\sigma_{\star,z+}, \quad \sigma_{\star,R-} = \frac{1}{0.6}\sigma_{\star,z-} \quad (\text{B.3})$$

$$Q_\star = \frac{\kappa\sigma_{\star,R}}{\pi G\Sigma_\star}, \quad Q_{\star+} = \frac{\kappa\sigma_{\star,R-}}{\pi G\Sigma_{\star-}}, \quad Q_{\star-} = \frac{\kappa\sigma_{\star,R+}}{\pi G\Sigma_{\star+}} \quad (\text{B.4})$$

$$\Sigma_g = \Sigma_{\text{H1}} + \Sigma_{\text{H2}}, \quad \Sigma_{g+} = \Sigma_{\text{H1}} + \Sigma_{\text{H2}} + (\Delta\Sigma_{\text{H1}}^2 + \Delta\Sigma_{\text{H2}}^2)^{1/2},$$

$$\Sigma_{g-} = \Sigma_{\text{H1}} + \Sigma_{\text{H2}} - (\Delta\Sigma_{\text{H1}}^2 + \Delta\Sigma_{\text{H2}}^2)^{1/2} \quad (\text{B.5})$$

$$Q_g = \frac{\kappa\sigma_g}{\pi G\Sigma_g}, \quad Q_{g+} = \frac{\kappa\sigma_g}{\pi G\Sigma_{g-}}, \quad Q_{g-} = \frac{\kappa\sigma_g}{\pi G\Sigma_{g+}} \quad (\text{B.6})$$

$$W = \frac{2\sigma_{\star,R}\sigma_g}{\sigma_{\star,R}^2 + \sigma_g^2}, \quad W_+ = \frac{2\sigma_{\star,R-}\sigma_g}{\sigma_{\star,R-}^2 + \sigma_g^2}, \quad W_- = \frac{2\sigma_{\star,R+}\sigma_g}{\sigma_{\star,R+}^2 + \sigma_g^2} \quad (\text{B.7})$$

$$\left(\frac{1}{Q}\right) = \begin{cases} \frac{W}{T_\star Q_\star} + \frac{1}{T_g Q_g} & \text{if } T_\star Q_\star \geq T_g Q_g \\ \frac{1}{T_\star Q_\star} + \frac{W}{T_g Q_g} & \text{if } T_g Q_g \geq T_\star Q_\star \end{cases},$$

$$\left(\frac{1}{Q}\right)_+ = \begin{cases} \frac{W_+}{T_\star Q_{\star-}} + \frac{1}{T_g Q_{g-}} & \text{if } T_\star Q_{\star-} \geq T_g Q_{g-} \\ \frac{1}{T_\star Q_{\star-}} + \frac{W_+}{T_g Q_{g-}} & \text{if } T_g Q_{g-} \geq T_\star Q_{\star-} \end{cases},$$

$$\left(\frac{1}{Q}\right)_- = \begin{cases} \frac{W_-}{T_\star Q_{\star+}} + \frac{1}{T_g Q_{g+}} & \text{if } T_\star Q_{\star+} \geq T_g Q_{g+} \\ \frac{1}{T_\star Q_{\star+}} + \frac{W_-}{T_g Q_{g+}} & \text{if } T_g Q_{g+} \geq T_\star Q_{\star+} \end{cases} \quad (\text{B.8})$$

$$Q = \frac{1}{(1/Q)}, \quad Q_+ = \frac{1}{(1/Q)_-}, \quad Q_- = \frac{1}{(1/Q)_+} \quad (\text{B.9})$$

Note that equation (B.7) requires that  $\sigma_{\star,R} > \sigma_g = \sigma_{\text{H1}}$ , but we showed in section 5.2 that this is not always the case. However, we also explained that computed values of  $\sigma_{\star,R}$  smaller than  $\sigma_{\text{H1}}$  are unphysical and therefore cannot be trusted.

For  $Q_2$  without  $\text{H}_2$  the equations are the same as (B.2)–(B.9) except without  $\Sigma_{\text{H2}}$  and  $\Delta\Sigma_{\text{H2}}$ , and for  $Q_3$  they are analogous with

$$m = \min\{T(i)Q(i)\}, \quad m_+ = \min\{T(i)Q_+(i)\},$$

$$m_- = \min\{T(i)Q_-(i)\}, \quad i = \star, \text{H1}, \text{H2} \quad (\text{B.10})$$

$$W(i) = \frac{2\sigma_R(m)\sigma_R(i)}{\sigma_R^2(m) + \sigma_R^2(i)}, \quad W_+(i) = \frac{2\sigma_{R-}(m-)\sigma_{R-}(i)}{\sigma_{R-}^2(m-) + \sigma_{R-}^2(i)},$$

$$W_-(i) = \frac{2\sigma_{R+}(m+)\sigma_{R+}(i)}{\sigma_{R+}^2(m+) + \sigma_{R+}^2(i)} \quad (\text{B.11})$$

The error-bars in figure 5.2 and 5.3 were also computed using completely analogous methods as those described above, and the error-bars in figure 5.1 were computed using the

$m$ -values of  $Q_+$ ,  $Q$  and  $Q_-$ . Moreover, it should be mentioned that the error-bars for  $Q_N^{\min}$  in figure 4.3–4.5 show  $Q_+$  and  $Q_-$  for the points with the smallest *nominal* values of  $Q_N$ . They do not take into account the fact that these points due to the uncertainty of  $Q_N$  may not have the smallest *physical* values of this quantity.

As a comparison we also computed error-bars for  $Q_N$  using *data smearing* (see for instance Bevington 2002). For each value of  $\Sigma_*$ ,  $\Sigma_{\text{HI}}$  and  $\Sigma_{\text{H}_2}$  ( $\Sigma_{\text{SFR}}$  for the dwarfs) given by Leroy et al. (2008) we computed 10000 pseudorandom numbers drawn from normal distributions centered at the tabular values of these quantities and with standard deviations equal to the uncertainties of the tabular values.

The result is shown in figure B.1. We see that the error-bars in these plots are very similar to those in figure 3.1. However, there are some important differences which make the latter error-bars better than the former. One such difference is that the error-bars in figure B.1 do not have individual colors, so one cannot tell how the uncertainty of  $Q_N$  may affect which component  $Q_N$  is dominated by. Also, the error-bars in this figure are symmetric, but the plots in figure B.2 suggest that the distribution of  $Q_N$  is very asymmetric for points with uncertain  $m$ -values. Moreover, using data smearing will only give accurate results if the tabular values of  $\Sigma_*$ ,  $\Sigma_{\text{HI}}$  and  $\Sigma_{\text{H}_2}$  ( $\Sigma_{\text{SFR}}$ ) are relatively close to the expectation values of these quantities, which may not be the case.

Let us now briefly discuss the data points with vanishing values of both  $\Sigma_{\text{HI}}$  and  $\Sigma_{\text{H}_2}$ , which we denoted by empty squares in figure 3.1, 5.1, 5.4 and A.9–A.14. We mentioned in section 3.2 that these points were excluded from the stability analysis in this thesis and we will now see how including them would have affected our results. Figure B.3 shows the same plots as figure 3.2 except that the square points are included in the former plots and excluded from the latter, and we see that there is no qualitative difference between the plots in these two figures.

Finally, let us explain how the percentages of data points within different intervals or regions were computed for figure 5.1, 5.2 and 5.3. The simplest method of computing the number of points within, for instance, the two-phase region in figure 5.3 is to simply count the number of points inside this region, divide that number by the total number of points and multiply the result by 100. However, this method does not take into account the uncertainty of the position of each point. Unfortunately, there is no unambiguous way to include this uncertainty in the computation of the percentages, but we have at least *tried* to do so in several different ways. One method which we used was to consider each data point as three distinct points: a nominal point computed from tabular values and two more points given by the end-points of the error-bars for the nominal point (method 1). Another method which we tried was data smearing (method 2). In table B.1 we compare the results given by these two methods for the percentages of data points with  $\sigma_* < \sigma_{\text{HI}}$  in the upper plots in figure 5.2, and we see that in this case the results are very similar.

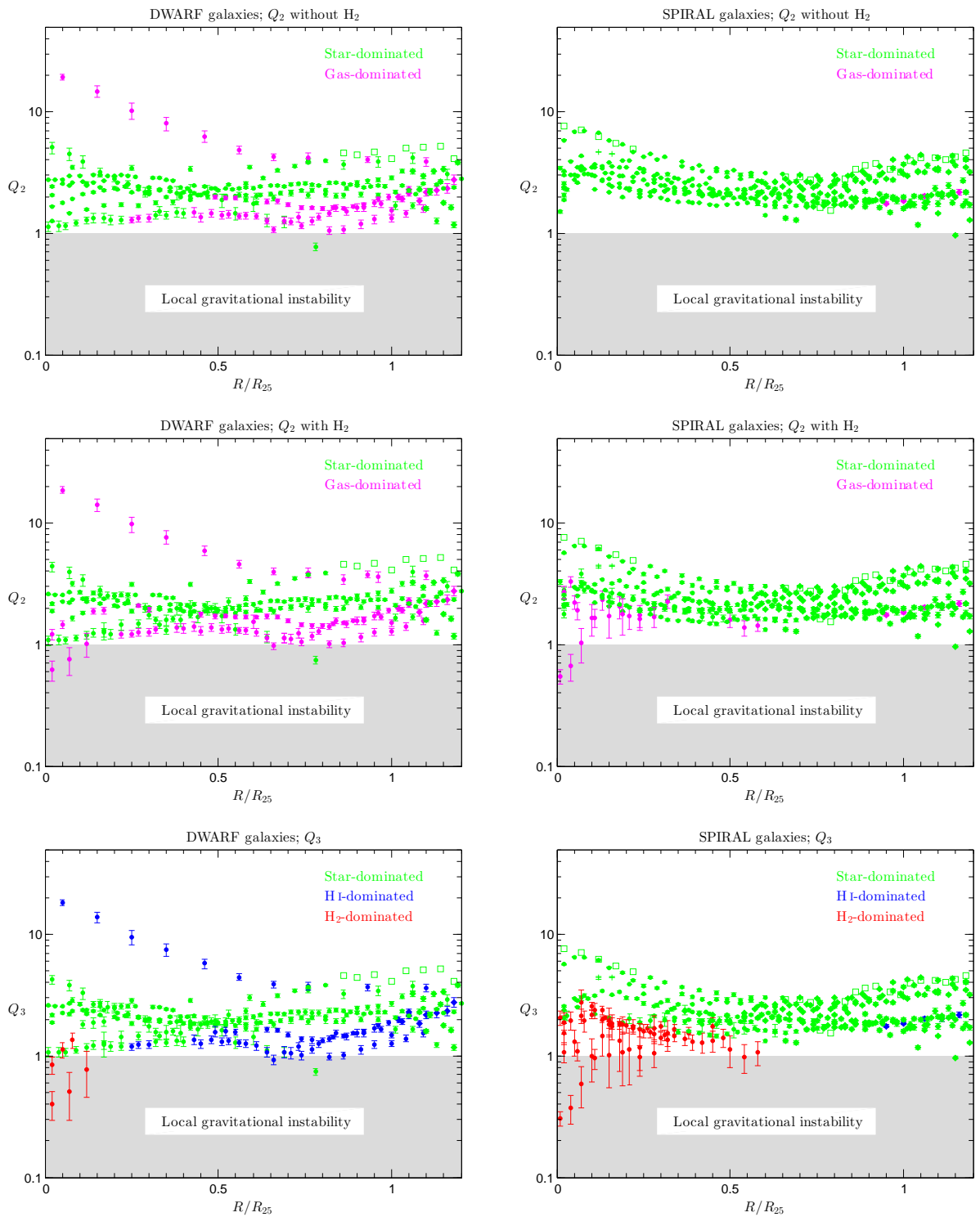


Figure B.1: The same plots as in figure 3.1 except that the error-bars in this figure have been computed using data smearing.

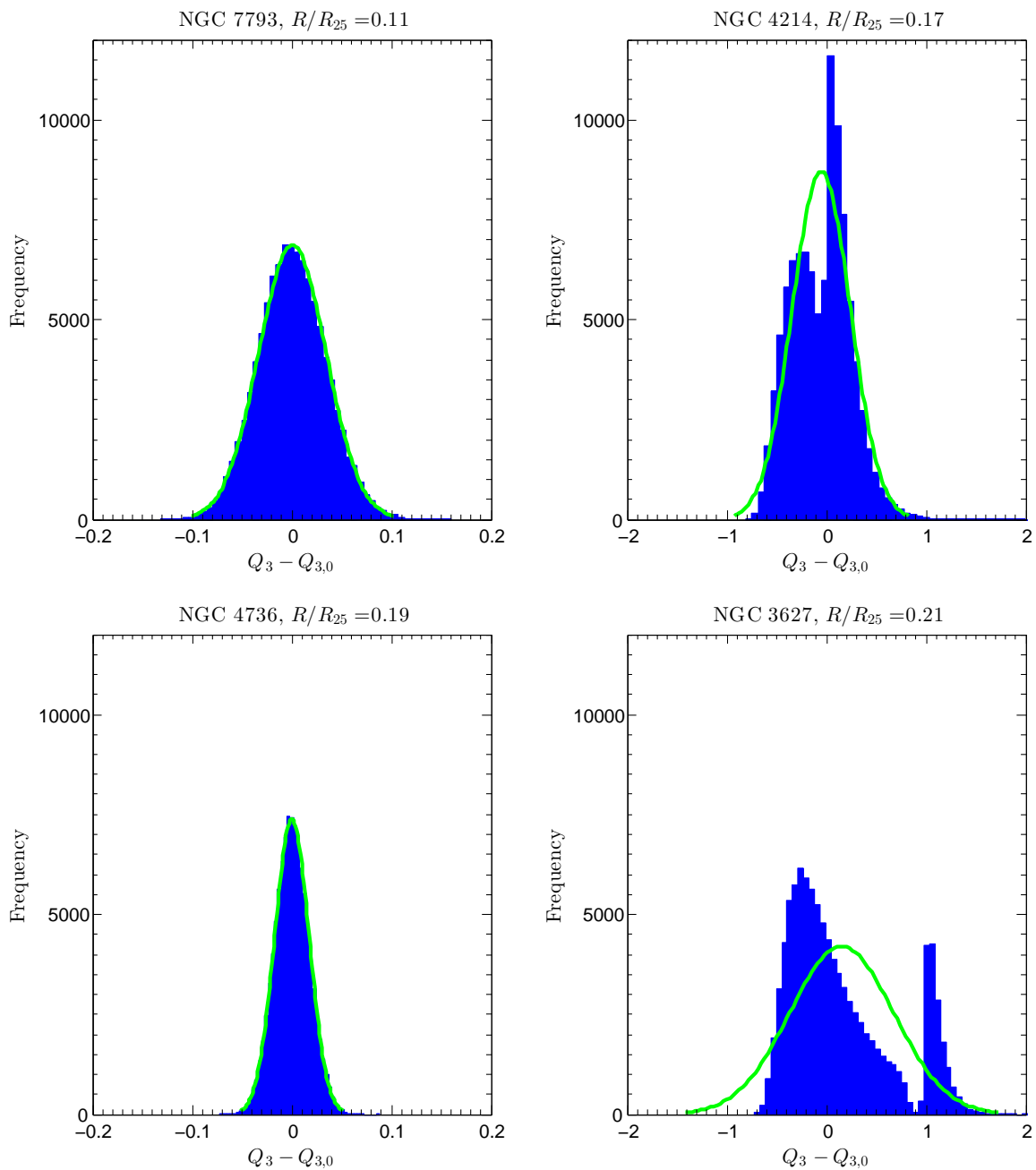


Figure B.2: The distribution of  $Q_3$  relative to the nominal value  $Q_{3,0}$  of  $Q_3$  (computed directly from the tabular values of Leroy et al. 2008) for two points belonging to the dwarf galaxies NGC 7793 and NGC 4214 and two points belonging to the spiral galaxies NGC 4736 and NGC 3627. The galactocentric distances  $R/R_{25}$  for these points are also given as well as Gaussian fits to the distributions (the green curves). For each point 100000 pseudorandom numbers were generated and the  $Q_{3,0}$ -points were selected so that the left plots are for points with well-defined dominant components while the right plots are for points with very uncertain dominant components. We see that in the left plots the  $Q_3$ -distributions are nearly perfectly Gaussian while in the right plots they are very far from being Gaussian. Also note that the horizontal scales are different and that the distributions in the right plots are an order of magnitude broader than those in the left plots.

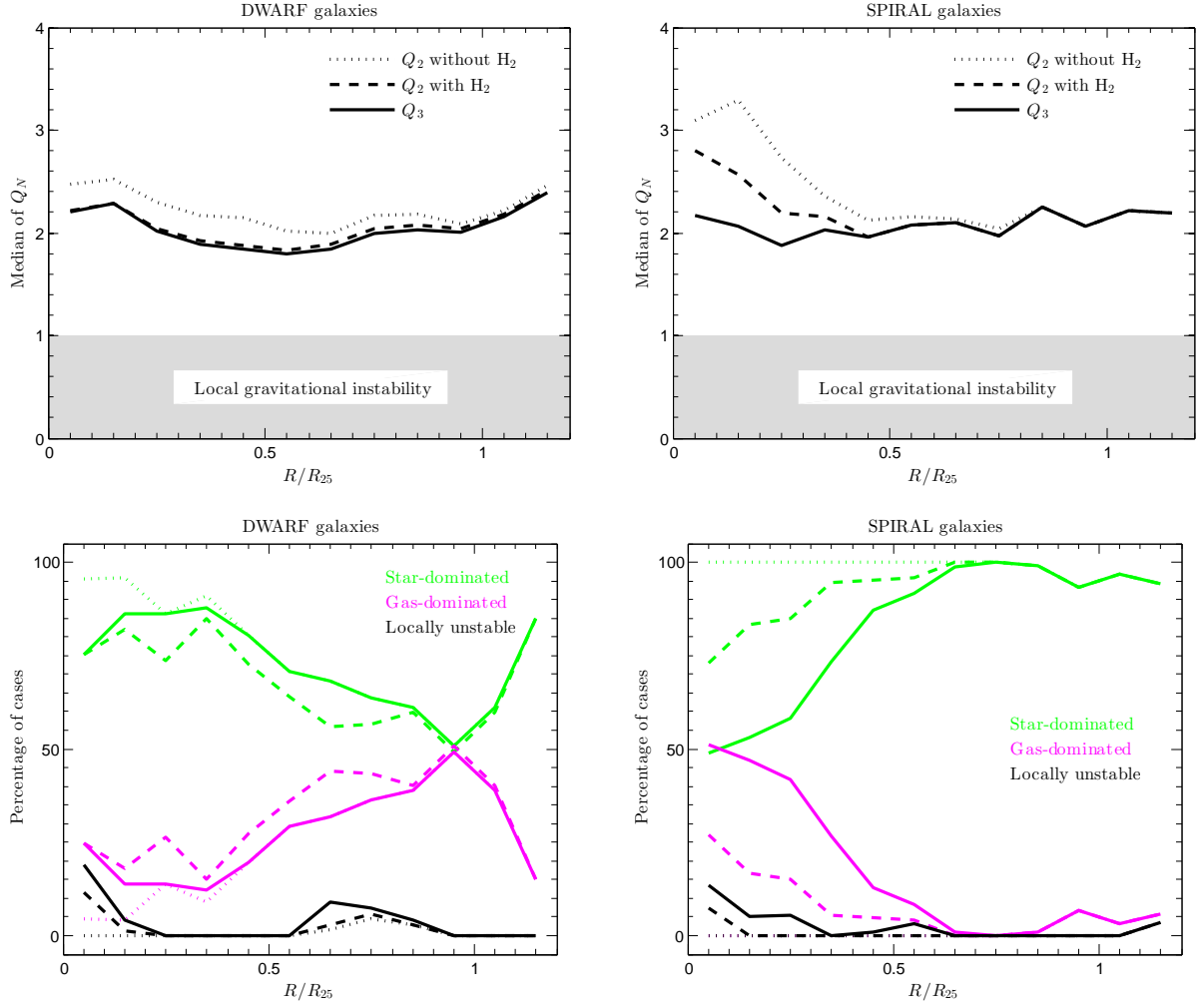


Figure B.3: The same plots as in figure 3.2 except that the data points with vanishing values of both  $\Sigma_{H_1}$  and  $\Sigma_{H_2}$  have been included in this figure.

Table B.1: The percentages of data points with  $\sigma_* < \sigma_{H_1}$  in the upper plots in figure 5.2 computed with the two methods described in the main text.

Method	Left plot	Right plot
1	41%	16%
2	41%	17%

# Bibliography

Bevington P. R., 2002, *Data Reduction and Error Analysis for the Physical Sciences*, 3rd ed., McGraw-Hill, NY

Bigiel F., Leroy A. K., Walter F., Brinks E., de Blok W. J. G., Madore B., Thornley M. D., 2008, *AJ*, 136, 2846

Binney J. & Tremaine S., 2008, *Galactic Dynamics*, 2nd ed., Princeton University Press, Princeton, NJ

de Blok W. J. G., Walter F., Brinks E., Trachternach C., Oh S.-H., Kennicutt R. C. Jr., 2008, *AJ*, 136, 2648

Fanelli M. N., et al., 1997, *AJ*, 481, 735

Hoffmann V. & Romeo A. B., 2012, *MNRAS*, 425, 1511

Ianjamasimanana R., de Blok W. J. G., Walter F., Heald G. H., 2012, *AJ*, 144, 96

Kennicutt R. C., 1989, *ApJ*, 344, 685

Kennicutt R. C. Jr., 1998, *ApJ*, 498, 541

Leroy A. K., Walter F., Brinks E., Bigiel F., de Blok W. J. G., Madore B., Thornley M. D., 2008, *AJ*, 136, 2782

Li Y., Low M.-M. M., Klessen R. S., 2005, *ApJ*, 626, 823

Li Y., Low M.-M. M., Klessen R. S., 2006, *ApJ*, 639, 879

Martin C. L. & Kennicutt R. C. Jr., 2001, *ApJ*, 555, 301

Ott J., Walter F., Brinks E., van Dyk S. D., Dirsch B., Klein U., 2001, *AJ*, 122, 3070

Quirk W. J., 1972, *ApJ*, 176, L9

Rafikov R. R., 2001, *MNRAS*, 323, 445

Romeo A. B., 1990, PhD thesis

Romeo A. B., 1992, *MNRAS*, 256, 307

Romeo A. B. & Falstad N., 2013, *MNRAS*, 433, 1389

Romeo A. B., Horellou C. & Bergh J., 2004, MNRAS, 354, 1208

Romeo A. B. & Wiegert J., 2011, MNRAS, 416, 1191

Schmidt M., 1959, ApJ, 129, 243

Spitzer L., 1968, Diffuse Matter in Space, Wiley, NY

Toomre A., 1964, ApJ, 139, 1217

Walter F., Brinks E., de Blok W. J. G., Bigiel F., Kennicutt R. C. Jr., Thornley M. D., Leroy A. K., 2008, AJ, 136, 2563

Westfall K. B., Andersen D. R., Bershadsky M. A., Martinsson T. P. K., Swaters R. A., Verheijen M. A. W., 2014, ApJ, 785, 43